12-1-2007

Seismic analysis and design of steel concentrically braced frames with self-centering friction damping brace

S. Zhu

Y. Zhang

Seismic Analysis and Design of Steel Concentrically Braced Frames with Self-Centering Friction Damping Brace

by

Songye Zhu

Yunfeng Zhang

ATLSS Report No. 07-09

December 2007

ATLSS is a National Center for Engineering Research on Advanced Technology for Large Structural Systems

117 ATLSS Drive
Bethlehem, PA 18015-4729

Phone: (610)758-3525
Fax: (610)758-5902

www.atlss.lehigh.edu
Email: inatl@lehigh.edu

Seismic Analysis and Design of Steel Concentrically Braced Frames with Self-Centering Friction Damping Brace

by

Songye Zhu
Graduate Research Assistant

Yunfeng Zhang
Associate Professor
yuz8@lehigh.edu

ATLSS Report No. 07-09

December 2007

ATLSS is a National Center for Engineering Research on Advanced Technology for Large Structural Systems

117 ATLSS Drive
Bethlehem, PA 18015-4729

Phone: (610)758-3525
Fax: (610)758-5902

www.atlss.lehigh.edu
Email: inatl@lehigh.edu

TABLE OF CONTENTS

LIST OF TABLES

LIST OF FIGURES

ABSTRACT

This dissertation presents a special type of bracing element termed self-centering friction damping brace (SFDB) for use in high performance concentrically braced frame (CBF) systems. The SFDB provides a passive form of energy dissipation with its core re-centering component made of stranded superelastic shape memory alloy (SMA) wires while enhanced energy dissipation mechanism of the SFDB is achieved through friction mechanism. The mechanical configuration of the SFDB is first described, and the experimental results of scaled SFDB specimens with different friction levels performed to validate its concept are also presented.

In this study, superelastic Nitinol is selected as the SMA material because of its prominent superelastic behavior and long fatigue life. The material properties of superelastic Nitinol wires are experimentally investigated through a series of uniaxial cyclic tests. The fatigue life and the effect of loading rate as well as temperature are also studied as parts of these experimental tests. Two types of constitutive models to describe the stress-strain relationship of superelastic Nitinol wires are presented here: a rate-dependent thermomechanical model and a rate-independent phenomenological model. Based on the calibrated constitutive model for superelastic Nitinol wires, an analytical model for SFDB has been developed to simulate the unique hysteretic behavior of SFDB.

The seismic performance of SFDB frames is evaluated based on nonlinear pushover and time history analyses of two prototype buildings—a 3-story and a 6-

story concentrically braced frames—at different seismic intensity levels. A simplified displacement-based design procedure for SFDB frame is presented here, for which SFDBs are proportioned based on the target performance level under design basis earthquakes. The results demonstrate that SFDB frame has several desirable performance characteristics. For example it has minimal residual drift after frequent and design basis earthquakes due to its self-centering capability. It also has the potential to withstand several design level earthquakes without the need for repair or replacement if properly designed.

CHAPTER 1 INTRODUCTION

1.1 BACKGROUND

Structures with conventional seismic load resistance system often dissipate seismic energy through activating ductile inelastic deformation in selected structural elements. Such a seismic design strategy may not be appealing from a life-cycle cost perspective, especially for high seismic regions, where costly repairs are often required after moderate earthquakes. After the 1994 Northridge earthquakes, growing interests are given to a more logical seismic design strategy which involves energy dissipation through supplemental dampers or fuse-type energy dissipating devices. In such systems, the main structural system (i.e., gravity load bearing system) is intended to have little or no damage while dedicated energy dissipating devices are designated for energy dissipation and can be replaced if damaged during earthquakes. Examples of such energy dissipation devices are friction dampers (Filiatrault and Cherry 1987; Grigorian and Popov 1993), buckling-restrained brace (Fahnestock et al 2007; Sabelli 2003), metallic yield damper (Tsai and Tsai 1995) and other types of passive or semi-active dampers.

Friction damping devices dissipate energy by utilizing the mechanism of solid friction developed at a sliding surface, which is a relatively inexpensive and effective way for stable energy dissipation. It is important to maintain a consistent, predictable frictional force throughout the life of these devices (Soong et al. 1997). Friction

damped braced (FDB) frames have been studied by Pall and Marsh (1982), Filiatrault and Cherry (1987), Aiken *et al*. (1988) and FitzGerald *et al* (1990). Their results show that properly designed FDB frame can outperform traditional moment resisting frames and braced frames. The addition of friction dampers results in a significant reduction in inter-story drifts and internal forces. Meanwhile slotted bolted connections intended for application in concentrically braced frames was also proposed by Grigorian and Popov (1993). The use of brass on steel frictional surface was recommended based on the experiment results of different types of slotted bolted connections. Nims et al. (1993) developed a passive friction-based energy dissipation device termed energy dissipating restraint (EDR), which consists of internal spring, compression wedges friction wedges, stops and cylinder and exhibits a self-centering hysteresis. The EDR would be installed in a building as a part of the bracing system which resists seismically induced lateral forces.

Large residual deformations in conventional ductile structure after strong earthquake event can make the structure appear unsafe to occupants, impair the structural response to a subsequent aftershock earthquake and significantly increase the cost of post-earthquake repair or renewal (Ruiz-Garcia and Miranda 2006a, 2006b). Residual structural deformation thus starts to be recognized as a complementary parameter in the evaluation of structural (and non-structural) damage in performance-based earthquake engineering (Pampanin et al. 2003; Christopoulos and Pampanin 2004). Recognizing the importance of controlling the residual deformation, self-centering seismic resisting system has recently been attracting considerable attention from the community (e.g., Kurama et al. 1999; Lu et al. 2000; Ricles et al. 2001;

Christopoulos et al. 2002b; Mahin et al 2006). A flag-shaped hysteresis loop is typical of such self-centering systems with certain energy dissipation capability, which is able to reduce (or even eliminate) residual structural deformation after strong earthquakes.

Shape memory alloys (SMA) refer to a unique group of alloys with the ability to return to some pre-defined shape when subjected to a proper thermal-mechanical procedure (Duerig et al. 1990; Shaw and Kyriakides 1995; Birman 1997). The most common SMA material in industrial applications is the alloy of nickel and titanium called Nitinol, which exhibits outstanding fatigue properties and excellent corrosion resistance (Oshida and Miyazaki 1991; Kim and Miyazaki 1997).

Due to its unique energy dissipation behavior and high fatigue life, SMA has been studied for use as damping device for hazard mitigation application (e.g., Graesser and Cozzarelli 1991; Aiken et al. 1992, 1993; Witting and Cozzarelli 1992; Clark et al. 1995; Whittaker et al. 1995; Higashino 1996; Wilde et al. 2000; Dolce et al. 2000, 2005; Castellano et al. 2001; Saadat et al. 2002; Ocel et al. 2004; DesRoches et al. 2004). For example, Krumme et al. (1995) have developed a SMA damping device termed center-tapped device for passive control of the dynamic response of civil structures. The center-tapped device comprises a simple slider mechanism in which resistance to linear sliding is provided by two pairs of opposed SMA tension elements. Whittaker et al (1995) developed two conceptual designs for SMA dampers, the effectiveness of which to mitigate the seismic hazard was demonstrated by the nonlinear time history analysis of an existing reinforced concrete frame retrofitted using these SMA dampers under moderate earthquake ground motions. Dolce et al. (2000) tested Nitinol-based devices with full re-centering and good energy dissipation

capabilities. Their experimental results have shown that SMA braces can provide a performance level at least comparable to those of steel braces, while having an additional self-centering feature. In Italy, superelastic SMA damping devices have also been implemented in several masonry cultural heritage structures to enhance their seismic resistance capacities during recent restoration (Castellano et al. 2001; Indirli et al. 2001). DesRoches and Delemont (2002) have tested the efficacy of superelastic NiTi bars as bridge restrainers to reduce the risk of collapse from unseating of bridge superstructures at the hinges. Additionally, two full-scale partially restrained steel beam-column connections using SMA bars for providing additional energy dissipation were tested by Ocel et al. (2004). The connection consists of four large diameter Nitinol SMA bars connecting the beam flange to the column flange and serve as the primary moment transfer mechanism. The connections exhibited a high level of energy dissipation, large ductility capacity, and no strength degradation after being subjected to cycles up to 4% drift.

1.2 OBJECTIVE AND SCOPE OF STUDY

This research presents a special type of bracing element termed self-centering friction damping brace (SFDB) which exhibits a flag-shaped hysteresis loop and has a potential to establish a new type of concentrically braced frame systems with self-centering capability. For SFDB, its self-centering ability is realized by using superelastic SMA wires while its enhanced energy dissipation capacity is achieved through friction mechanism. The overall objective of this research is to investigate the

system-level performance of SFDB frame under various seismic intensity levels. Specifically, the research work can be divided into the following five major tasks:

- *Experimentally characterize the mechanical properties of SMA materials*. Among many SMA materials, Nitinol is selected in this study due to its superior material properties. The material properties of Nitinol wires critical to the seismic applications, including their fatigue life, hysteretic behavior, rate-induced effect, temperature-induced effect, etc., are investigated through a series of cyclic tensile tests of Nitinol wires. The one-dimensional stress-stain relationship of Nitinol wires as determined from characterization tests serves as the basis for subsequent analytical study in this research.
- *Develop and validate the mechanical configuration and principle of the SFDB device*. A novel mechanical configuration of SMA-based energy dissipation device is proposed in this research. Validation test of scaled SFDB specimens were performed in order to verify the concept of SFDB.
- *Develop the analytical model for SMA-based device*. Two constitutive models for superelastic SMA wires are proposed here in order to simulate its hysteretic behavior under dynamic loading. New SFDB elements have been developed by the author for the DRAIN-2DX program and were used in seismic response analyses of SFDB frame.
- *Perform nonlinear pushover and time history analyses of prototype buildings.* The system-level performance of SFDB frame is evaluated for three intensity levels of seismic loading, namely, the frequent earthquake (FE), the design basis earthquake (DBE) and the maximum considered earthquake (MCE).

- *Develop a displacement-based seismic design procedure for SFDB frame* in order to facilitate the implementation of SFDBs in real buildings. The ductility and peak inter-story drift ratio of SFDB frames are selected as two target performance parameters. SFDB is proportioned accordingly to achieve the target performance.

1.3 OUTLINE OF DISSERTATION

This dissertation consists of six chapters, including an introduction in this chapter and the summary and conclusions in Chapter 6. The remaining chapters are organized as follows,

- Chapter 2 presents the experimental characterization of mechanical properties of Nitinol wires. Its material properties essential to seismic resistant structure applications, such as fatigue life, material degradation with increasing number of cycles, effect of loading rate and temperature, are investigated through a series of uniaxial cyclic test of superelastic Nitinol wires.
- Chapter 3 presents two constitutive models for the superelastic Nitinol wires: the first one is a rate-dependent thermo-mechanical model, while the other is a rate-independent phenomenological model termed as modified Wilde model. The derivation process and mathematical expression for these two models are described in this chapter. The thermo-mechanical constitutive model is derived in a thermodynamic framework and is comprised of three key components – a mechanical law, an energy balance equation and a transformation kinetics rule. The good agreement with experimental results indicates that this thermo-

mechanical model is capable of predicting the strain-rate dependent hysteretic behavior of superelastic Nitinol wires. The pros and cons of the rate-dependent and rate-independent constitutive models are also given in this chapter. Finally a feasibility study of using rate-independent constitutive models for Nitinol wires in seismic analyses of structures with SMA-based devices are investigated through the comparative study between rate-dependent and rate-independent models.

- Chapter 4 describes the mechanical configuration and mechanics of SFDB device. Cyclic test of scaled SFDB specimens under dynamic loading rates was carried out in order to validate the concept of SFDB. To simulate the hysteretic behavior of SFDB, an analytical model for SFDB is described, which is used in the analytical study described in the following chapters. The typical hysteretic behavior as predicted by the analytical model of SFDB, as well as the characteristics of SFDB, is also discussed.
- In Chapter 5, a comparative study between SFDB frame and buckling-restrained braced frame (BRBF) is conducted in order to better understand the seismic performance of SFDB frames. The comparative study is based on two prototype buildings: 3-story and 6-story concentrically braced frames. Nonlinear time history analyses of these two types of braced frames was carried out under different seismic intensity levels: frequent earthquakes, design basis earthquakes and maximum considered earthquakes. Analysis results of seismic response including displacement, acceleration, peak inter-story drift and residual inter-story drift are discussed.

- In Chapter 6, a displacement-based seismic design procedure of SFDB frame is presented. The nonlinear response spectrum of SDOF system with hysteresis similar to that of SFDB is used in the design procedure. The target performance parameteris considered in the design procedure includes the inter-story drift ratios and the brace ductility levels under design basis earthquakes. Design examples of 3-story and 6-story buildings are presented. The effectiveness of the proposed displacement-based design procedure was evaluated through both nonlinear pushover and time history analyses of the designed buildings under several selected suites of ground motions.
- Chapter 7 presents the main conclusions of this research. The limitations of current work and proposed future work along this research direction are also discussed in this chapter.

CHAPTER 2 SMA WIRE TESTING

2.1 INTRODUCTION OF SHAPE MEMORY ALLOY

In the past decade, passive dampers which utilize shape memory alloys (SMA) for energy dissipation have attracted growing interest from civil engineering communities, especially for seismic hazard mitigation application. SMA refers to a unique group of alloys with the ability to return to some pre-defined shape when subjected to an appropriate thermal-mechanical procedure (Duerig et al. 1990; Shaw and Kyriakides 1995; Birman 1997). This shape recovery or shape memory effect is due to micromechanical phase transformation. The hysteretic behaviors of SMA materials can be adjusted by altering the material composition and heat treatment procedure. The hysteretic behavior of SMA materials is dependent on their composition as well as thermal conditions.

SMAs generally demonstrate two types of unique behavior at different temperatures. For example, at ambient temperatures $T < M_f$, where M_f refers to martensite finish temperature, the microstructure of SMA materials is fully martensitic and SMA exhibits a large hysteresis loop similar to other conventional metal alloys such as mild steel, but the residual deformation after unloading can be fully recovered by an increase in temperature (as shown in Figure 2.1-(a)). This shape recovery effect is called shape memory effect, which is due to a micromechanical phase transformation from the martensite phase to the parent austenite phase. In this study,

another important characteristic of SMA materials – superelasticity or pseudoelasticity, which involves rate-dependent hysteretic damping with zero residual strain upon unloading, is utilized to dissipate vibration energy in structures. SMA exhibits the superelastic behavior at ambient temperatures $T > A_f$, where A_f is termed austenite finish temperature, above which the microstructure of SMA is fully austenitic. The superelastic behavior of SMA is due to a stress-induced solid phase transformation from austenite to martensite. Since martensite is stable only at the presence of the externally applied load, a reverse transformation takes place upon unloading, and after fully unloading, the material will return to its original undeformed shape (as shown in Figure 2.1-(b)).

Although there are many SMAs, such as Ti-Ni, Cu-Al-Ni, Cu-Zn-Al, Au-Cd, Mn-Cu, Ni-Mn-Ga, and Fe-based alloys, most of the practical SMAs are Ti-Ni-based alloys, since other SMAs are usually not ductile (or not ductile enough) or are of low strength and exhibit grain-boundary fracture (Otsuka and Kakeshita 2002). Ni-Ti-based alloys, usually called Nitinol, are superior to other SMA materials in many respects and are the most widely used SMA material at present. Their transformation temperatures such as the above-described M_f and A_f can be adjusted in the range from less than -100°C to over 100°C. Nitinol alloys tend to be much more thermally stable, have high corrosion resistance compared to other SMA materials, and have much higher ductility and excellent fatigue performance (both low-cycle and high-cycle fatigue). For example, Nitinol alloys have greater shape memory strain than the copper-based SMA materials (8% versus 4.5%). Furthermore, Nitinol alloys are available in the form of wires with a diameter as small as 25 μm. The prominent

properties of Nitinol materials have made them a promising candidate for use in energy dissipation device.

2.2 NITINOL WIRE TESTING

In this study superelastic Nitinol wires have been chosen as the core re-centering component in the SFDB device in consideration of its superior material properties. This section presents the experimental results of cyclic test of superelastic Nitinol wires, and some aspects important to engineering applications are also investigated through the tests, such as fatigue, recoverable strain, training effect, loading rate effect, temperature effect, etc.

2.2.1 Experimental Setup

The Nitinol wires tested in this study are products from two different manufacturers: Memry Corporation and Johnson Matthey, Inc, and they are designated as Type A (from Memry Corporation) and Type B (from Johnson Matthey, Inc) respectively. Both types of wires have a chemical composition (about 56% nickel and 44% titanium) to exhibit superelastic behavior at room temperature. The wire diameter is 0.58 mm (0.23 in) and the gauge length of the wire under tensile test is 254 mm (10 in). The cyclic tensile tests of superelastic Nitinol wires were carried out at Lehigh University using an MTS universal testing machine. A pair of wire grip fixtures made of aluminum was used in the test. One K-type thermocouple with a diameter of 0.0254 mm (0.001 in) was mounted on the test wire surface to measure its temperature during

the cyclic test. Figure 2.2 shows the setup for wire testing. The superelastic Nitinol wires were tested at various loading frequencies and maximum strain amplitudes in this study. All Nitinol wires were tested at a room temperature of 23ºC except for Section 2.2.6 in which the effect of ambient temperature were investigated.

In order to test Nitinol wires at lower temperatures, a temperature-controlled test chamber was in-house made and utilized to maintain the specified cold temperature. As shown in Figure 2.3, the temperature chamber measures 343 mm×292 mm×394 mm (13.5 in×11.5 in×15.5 in) and fits in the MTS universal testing machine being used. The schematic diagram of the temperature chamber is shown in Figure 2.4. Polystyrene foam with 1½ inch thickness was used to construct this temperature chamber, and the temperature process controller was configured to activate a solenoid valve for liquid nitrogen tank to maintain the cryogenic test condition. The temperature chamber is able to maintain a specified cold temperature down to -100ºC. with a temperature fluctuation of only about ±3ºC. The test temperature was monitored using a set of insulated thermocouples placed inside the temperature chamber.

2.2.2 Preliminary Test

The preliminary tests were conducted first to verify the data provided by manufacturer and provide testing parameters for formal tests of superelastic Nitinol wires. Figure 2.5 shows the stress-strain curves of both types of superelastic Nitinol wires from cyclic tests conducted at slow loading rates. The test program was conducted with a

constant strain rate of 7.0×10^{-5} sec^{-1} at an Instron 5567 universal testing machine. The superelastic Nitinol wires were not trained by cyclic preloading. The displacement amplitude increased with cycles until Nitinol wires fractured. Both wires show a similar hysteretic behavior during these tests.

It is seen in Figure 2.5 that the superelastic Nitinol wires under test can regain its initial length without permanent deformation when unloaded from strain amplitudes as high as 8%. This is because the yield-like plateau in Figure 2.5 for superelastic Nitinol wires is due to solid phase transformation instead of yielding. Thus below the 8% strain level, no damage can be observed in superelastic Nitinol wires. Beyond the 8% strain level, however, strain hardening occurs in superelastic Nitinol wires and noticeable residual strains after unloading can be observed due to plastic deformation of Nitinol wires. Thus, 8% strain is assumed to be the maximum recoverable strain level for the superelastic Nitinol wires used in this study. The ultimate strain of both superelastic Nitinol wires can reach up to 15%, which provides a reasonably large safety margin to Nitinol wires. The ultimate stress of both wires is about 1400-1500 MPa, which is almost three times the yield-like stress (i.e., the transformation stress from austenite to martensite). Such a significant strain hardening behavior of superelastic Nitinol wires may cause potential overloading to the adjoined members which needs special attention when designing SMA-based energy dissipation device.

2.2.3 Fatigue Life

The tests by Funakubo (1987) indicated that the high-cycle fatigue life of Nitinol under cyclic strain $\varepsilon_{max} = 0.02$ can reach as high as 1×10^5 cycles. However, the low-cycle fatigue life is of more interest for seismic application. In this study the fatigue life of superelastic Nitinol wire samples was tested under 8% strain cycles, a typical strain amplitude of Nitinol wires for earthquake engineering applications. The loading frequency is 1 Hz for the fatigue tests. Table 2.1 lists the experimentally determined values of the fatigue life of superelastic Nitinol wires, as well as a copper-based SMA material. It is seen that the superelastic Nitinol wires can withstand over 2000 cycles under 8% strain cycles. In comparison with the copper-based SMA wires, the superelastic Nitinol wires have much higher fatigue life despite their larger strain level during the fatigue test. Such a high fatigue life, as well as their large recoverable strain, enables superelastic Nitinol wires to sustain several strong earthquakes without the need of repair or replacement of SMA-based energy dissipation device if carefully designed. This reusability can considerably reduce the repair cost after earthquakes and is very appealing from a life-cycle cost perspective.

2.2.4 Training Effect

Figure 2.6 shows the change in material properties of Nitinol wires with increasing number of cycles. The wires were tested under 8% strain cycles at the loading frequency of 1 Hz. Figure 2.7 shows the changes in the hysteretic behavior of Nitinol wires (Type B) under cyclic loading. Observable changes include strain shift at zero

stress (i.e., after unloading), decrease of 'yield' stress (i.e., transformation stress of the upper transformation plateau) and hysteresis area, and increase of 'post-yield' stiffness as seen from the first eighty loading cycles. For example, the strain at zero stress ε_r shifts to 1.1% and 0.6% respectively for two different types of wires – Type A and Type B, and the 'yield' stress due to phase transformation decreases from 590 MPa in the 1st load cycle to 310 and 420 MPa respectively in the 80th load cycle for two different types of wires. Generally the degradation of the superelastic Nitinol wires of Type A is more substantial than the wires of Type B.

However, after the first 50-80 load cycles the hysteretic behavior of superelastic Nitinol wires stabilizes to its steady-state hysteresis loop. These observations are consistent with the findings by other researchers (e.g., Miyazaki 1990; McCormick et al. 2005). To overcome the potential problems in implementation that may arise from these observed degradation behaviors of superelastic SMA, training (i.e. cyclic preloading) of superelastic Nitinol wires should be performed before their use in energy dissipation device. Based on the above observations, superelastic Nitinol wires in this study were loaded for 80 loading cycles for training purpose before formal test or use to obtain a stable hysteretic behavior.

Figure 2.8 shows the hysteretic behavior of superelastic Nitinol wires after 80 cycles of training with peak strain equal to 8%. The loading frequency for this dynamic wire testing was equal to 2 Hz. The displacement-controlled test process is comprised of four separate load sequences with different strain amplitudes, and in each load sequence the wire was cyclically loaded at constant amplitudes for more than ten cycles. It is seen that stable hysteretic loops have been obtained after training

and no noticeable degradation effect such as residual deformation and change in transformation stresses, were observed in the formal test.

Although the hysteretic behaviors of the two types of superelastic Nitinol wires were similar before the training process (as shown in Figure 2.5), observable difference between their hysteresis occurred after the training (as shown in Figure 2.8). Compared with the Nitinol wires of Type A, the Nitinol wires of Type B have larger yield stress, flat transformation plateau and larger strain magnitude at the initiation of strain hardening.

2.2.5 Strain rate effect

In order to investigate the load-induced thermal effect on Nitinol wires, the results of the superelastic Nitinol wires (Type A) tested at various predetermined loading rates are presented in this section. Before the formal test, the Nitinol wires were trained by 80 cycles of preloading in order to minimize the accumulation of residual strain and stabilize its hysteretic behavior. Displacement control was used for the uniaxial tension test of Nitinol wires. The uniaxial tension test was carried out at six different loading frequencies - 0.001 Hz, 0.01 Hz, 0.1 Hz, 1 Hz, 2 Hz and 5 Hz for 7% strain cycles. In each test, Nitinol wire was cyclically loaded with constant strain rate at a strain amplitude of 7%. Accordingly, the strain rates are 1.4×10^{-4} sec^{-1}, 0.0014 sec^{-1}, 0.014 sec^{-1}, 0.14 sec^{-1}, 0.28 sec^{-1} and 0.70 sec^{-1} for the 0.001 Hz, 0.01 Hz, 0.1 Hz, 1 Hz, 2 Hz and 5 Hz loading frequencies, respectively. Figure 2.9 shows the typical stress-strain curve of superelastic Nitinol wires under six different loading frequencies

respectively. Figure 2.10 presents the experimental results of temperature variation in superelastic Nitinol wire specimens at three loading frequencies of 0.001 Hz, 0.01 Hz and 0.1 Hz respectively. Figure 2.10-(a), (b) and (c) show the temperature-strain profile for these three loading frequencies respectively, while Figure 2.10-(d) shows the corresponding time history of the wire specimen temperature. The temperature variation under higher loading frequencies was not measured due to the limitation of thermocouple measurement for this kind of use.

The test with a loading frequency of 0.001 Hz was a quasi-static test. During quasi-static test, the temperature change was negligible, and the slopes of both the upper and lower transformation plateau in the stress-strain curve are essentially horizontal. Compared with the quasi-static test results, the slope of the loading and unloading plateaus becomes increased and the amount of energy dissipation (i.e. the enclosed hysteresis area in each cycle) gets reduced for the dynamic test results. The increased slope of loading/unloading plateau (or post-'yield' stiffness) which is often considered a favorable effect for seismic applications is caused by the self-heating phenomena due to latent heat. The austenite to martensite phase transformation in the loading path is exothermic, while the martensite to austenite phase transformation in the unloading path is endothermic. Therefore, the loading path is accompanied with a rise in wire temperature while the unloading path is associated with a temperature drop (as shown in Figure 2.10). Such a temperature variation in each cycle results in the observed increase in the post-'yield' stiffness. For quasi-static tests, nonetheless, temperature fluctuation is negligible which leads to relatively flat transformation plateau.

It is also seen in Figure 2.9 that under certain loading frequencies the hysteresis loops of superelastic Nitinol wires are not stable in the first several load cycles. The shift direction of the hysteretic loops is indicated in Figure 2.9. This trend can also be observed in Figure 2.11 which shows the stress-strain curve for the 1^{st} and 10^{th} cycle corresponding to a variety of loading frequencies. For example, in terms of the stress-strain curves corresponding to the first cycle of dynamic tests, only slight differences exist among the hysteretic loops with the loading frequencies varying from 1 Hz to 5 Hz, but noticeable differences among the hysteretic loops corresponding to the tenth cycle for the same loading frequencies can be clearly observed in Figure 2.11-(b). Compared with the first cycle, the hysteresis loops of the tenth cycle shift downwards for the loading frequencies of 0.1 Hz and 1 Hz, while the hysteresis loop shifts upwards for the loading frequency of 5 Hz; for the loading frequency of 2 Hz and quasi-static loading, the hysteresis loops of the first and tenth cycles are almost identical. The energy dissipation capacity is slightly reduced with the increasing number of loading cycles for all loading frequencies considered. It is noted that the tenth cycle of hysteresis loop is quite stable and repeatable in the subsequent cycles except for the loading frequency of 5 Hz. At the loading frequency of 5 Hz the successive loading after the tenth loading cycle makes the hysteresis loop continue to shift upwards.

The variation in the hysteretic shapes was attributed to the temperature change associated with the increasing number of loading cycles. According to energy equilibrium, the absorbed specific heat has to be equal to the latent heat generation and mechanical energy dissipation, subtracted by the heat loss to the surrounding

environment. After a superelastic Nitinol wire is fully unloaded, the latent heat generation is zero. If the heat generated by mechanical energy dissipation has different values than the heat loss in one cycle, the temperature at zero strain will be different at the start and end of this particular cycle. Such a variation of zero-strain temperature results in the shift of hysteresis loops with the increasing number of loading cycles until the mechanical energy dissipation is equal to the heat loss in one cycle, i.e., the temperature cycles get stabilized. For example, for the wire test results shown in Figure 2.9, the zero-strain temperature drops in the first several cycles for loading frequency of 0.1 Hz and 1 Hz, and rises for the loading frequency of 5 Hz. The zero-strain temperature does not differ much for the loading frequency of 2 Hz, which leads to quite repeatable hysteretic loops at this loading rate. Under the slow loading frequencies (0.001 Hz and 0.01 Hz), temperature variation is very small and the hysteresis loop is quite repeatable. As a result, such temperature cycles cause the shift of hysteresis loops correspondingly in the first several load cycles since the transformation stress is also dependent on the wire temperature. The relationship between the temperature and hysteresis behavior of superelastic Nitinol wires will be discussed in the next section.

In summary, the temperature change in superelastic wires under dynamic loading not only leads to the variation of hysteresis loops at different loading frequencies, but also leads to the variation of hysteresis loops with the increasing number of cycles under the same loading frequency. It is noted that the loading frequency from 0.1 Hz to 5 Hz is typically the range of interest for seismic application. In light of the above discussion, it is seen that the thermo-mechanical effect of superelastic Nitinol wires

needs to be carefully evaluated for nonlinear dynamic analyses since important material properties of Nitinol such as the 'post-yield' stiffness, 'yield' strength and energy dissipation all vary with loading rates, which may influence the accuracy in predicting the seismic response of structures equipped with SMA-based energy dissipating devices.

2.2.6 Temperature Effect

Figure 2.12 shows the hysteresis behavior of superelastic Nitinol wires (Type A) at different ambient temperatures: 24ºC (room temperature), 16ºC, 8ºC and 0ºC. The wires were tested at the loading frequency of 1 Hz using the experimental setup shown in Figure 2.4. Before formal tests, all Nitinol wire specimens were trained by 80 cycles of preloading in order to minimize the accumulation of residual strain and stabilize hysteretic behavior. It is seen that the hysteresis loop of superelastic Nitinol wires shift downwards with the decrease of the ambient test temperature. The stresses at 2% strain on both the upper transformation plateau and lower transformation plateau were recorded, denoted as σ_U and σ_L respectively, and their variation pattern with the change of ambient temperature is shown in Figure 2.12-(b). Almost linear relation is observed between the stress and ambient test temperature.

Thus the transformation stress of superelastic Nitinol is strongly dependent on ambient temperature. The Nitinol wires tested in this study exhibits the superelastic behavior as long as the ambient temperature is above 0ºC. However below 0ºC they would be partially or completely martensite and lose their re-centering properties,

namely, permanent deformation would take place after unloading. Therefore, this type of Nitinol wires is not suitable for outdoor applications if its superelastic behavior is desired. Other superelastic SMA materials applicable for cold environment use need to be used for cold temperatures. However, in this study the Nitinol-based SFDB is intended to be installed inside buildings and thus is anticipated not to subject to low temperature.

2.3 CONCLUSIONS

This chapter presents the test results of superelastic Nitinol wires which form the core re-centering component of SFDB devices. This experimental study on superelastic Nitinol wires has led to the following findings:

- Superelastic Nitinol wires can recover their initial length with certain amount of energy dissipation when unloaded from deformation as high as 8% strain. They can also sustain over 2000 cycles under 8% strain cycles. Such a high fatigue life and large recoverable strain enables superelastic Nitinol wires to withstand several strong earthquakes without the need of replacement if carefully designed and implemented for SMA-based energy dissipation devices.
- The degradation of superelastic Nitinol wires occurs in the first several load cycles, including accumulation of residual strain and decrease of 'yield' stress (i.e., transformation stress). Therefore a training process that involves cyclic preloading for a specified number of load cycles, needs to be performed before their formal use in energy dissipation devices. The test results indicate that the

training process can effectively minimize accumulation of residual strain and stabilize the hysteretic behavior of superelastic Nitinol wires.

- The transformation stress of superelastic Nitinol wires decreases with the drop of ambient temperature.
- The temperature variation in superelastic Nitinol wires under dynamic tests not only leads to the variation in hysteretic behaviors at different loading frequencies, but also causes the shift of hysteretic loops with the increasing number of cycles under the same loading frequency. This rate-induced thermo-mechanical effect needs to be carefully considered for applications involving SMA-based energy dissipating devices.
- The superelastic Nitinol wires considered in this study lose the re-centering behavior if loaded beyond 8% strain. Furthermore, their application in low temperature application is limited due to the transformation temperature values for this particular Nitinol alloy.
- The maximum strength of superelastic Nitinol wires right before fracture is considerably higher than their transformation stress (i.e., 'yield' strength). The potential overloading to the adjoined members such as brace connections due to this strain hardening phenomenon should be carefully considered in the design of Nitinol-based energy dissipation device.

Table 2.1 Number of cycles to failure of SMA wires

Specimen No.	Material	Strain amplitude	# of cycles to fracture
1	Nitinol wire (Type A)	8%	2610
2	Nitinol wire (Type B)	8%	2515
3	Nitinol wires (Type B)	8%	2335
4	Cu-Al-Be wire	3%	90
5	Cu-Al-Be wire	3%	43

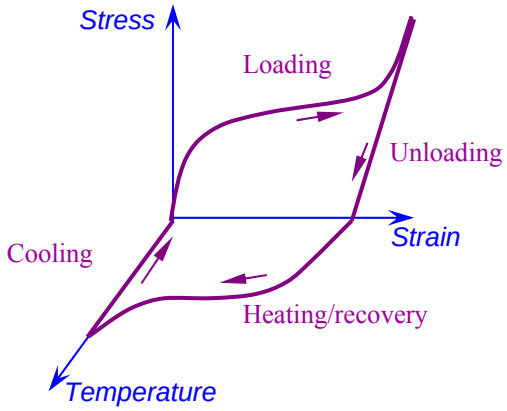

(a) Shape memory effect

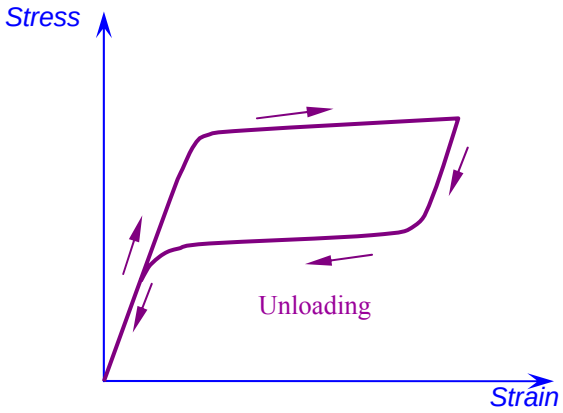

(b) Superelastic effect

Figure 2.1 Typical hysteresis of shape memory alloy materials

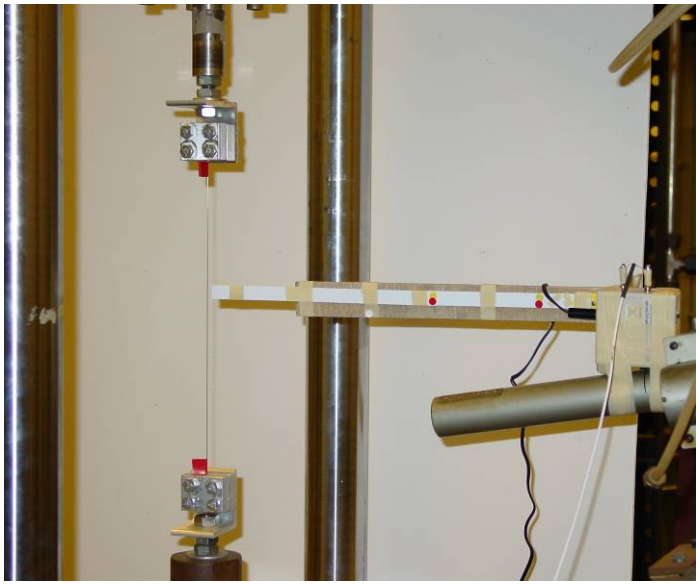

Figure 2.2 View of test setup for cyclic test of superelastic NiTi wire

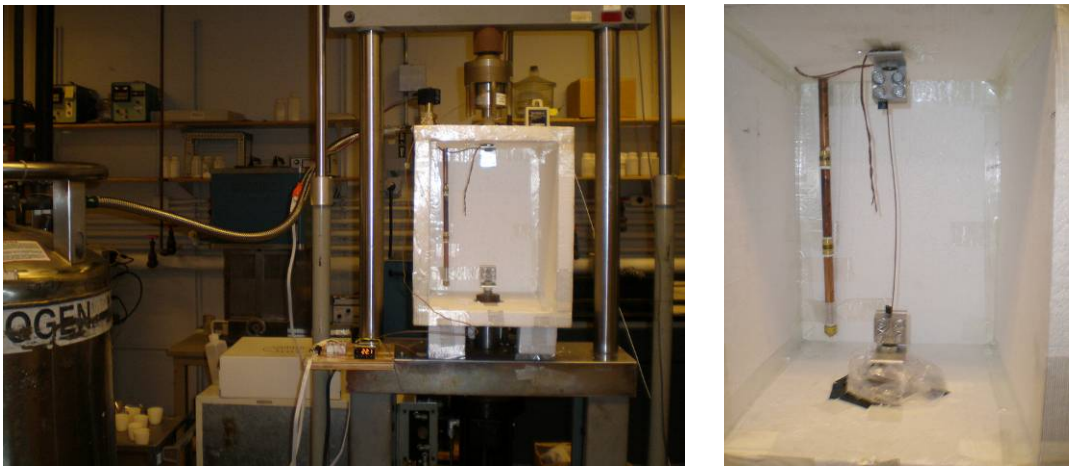

Figure 2.3 View of temperature-controlled test chamber

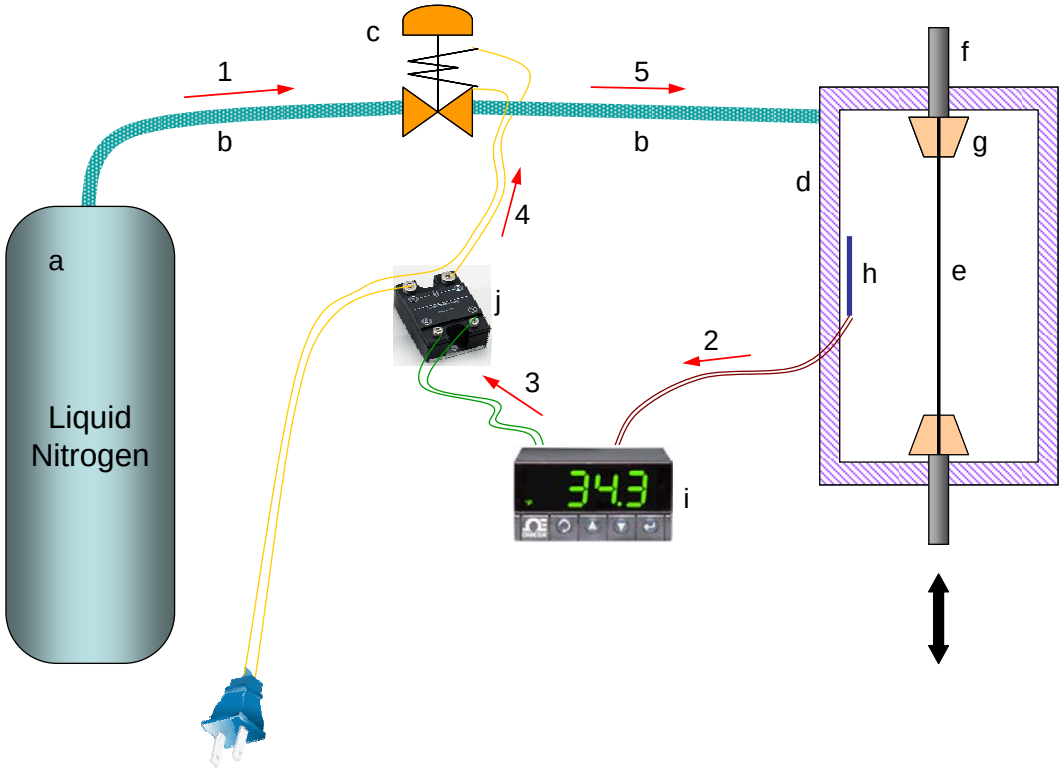

Legend of Figure 2.4

a. Liquid nitrogen tank
b. Cryogenic hose
c. Cryogenic solenoid valve (normally closed)
d. 1 ½" thick polystyrene foam temperature chamber
e. Nitinol wire
f. MTS testing machine
g. Aluminum wire grips
h. K-type thermocouple
i. Temperature process controller
j. Solid state relay

1. Liquid nitrogen valve is opened, cold liquid nitrogen passes through cryogenic hose and is stopped by the normally closed solenoid valve
2. Thermocouple reads temperature inside box; the temperature reading is sent to the temperature controller
3. If temperature is above set point (0ºC) the temperature process controller send a signal to the solid state relay which activates
4. Upon activation of the solid state relay the solenoid valve is then activated and opened
5. Cold nitrogen which is now in the gas phase rushes into the temperature chamber

Figure 2.4 Schematic diagram of test-setup with temperature chamber

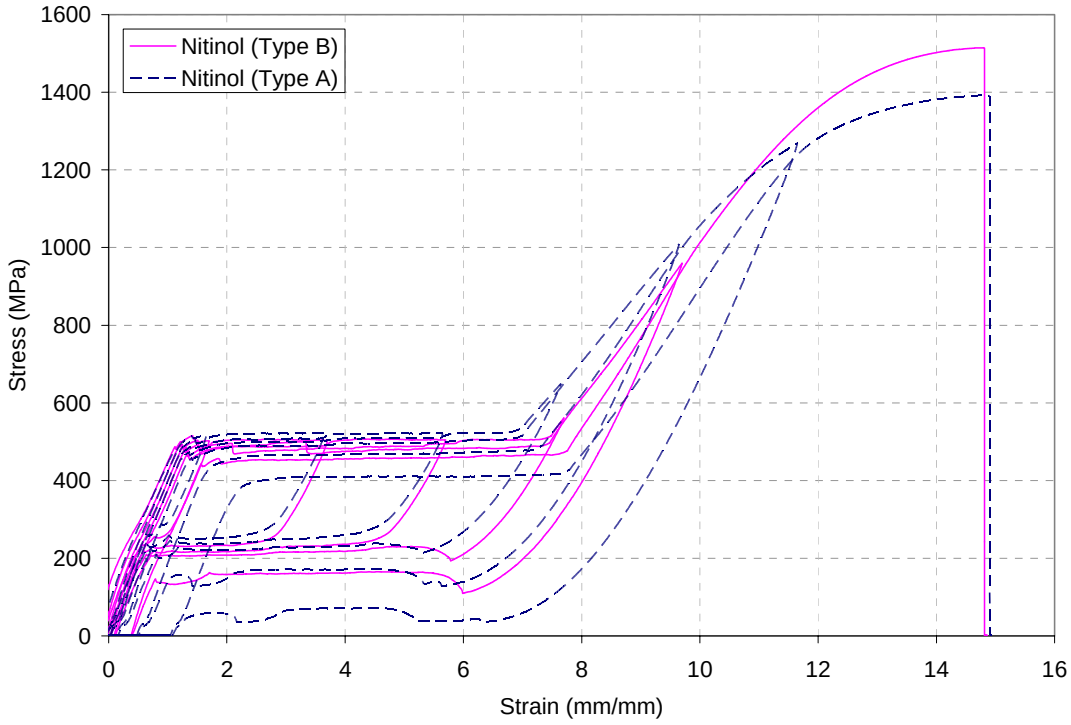

Figure 2.5 Cyclic quasi-static test of Nitinol wires with increasing amplitude

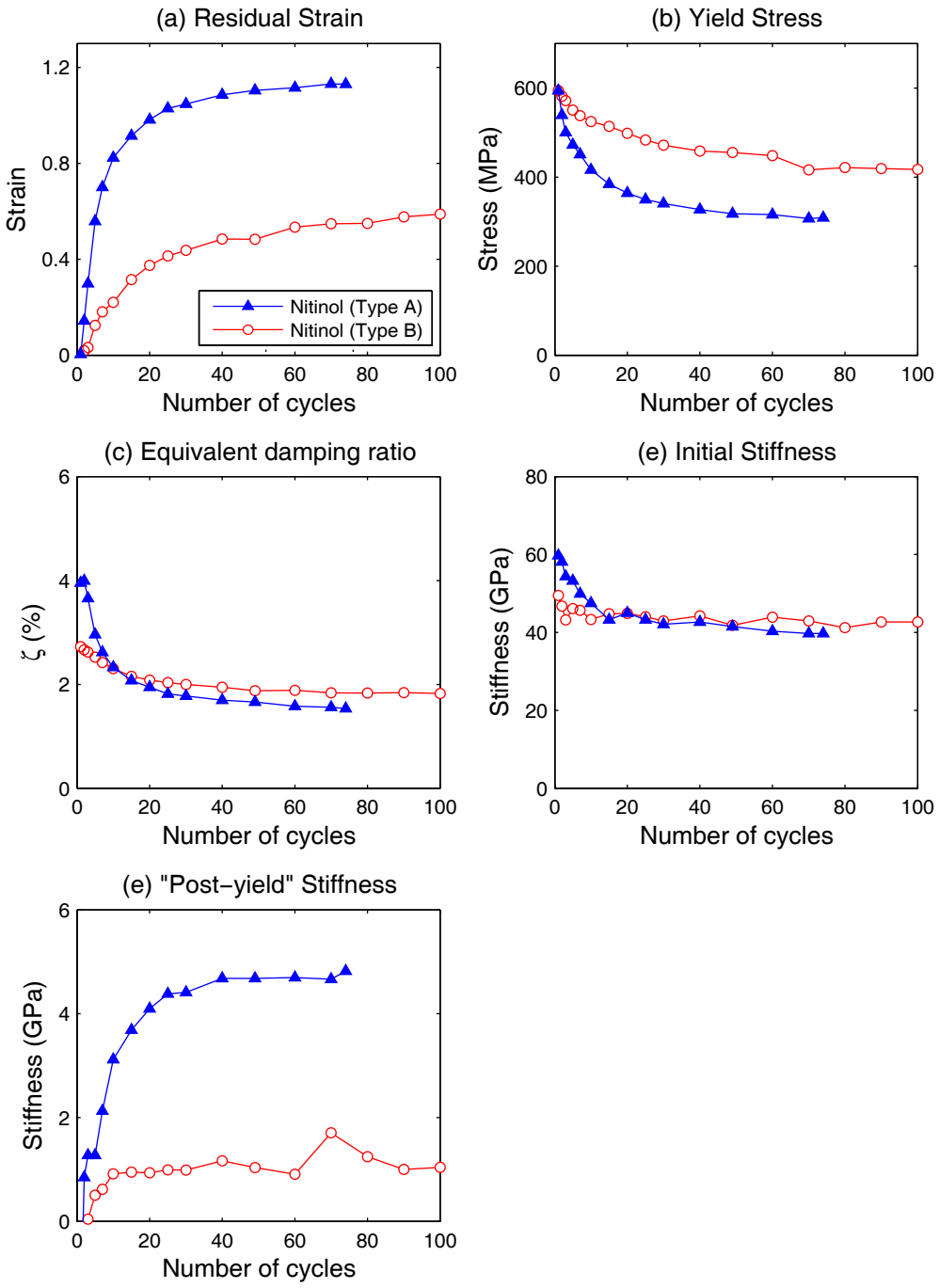

Figure 2.6 Change of material properties of Nitinol wire with increasing number of cycles

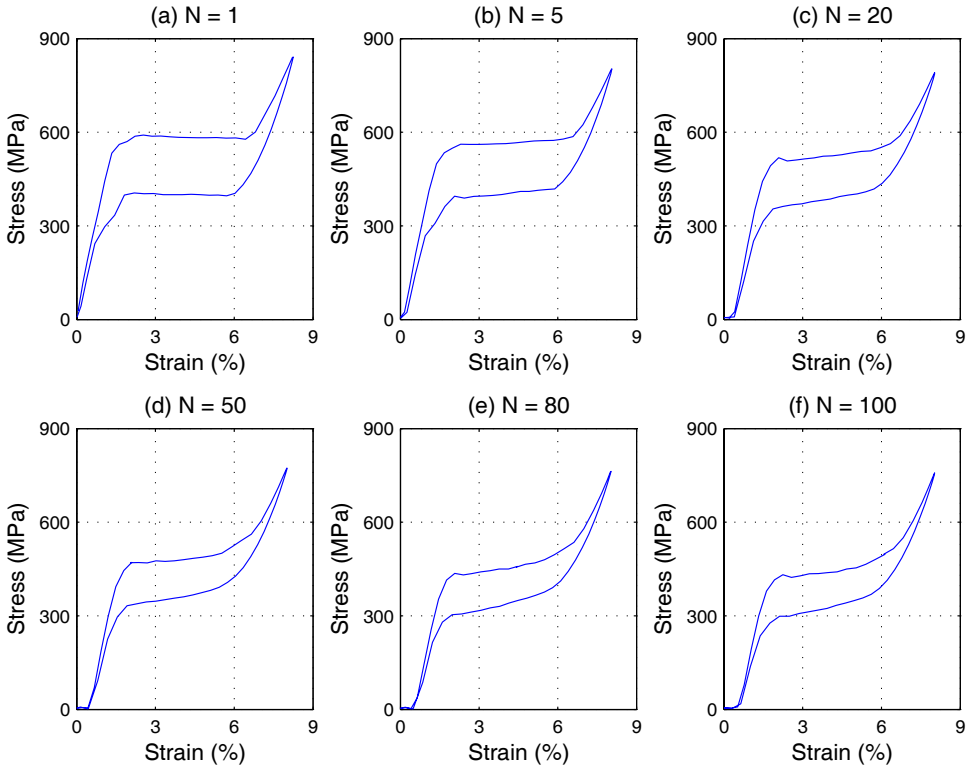

Figure 2.7 Cyclic effect on the hysteretic behavior of superelastic Nitinol wire (Type B)

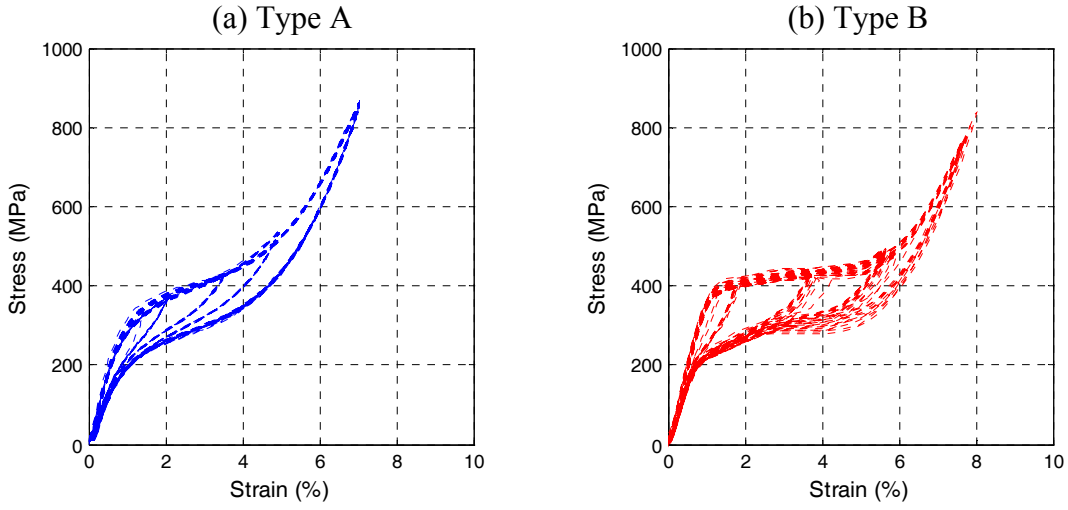

Figure 2.8 Cyclic behavior of Nitinol wires after training at loading frequency of 2 Hz

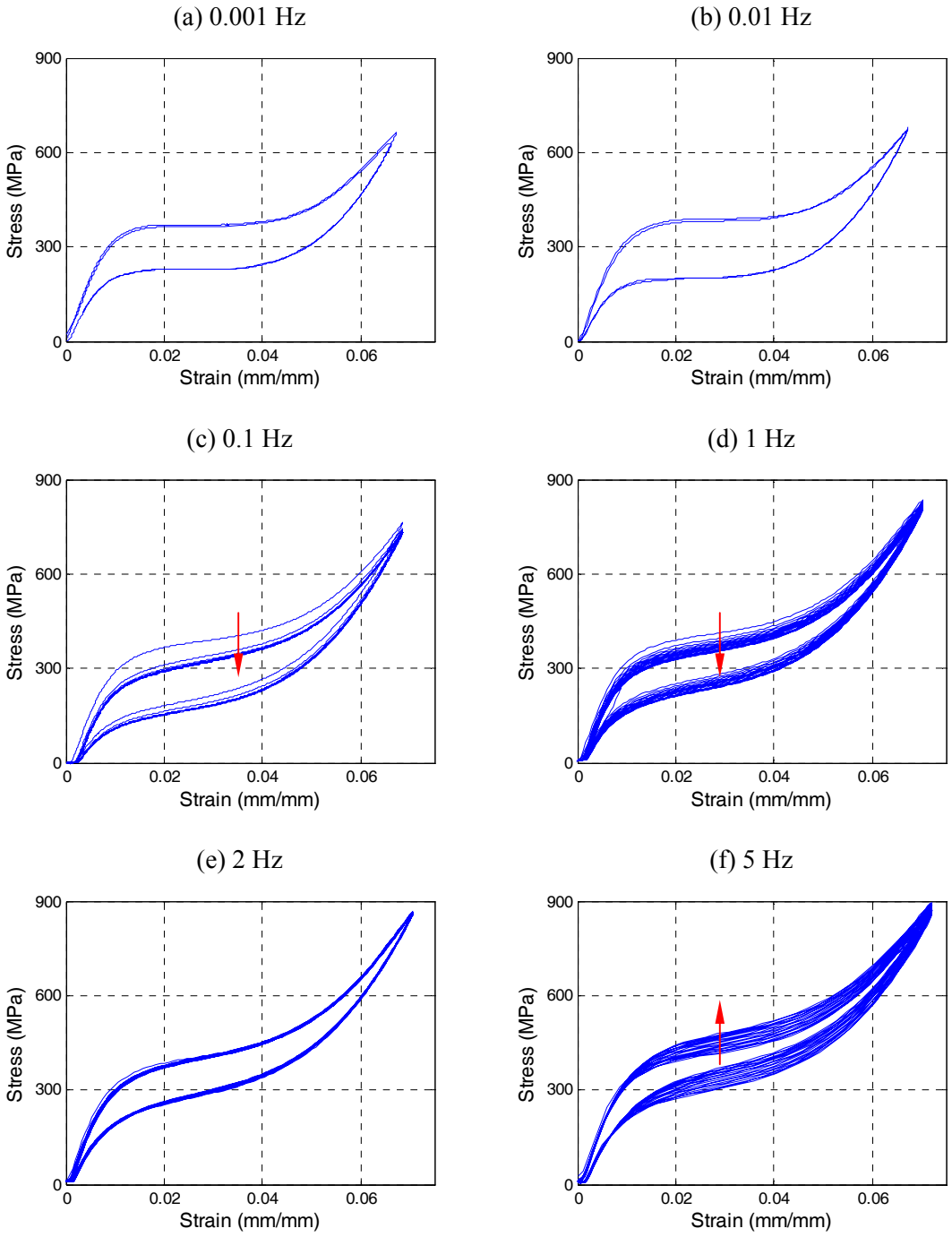

Figure 2.9 Stress-strain curve of superelastic Nitinol wires (Type A) at various loading frequency

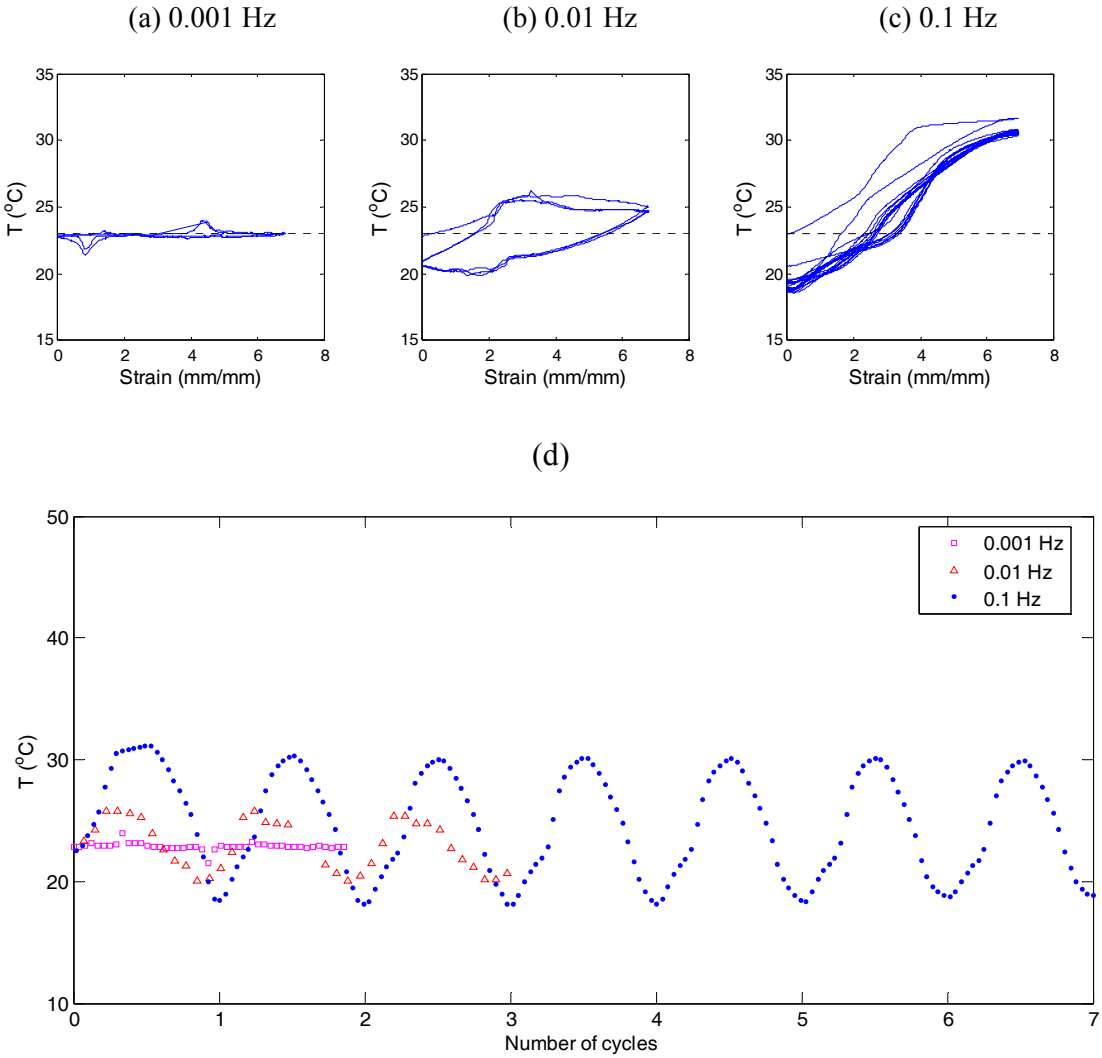

Figure 2.10 Temperature variation of superelastic Nitinol wires (Type A) during the loading process

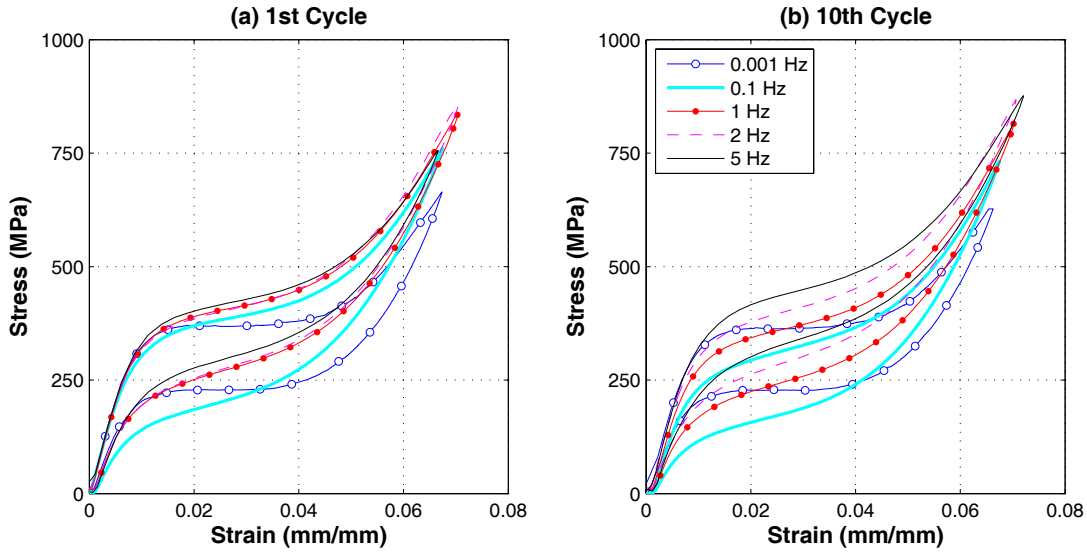

Figure 2.11 Stress-strain curve of Nitinol wires (Type A) for 1st and 10th cycles under different loading rates

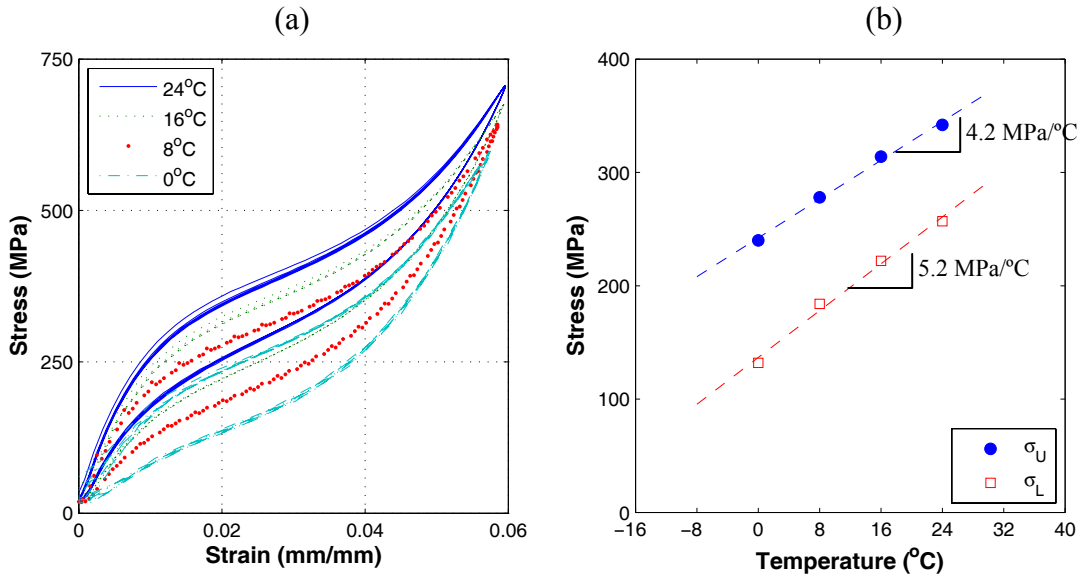

Figure 2.12 Temperature effect on the hysteretic behavior of superelastic Nitinol wires (Type A): (a) stress-strain curves at various ambient temperatures; (b) stress-strain relationship (where σ_U = stress on upper plateau corresponding 2% strain, σ_L = stress on lower plateau corresponding 2% strain)

CHAPTER 3 CONSTITUTIVE MODEL FOR SUPERELASTIC SMA WIRES

3.1 INTRODUCTION

Shape memory alloys (SMA) as a promising 'smart' material have found an increasing use in aerospace, civil, mechanical and biomedical applications. Due to the nature of stress-induced martensitic transformation, research and application of shape memory alloys have generally been one-dimensional in order to obtain maximal recoverable deformation. The applications of SMA materials and the need for a design tool have motivated a number of macroscopic constitutive models for these materials that accurately describe the mechanical behavior of SMAs. The macroscopic mechanical behavior of SMAs is usually modeled following either a phenomenological or a micromechanical approach (Brocca et al. 2002). Micromechanics based model are much more complicated than phenomenological models and usually are computationally demanding. Phenomenological models are often ad hoc descriptions aimed at fitting experimental data and are usually quite accurate in predicting the uniaxial response of SMAs.

Two one-dimensional constitutive models for superelastic SMA wires are proposed in this chapter. One is a thermo-mechanical constitutive model which can fairly accurately predict the strain-rate dependent behavior of superelastic SMA wires

under various loading rates. This model is derived in a thermo-dynamics framework and overcomes the limitations of most previously proposed constitutive models for SMA wires in capturing the rate-dependent mechanical behaviors in this frequency range of interest for seismic applications. The other is a rate-independent phenomenological model which is called modified Wilde model. Compared with the thermo-mechanical model, the modified Wilde model has relatively simpler mathematical expression and is appealing for seismic application for the sake of its convenience. These two constitutive models provide the useful tool to the numerical simulation of hysteretic behavior of SMA-based devices.

A comparative study of two nonlinear constitutive models for superelastic SMA wires is also conducted in this chapter in order to investigate the feasibility of using rate-independent constitutive model for superelastic SMA in seismic analyses of structures. Seismic analysis results of single-degree-of-freedom (SDOF) systems with superelastic SMA resistant element and one 6-story building with self-centering friction damping braces are presented in the comparative study.

3.2 THERMOMECHANICAL MODEL

3.2.1 Introduction

The experimental evidences in previous chapter indicate that varying loading rates generally lead to variation in the hysteretic and thermal behaviors of SMA. Such a rate-induced thermo-mechanical effect has drawn attention in seismic applications where the dynamics of SMA-based energy dissipation devices and structures is of

interest. In order accurately capture this thermo-mechanical effect, rate-dependent constitutive models for SMA have been studied in the past decade by researchers (e.g. Prahlad and Chopra 2003; Boyd and Lagoudas 1998; Auricchio et al. 1999, 2006; Brocca et al. 2002). Among them, uniaxial thermo-mechanical models are most suitable for engineering practice, because they make use of measurable quantities as parameters and are often relatively simple.

A uniaxial quasi-static constitutive model was proposed by Tanaka (1986) based on thermodynamics considerations. The Tanaka model was modified by Liang and Rogers (1990) and Brinson (1993) to overcome the limitation of the original model. Both Liang-Rogers model and Brinson model are applicable to quasi-static loading case. The Brinson model was further modified by Prahlad and Chopra (2003) to consider strain-rate dependent behavior of SMA. In the Prahlad-Chopra model, the original models are coupled with an additional energy balance Equation in order to reflect the thermal effect of strain rate.

The typical frequency range of interest to seismic application is from 0.1 Hz to 5 Hz. However, most previously proposed 1-D thermo-mechanical models for SMA materials have limitations in capturing all the rate-dependent mechanical behaviors in this frequency range, such as the variation of hysteretic shape, transformation plateau, energy dissipation and temperature at different loading rates. Therefore, an improved thermo-mechanical constitutive model is proposed in this section, which can fairly accurately predict the strain-rate dependent behavior of superelastic SMA wires in the loading rate range of interest to civil engineering application. This phenomenological constitutive model was derived within a thermo-mechanical framework and comprised

of three key components – a mechanical law governing the stress–strain behavior, an energy balance equation that reflect the rate-dependent thermal effect and a transformation kinetics rule that describes the evolution of the phase fraction as a function of stress. The mathematical expression of this thermo-mechanical model is described as follows.

3.2.2 Thermodynamics Formulation

The Tanaka's approach (Tanaka 1986) to the derivation of the constitutive law of shape memory alloys have been used extensively in which the one-dimensional tensile behavior of SMAs was considered. From the first and second law of thermodynamics, the energy balance and the Clausius-Duhem inequality in the current configuration can be expressed as,

$$\rho \dot{u} - \hat{\sigma} L + \frac{\partial q_{sur}}{\partial x} - \rho q = 0 \tag{3-1}$$

$$\rho \dot{\eta} - \rho \frac{q}{T} + \frac{\partial}{\partial x}\left(\frac{q_{sur}}{T}\right) \geq 0 \tag{3-2}$$

where u and η represent the internal energy density and the entropy density, i.e. the internal energy and entropy per unit mass respectively, q and q_{sur} represent the heat production and the heat flux, T, x and ρ represent the temperature, the material coordinate and the density in the current configuration, $\hat{\sigma}$ and L represent the Cauchy stress and velocity gradient. It is assumed by Tanaka (1986) that the thermo-mechanical process of SMA can be fully described by a set of state variables (ε, T, ξ),

where ε is the Green strain and ξ is an internal variable which is often defined as the fraction of martensite.

For one-dimensional small deformation case, the reference configuration and the current configuration is no longer distinguished in this paper. By introducing the Helmholtz free energy density $\psi = u - T\eta$, Equations (3-1) and (3-2) can be rewritten as,

$$\rho_0(\dot{\psi} + \dot{T}\eta + T\dot{\eta}) - \sigma\,\dot{\varepsilon} + \frac{\partial q_{sur}}{\partial X} - \rho_0 q = 0 \tag{3-3}$$

$$(\sigma - \rho_0 \frac{\partial \psi}{\partial \varepsilon})\dot{\varepsilon} - (\eta + \frac{\partial \psi}{\partial T})\dot{T} - \frac{\partial \psi}{\partial \xi}\dot{\xi} - \frac{1}{\rho_0 T} q_{sur} \frac{\partial T}{\partial X} \geq 0 \tag{3-4}$$

where the Helmholtz free energy density ψ is a function of state variables (ε, T, ξ), ρ_0 and X represent the material density and coordinate in the reference configuration, σ is the second Piola-Kirchhoff stress which is energy conjugate to the Green strain. From the thermodynamics of continuous media, the coefficients of $\dot{\varepsilon}$ and $\dot{T}$ should vanish in Equation (3-4). Thus the above inequality provides the constitutive equations as:

$$\sigma = \rho_0 \frac{\partial \psi}{\partial \varepsilon} \tag{3-5a}$$

$$\eta = -\frac{\partial \psi}{\partial T} \tag{3-5b}$$

Additionally, $\mathcal{A} \equiv -\rho_0 \frac{\partial \psi}{\partial \xi}$ is the driving force of transformation which is conjugate to the internal variable ξ. Here Equation (3-5a) describes the stress-strain relationship and is thus called mechanical law in this study. The rate form of the above constitutive equations can be obtained by differentiating Equation (3-5),

$$\dot{\sigma} = E\dot{\varepsilon} + \Theta\dot{T} + \Omega\dot{\xi}\,, \quad \rho_0\dot{\eta} = -\Theta\dot{\varepsilon} + c\dot{T} + \Gamma\dot{\xi} \tag{3-6}$$

where E, Θ, Ω , c, and Γ are material constants as defined by the following equations,

$$E \equiv \rho_0 \frac{\partial^2 \psi}{\partial \varepsilon^2}, \quad \Theta \equiv \rho_0 \frac{\partial^2 \psi}{\partial \varepsilon \cdot \partial T}, \quad \Omega \equiv \rho_0 \frac{\partial^2 \psi}{\partial \varepsilon \cdot \partial \xi} = -\frac{\partial \mathcal{A}}{\partial \varepsilon}$$

$$c \equiv -\frac{\partial^2 \psi}{\partial T^2}, \quad \Gamma \equiv -\frac{\partial^2 \psi}{\partial T \partial \xi}$$

which are, in general, functions of the state variables (ε, T, ξ). The rate form of the Helmholtz free energy density can be expressed as,

$$\rho_0\dot{\psi} = \sigma\dot{\varepsilon} - \rho_0\eta\dot{T} - \mathcal{A}\dot{\xi} \tag{3-7}$$

By substituting Equation (3-7) into Equation (3-3), the energy balance Equation can be rewritten as

$$\mathcal{A}\dot{\xi} = \rho_0 T\dot{\eta} + \frac{\partial q_{sur}}{\partial X} - \rho_0 q \tag{3-8}$$

The term $\mathcal{A}\dot{\xi}$ represents an internal power which in the case of an irreversible evolution is entirely dissipated inside the system instead of being developed against the exterior (Maugin 1999). It can be seen that both the mechanical law and energy balance equations, i.e., Equations (3-6) and (3-8), involve the term $\dot{\xi}$, and thus the evolution of martensite fraction ξ has to be established too. The transformation kinetics will be presented in the next section. The mechanical law, the energy balance equation and the transformation kinetics collectively give a complete model for describing the constitutive relations of superelastic SMAs.

3.2.3 Constitutive Model with Constant Elastic Modulus

3.2.3.1 *Helmholtz free energy*

Similar to Sadjadpour and Bhattacharya (2006), the Helmholtz free energy density of superelastic SMAs is assumed here to be of the form below,

$$\psi = \frac{E}{2\rho_0}\varepsilon_{el}^2 + \frac{L}{T_{cr}}(T - T_{cr})\xi - C_p T \ln(\frac{T}{T_0}) \tag{3-9}$$

where ψ is the Helmholtz free energy per unit mass, ε_{el} is the elastic strain, T_{cr} and T_0 are thermodynamic transformation temperature and initial temperature respectively, E, L and C_p represent the elastic modulus, latent heat of phase transformation and specific heat of the material respectively, which are all assumed to be equal for both the austenite and the martensite here. The three terms in Equation (3-9) represent the effect of strain energy, latent heat of phase transformation and specific heat. The effect of pure-phase thermal expansion is neglected in this expression, because it is much smaller and negligible compared with the other three effects (Liang and Rogers 1990, Brinson 1993, Prahlad and Chopra 2003).

In the case of small deformation the strain of SMA material can be decomposed into two parts: $\varepsilon = \varepsilon_{el} + \varepsilon_{in}$, where ε_{el} is the thermo-elastic strain and ε_{in} is the inelastic strain due to phase transformation. Following Brinson (1993) and Auricchio and Sacco (2001), the inelastic and elastic strain can be expressed as

$$\varepsilon_{in} = \varepsilon_l \xi, \qquad \varepsilon_{el} = \varepsilon - \varepsilon_l \xi \tag{3-10}$$

where ε_l is the maximum residual strain which is generally considered as a time-independent material constant of SMAs. By substituting Equation (3-10), the Helmholtz free energy for superelastic SMAs can be rewritten as

$$\psi = \frac{E}{2\rho_0}(\varepsilon - \varepsilon_l \xi)^2 + \frac{L}{T_{cr}}(T - T_{cr})\xi - C_p T \ln(\frac{T}{T_0}) \tag{3-11}$$

where E, L, C_p and ε_l are all constants.

3.2.3.2 *Constitutive equation*

On combining Equations (3-5) and (3-11), we obtain the following constitutive equations,

$$\sigma = E\varepsilon - \varepsilon_l E\xi = E\varepsilon_{el} \tag{3-12a}$$

$$\eta = -\frac{L}{T_{cr}}\xi + C_p\left[1 + \ln\left(\frac{T}{T_0}\right)\right] \tag{3-12b}$$

$$\mathcal{A} = \varepsilon_l E(\varepsilon - \varepsilon_l \xi) - \frac{\rho_0 L}{T_{cr}}(T - T_{cr}) \tag{3-12c}$$

The mechanical law, i.e. Equation (3-12a), describes the stress-strain relationship which is consistent with previous quasi-static constitutive models such as those by Tanaka (1986), Liang and Rogers (1990), and Brinson (1993). Although this mechanical law was formulated from thermodynamic considerations, an alternative derivation can also be obtained based on the Voigt model in micromechanics (Brinson and Huang 1996). Figure 3.1 shows the Voigt model in which the austenite and martensite phases are in parallel while the transformed fraction is in series with these

two phases. The rate form of the constitutive equations can be obtained by differentiating Equation (3-12)

$$\dot{\sigma} = E\dot{\varepsilon} + \Omega\dot{\xi} \tag{3-13a}$$

$$\dot{\eta} = -\frac{L}{T_{cr}}\dot{\xi} + \frac{C_p}{T}\dot{T} \tag{3-13b}$$

where material property Ω is expressed as $\Omega = -\varepsilon_l E$.

3.2.3.3 *Energy balance equation*

During uniaxial tensile loading, the heat production q in superelastic SMAs is always zero. Additionally, a uniform temperature in the superelastic SMA wires can be assumed under uniaxial tensile loading (Vitiello et al 2005). Thus the heat flux is solely caused by heat transfer between SMA wire and surrounding environment due to temperature difference. The heat transfer equation can be described using the equation below,

$$Q = k \cdot (T - T_0) \tag{3-14}$$

where Q is the transient rate of heat flow; T and T_0 are the transient temperature of the SMA wire specimen under loading and environment temperature, respectively; and k is the heat transfer coefficient which should include not only the effect of heat convection but also the heat contact conduction between the wire specimen and the gripping fixture at the end of wire specimen. Here the temperature of the gripping fixture and environment is assumed to be a constant, T_0. The divergence of heat flux can be estimated from heat transfer per unit volume,

$$\frac{\partial q_{sur}}{\partial X} = \frac{k}{V}(T - T_0) \tag{3-15}$$

By substituting Equations (3-12) and (3-15) into Equation (3-8), the energy balance equation can be rewritten as,

$$\varepsilon_l E(\varepsilon - \varepsilon_l \xi)\dot{\xi} = \rho_0 C_p \dot{T} - \rho_0 L\dot{\xi} + \frac{k}{V}(T - T_0) \tag{3-16}$$

By considering Equations (3-10) and (3-12*a*), Equation (3-16) is rewritten as,

$$\sigma\dot{\varepsilon}_{in} = \rho_0 C_p \dot{T} - \rho_0 L\dot{\xi} + \frac{k}{V}(T - T_0) \tag{3-17}$$

Like the mechanical law, the Equation (3-17) can also be explained by Voigt model. As shown in Figure 3.1, under uniaxial loading the inelastic deformation occurs in the transformed fraction which is in series with the elastic part. Thus, for materials like superelastic Nitinol, only part of the mechanical input energy is stored in the form of elastic strain energy, the remaining part of the mechanical input energy is dissipated due to the inelastic deformation. Such energy dissipation usually contributes to the temperature variation in the SMA wire specimen under loading, and thus affects the material behaviors of SMA. The term $\sigma\dot{\varepsilon}_{in}$ in Equation (3-17) represents the time rate of mechanical energy dissipation due to the inelastic deformation; the term $\rho_0 L\dot{\xi}$ represents the rate of latent heat and the negative sign means the austenite to martensite transformation is exothermic, while the martensite to austenite transformation is endothermic. Thus Equation (3-17) means at any instant the heat generation due to the inelastic dissipation and latent heat is equal to the specific heat absorbed by the specimen plus the heat loss to the environment.

3.2.3.4 *Transformation kinetics*

Transformation kinetics of SMAs describes the evolution rule of martensite fraction ξ for both the transformation from austenite to martensite and the reverse transformation from martensite to austenite. Different transformation kinetics rules have been proposed by various researchers. The evolution of martensite fraction ξ is governed by the driving force $\mathcal{A}$ and temperature T, and thus the transformation kinetics can be expressed as a function of $\mathcal{A}$ and T (see, e.g. Auricchio and Sacco 2001; Sadjadpour and Bhattacharya 2005). It can be seen from Equation (3-12) that the driving force $\mathcal{A}$ can also be expressed by stress σ and temperature T. Because the stressed- and temperature-induced phase transformation of SMA was widely studied and the relationship of transformation stress and transformation temperature was well established, the empirical transformation kinetics which represent the martensite fraction as a function of stress and temperature are more frequently used, e.g., in the constitutive models derived by Tanaka (1986), Liang and Rogers (1990), Brinson (1993), and Wang et al (2006), Such empirical transformation kinetics offer good agreement with experimental data. In order to further improve the simulated behavior of superelastic SMAs, a modified version of Liang-Rogers transformation kinetics is used in this study of rate-dependent constitutive model. However, any transformation kinetics rule like those described above can be used in conjunction with the mechanical law and energy balance equation if so desired.

In the Tanaka model, an exponential function is used to describe the evolution of martensite fraction ξ. It is noted that if the reverse transformation occurred before the forward transformation is completely finished, i.e., $0 < \xi < 1$, the Tanaka's transformation equations would yield discontinuous results; therefore, a transformation kinetics rule like this can not be used to describe the inner loop behavior of superelastic SMAs. In the Liang-Rogers model, the transformation equation was modified and the martensite fraction ξ is described using a cosine function of stress and temperature instead of an exponential function. The inability of the Tanaka model to describe the inner loop behavior is overcome by this transformation kinetics. The evolution of martensite fraction during the phase transformation is defined by the equations below.

Austenite → Martensite: $\xi = \frac{1-\xi_0}{2}\cos[a_M(T - M_f - \frac{\sigma}{c_M})] + \frac{1+\xi_0}{2}$

$$\text{for } c_M(T - M_s) < \sigma < c_M(T - M_f) \tag{3-18a}$$

Martensite → Austenite: $\xi = \frac{\xi_0}{2}\cos[a_A(T - A_s - \frac{\sigma}{c_A})] + \frac{\xi_0}{2}$

$$\text{for } c_A(T - A_f) < \sigma < c_A(T - A_s) \tag{3-18b}$$

where the material constants a_M and a_A are defined as,

$$a_M \equiv \frac{\pi}{M_s - M_f}, \quad a_A \equiv \frac{\pi}{A_f - A_s}$$

ξ_0 is the initial martensite fraction at the beginning of the current transformation, and the transformation temperatures M_s, M_f, A_s and A_f are referred to the martensite start temperature, martensite finish temperature, austenite start temperature and austenite

finish temperature, respectively. The material constants c_A and c_M are the slopes of the critical stress-temperature curve (as shown in Figure 3.2-(a)). A typical hysteresis of superelastic SMAs is shown in Figure 3.2-(b). For quasi-static uniaxial loading of SMA wires, in which the material temperature remains the same as the environmental temperature T_0, the four characteristic stress in Figure 3.2-(b) can be expressed using these material constants,

$$\begin{aligned} \sigma^{Ms} &= c_M (M_s - T_0), \qquad \sigma^{M_f} = c_M (M_f - T_0) \\ \sigma^{As} &= c_A (A_s - T_0), \qquad \sigma^{A_f} = c_A (A_f - T_0) \end{aligned}, \tag{3-19}$$

However, the Liang-Rogers transformation kinetics is unable to capture the behavior of shape memory effect at temperatures below M_s. In the Brinson model (Brinson 1993), this transformation equation is further modified to overcome this defect by differentiating the stressed-induced and temperature-induced components in the martensite fraction, and as a result of this, the Brinson transformation kinetics rule takes a more complex form than the Liang-Rogers model. For superelastic applications, the martensite fraction is induced solely by stress, and it is unnecessary to distinguish between the twinned and detwinned variants of martensite. For simplicity, the Brinson transformation kinetics is not presented and studied in this paper. The transformation kinetics adopted in this study is modified from the Liang-Rogers model, and it does not differentiate the stressed-induced and temperature-induced components of the martensite fraction.

Based on the writers' research as well as those by Prahlad and Chopra (2001), it can be shown that the Liang-Rogers transformation kinetics results in relatively sharp transition at the points of critical stress, which is inconsistent with experimental data.

To achieve a smooth transition at critical stress, we propose to use a sigmoid function in the transformation kinetics equation. The sigmoid function is defined as,

$$\mathrm{sig}(x) \equiv \frac{1}{1+e^{-x}} \tag{3-20}$$

The evolution of martensite fraction can be expressed as

Austenite→ Martensite:

$$\xi = \xi_0 + (1-\xi_0)\cdot \mathrm{sig}\left[-a_M (T - T_M - \frac{\sigma}{c_M})\right] = \xi_0 + \frac{1-\xi_0}{1+e^{a_M (T - T_M - \frac{\sigma}{c_M})}} \tag{3-21a}$$

Martensite → Austenite:

$$\xi = \xi_0 \cdot sig\left[-a_A (T - T_A - \frac{\sigma}{c_A})\right] = \frac{\xi_0}{1+e^{a_A (T - T_A - \frac{\sigma}{c_A})}} \tag{3-21b}$$

where the critical temperatures T_M and T_A are defined as

$$T_M = \frac{M_s + M_f}{2}, \qquad T_A = \frac{A_s + A_f}{2}$$

The material constants c_M and c_A are as defined before, while the material constants a_M and a_A are defined here as

$$a_M = \frac{\ln(10000)}{M_f - M_s}, \qquad a_A = \frac{\ln(10000)}{A_f - A_s}$$

This results in a starting point and finishing point of transformation that corresponds to the martensite fraction of 0.01 and 0.99 respectively. The rate form of this transformation equation can be derived from Equation (3-21) as follows,

Austenite → Martensite:

$$\dot{\xi} = (1-\xi_0)\cdot(a_M\dot{T} - \frac{a_M}{c_M}\dot{\sigma})\cdot \mathrm{g}\left[a_M(T - M_f - \frac{\sigma}{c_M})\right] \tag{3-22a}$$

Martensite → Austenite:

$$\dot{\xi} = \xi_0\cdot(a_A\dot{T} - \frac{a_A}{c_A}\dot{\sigma})\cdot \mathrm{g}\left[a_A(T - A_s - \frac{\sigma}{c_A})\right] \tag{3-22b}$$

where the function g(.) is defined as

$$\mathrm{g}(x) \equiv \frac{-e^x}{(1+e^x)^2}$$

3.2.4 Constitutive model with non-constant elastic modulus

3.2.4.1 *Helmholtz free energy*

In previous derivation, all material functions are assumed constant. However, the Young's modulus E of SMA is experimentally found to be strongly dependent on the martensite fraction, ξ. To address this, the following expression was assumed for the Young's modulus by Liang and Rodgers (1990) as well as Sato and Tanaka (1988),

$$E(\xi) = E_a + \xi(E_m - E_a) \tag{3-23}$$

where constants E_a and E_m are Young's modulus for austenite and martensite respectively. Similar to Equation (3-11), the Helmholtz free energy can be accordingly expressed as

$$\psi = \frac{E(\xi)}{2\rho_0}(\varepsilon - \varepsilon_l\xi)^2 + \frac{L}{T_{cr}}(T - T_{cr})\xi - C_pT\ln(\frac{T}{T_0}) \tag{3-24}$$

where the Young's modulus $E(\xi)$ is described by Equation (3-23), and all material properties such as L, C_p and ε_l are constants. However, the constitutive model for non-

constant L, C_p and ε_l can also be derived with the same procedure as described in this section if so desired.

3.2.4.2 *Constitutive equation*

From Equations (3-5), (3-23) and (3-24), we obtain the following constitutive equations,

$$\sigma = E(\xi)\varepsilon - \varepsilon_l E(\xi)\xi = E(\xi)\varepsilon_{el} \tag{3-25a}$$

$$\eta = -\frac{L}{T_{cr}}\xi + C_p\left[1 + \ln\left(\frac{T}{T_0}\right)\right] \tag{3-25b}$$

$$\mathcal{A} = \varepsilon_l \cdot E(\xi) \cdot (\varepsilon - \varepsilon_l \xi) - \frac{E_m - E_a}{2}(\varepsilon - \varepsilon_l \xi)^2 - \frac{\rho_0 L}{T_{cr}}(T - T_{cr}) \tag{3-25c}$$

In the above equations, Equation (3-25*a*) has a similar form to Equation (3-12*a*), Equation (3-25*b*) is identical to Equation (3-12*b*), while Equation (3-26*c*) has a different form from Equation (3-12*c*) because of non-constant elastic modulus. It is noticed that the mechanical law, i.e., Equation (3-25*a*), is still consistent with the Brinson model with non-constant material properties and can be reconstructed by a special interpretation of the standard Voigt model (Brinson and Huang 1996). The ratio of the coefficients before ξ and ε in Equation (3-25*a*) has to be $-\varepsilon_l$ if the maximum residual strain ε_l is considered as a temperature-independent constant (Liang and Rogers 1990, Brinson 1993).

The rate form of constitutive equations are obtained by differentiating the two sides of Equation (3-25) simultaneously,

$$\dot{\sigma} = E(\xi)\dot{\varepsilon} + \Omega(\varepsilon, \xi)\dot{\xi} \tag{3-26a}$$

$$\dot{\eta} = -\frac{L}{T_{cr}}\dot{\xi} + \frac{C_p}{T}\dot{T} \qquad (3\text{-}26b)$$

where material property $\Omega(\varepsilon, \xi)$ is defined by

$$\Omega(\varepsilon, \xi) = -\varepsilon_l \cdot E(\xi) + (E_m - E_a)(\varepsilon - \varepsilon_l \xi)$$

In comparison with the case for constant elastic modulus, the rate form of mechanical law with non-constant elastic modulus is more complicated, although these two expressions have very similar form. The material property Ω is a function of both variables ε and ξ. Consequently, the ratio of material properties Ω to E is not equal to $-\varepsilon_l$.

3.2.4.3 *Energy balance equation*

With the similar assumption and procedure of section 2.2.3, we can obtain the energy balance equation as

$$\varepsilon_l E(\xi) \cdot (\varepsilon - \varepsilon_l \xi)\dot{\xi} + \frac{E_a - E_m}{2}(\varepsilon - \varepsilon_l \xi)^2 \dot{\xi} = \rho_0 C_p \dot{T} - \rho_0 L \dot{\xi} + \frac{k}{V}(T - T_0) \quad (3\text{-}27)$$

or

$$\sigma \dot{\varepsilon}_{in} + \frac{E_a - E_m}{2}\varepsilon_{el}^2 \dot{\xi} = \rho_0 C_p \dot{T} - \rho_0 L \dot{\xi} + \frac{k}{V}(T - T_0) \qquad (3\text{-}28)$$

The term on the left side of Equation (3-28) represents the energy dissipation rate, which can also be derived based on the Voigt model in micromechanics. Figure 3.3 shows the Voigt model and its parameters corresponding to time t and $t+dt$ respectively. The energy dissipation is equal to the mechanical work minus the increase of elastic strain energy, i.e.,

$$E_{dis} = \sigma \cdot d\varepsilon - \left[\tfrac{1}{2} E(\xi + d\xi) \cdot (\varepsilon_{el} + d\varepsilon_{el})^2 - \tfrac{1}{2} E(\xi) \cdot \varepsilon_{el}^2\right] \tag{3-29}$$

By ignoring second and higher order terms, the rate of energy dissipation reads

$$\frac{dE_{dis}}{dt} = \sigma \dot{\varepsilon}_{in} + \frac{E_a - E_m}{2} \varepsilon_{el}^2 \dot{\xi} \tag{3-30}$$

The first term, similar to the expression for constant elastic modulus, represents the mechanical work on the inelastic deformation. The second term represents the loss of elastic strain energy due to the increment $d\xi$, because the elastic modulus of austenite and martensite is different. The total energy dissipation in one cycle, i.e. the integration of Equation (3-30) over the time duration of one cycle, should be equal to the enclosed area of the hysteresis loop. The terms on the right-hand side of Equation (3-28) are the same as those of Equation (3-17). Thus Equation (3-28) has a similar physical interpretation as Equation (3-17), while it involves a more complex form for expressing the energy dissipation term compared with the case with constant elastic modulus.

3.2.4.4 *Transformation kinetics*

The transformation kinetics needs no modification for model with non-constant elastic modulus. Therefore the transformation equations described in Section 2.2.4 are still applicable for the model with non-constant elastic modulus.

3.2.5 Integration algorithm

Since the energy balance equation is in its rate form, it is convenient to use the rate form of the mechanical law and transformation kinetics too. The rate form of the constitutive model with non-constant elastic modulus comprised of Equations (3-26*a*), (3-27) and (3-22) is used for the numerical analyses in the next section.

For numerical simulation purpose, it is assumed that deformation time history is known a priori, and thus strain rate $\dot{\varepsilon}$ is also known at each time step. In order to solve for the three variants – σ, T and ξ, these three constitutive equations need to be integrated simultaneously. Each of these equations involves more than one term of $\dot{\sigma}$, $\dot{T}$ or $\dot{\xi}$ which are all unknowns for the current step. If these three equations is to be solved directly, the value of one of $\dot{\sigma}$, $\dot{T}$ or $\dot{\xi}$ from the previous step should be used first to solve the other two terms and then an iterative procedure has to be applied until specified precision is reached. This iterative method requests additional computing time and is not very efficient for dynamic analysis of large structural system with SMA based devices. However, it is noted that all three equations only involve the first power of $\dot{\sigma}$, $\dot{T}$ or $\dot{\xi}$. If we view these three equations as a set of simultaneous algebraic equations of $\dot{\sigma}$, $\dot{T}$ or $\dot{\xi}$, each rate form - $\dot{\sigma}$, $\dot{T}$ and $\dot{\xi}$ can be easily expressed in terms of variables σ, T and ξ, i.e., the constitutive equations can be rewritten into the form,

$$\begin{cases} \dot{\sigma} = f_1(\sigma, T, \xi, \varepsilon, \dot{\varepsilon}) \\ \dot{T} = f_2(\sigma, T, \xi, \varepsilon, \dot{\varepsilon}) \\ \dot{\xi} = f_3(\sigma, T, \xi, \varepsilon, \dot{\varepsilon}) \end{cases} \tag{3-31}$$

These differential equations are simultaneously solved using the 4^{th} order Runge-Kutta method in this study. This time integration method is still applicable even if other form of transformation kinetics equations (e.g., Tanaka 1986, Liang and Rogers 1990, Brinson 1993, Auricchio 2001) instead of Equation (3-22) is to be used.

3.2.6 Numerical Examples

In this section the simulation by the thermo-mechanical model is compared with the test results of superelastic Nitinol wires under different frequencies and different amplitude in order to verify the ability of this model to capture the rate-induced thermal effect under dynamic loading. The superelastic Nitinol wires tested in this study is a product of Memry Corporation with a diameter of 0.58 mm (0.025 in). Before the formal test, the Nitinol wires were trained by cyclic preloading in order to minimize accumulation of residual strain and stabilize its hysteretic behavior. More details of test program and corresponding results are presented in the Section 2.2.5.

The parameters of the constitutive model used in this study to simulate the superelastic behavior of Nitinol wires are given in Table 3.1. Using knowledge of these thermo-mechanical parameters, these model parameters were indirectly derived from the stress-strain curves of superelastic Nitinol wires obtained in the experimental study. Parameter values suggested by other researchers were taken into account when identifying the values of these model parameters. Because in the wire test program, relatively large aluminum gripping fixtures were used at both ends of the wire specimen, heat contact conduction as well as heat convection dominated the heat

transfer in the experiments. The test results of Nitinol coupon by Schmidt (2006) also suggested that the end of Nitinol specimen would remain at room temperature due to a strong heat exchange with the gripping fixture. In light of this observation, a value greater than the theoretical value which only considers the heat convection is chosen to achieve good agreement with experimental stress-strain data.

It is seen in Figure 3.4 that the presented thermo-mechanical constitutive model can predict the superelastic behavior of Nitinol wires quite well for a variety of loading rates. It is capable of capturing two major thermo-mechanical behaviors of superelastic Nitinol wires under varying loading rates – reduction of hysteresis area and thus energy dissipating capacity as well as increased slope of transformation plateau with increasing loading rates. It can also replicate the phenomenon of change in hysteresis loops with increasing number of load cycles, which is due to the temperature change in superelastic Nitinol wires. Notable discrepancy between the experimental results and simulation results can be observed in the hysteresis shape at large strains over 5%. This is due to the difference between the evolution of martensite fraction in the experiment data and that described by Equation (3-22) at large strains. More accurate but sophisticated transformation kinetics equations need to be used to minimize this discrepancy.

Figure 3.5 presents the experimental and simulation results of temperature change in superelastic Nitinol wire specimens. Figure 3.5-(a), (b) and (c) show the temperature-strain profile for loading frequencies of 0.001 Hz, 0.01 Hz and 0.1 Hz, respectively. The temperature variation under higher loading frequencies was not measured due to the limitation of thermocouple measurement in the test. Figure 3.5-(d)

shows the time history of the wire specimen temperature from both the experimental and numerical results. It is seen that the proposed constitutive model can properly predict the trend of temperature change in superelastic Nitinol wires: negligible temperature fluctuation under quasi-static loading (0.001 Hz); slight cooling down at medium loading frequency (0.01 Hz, 0.1 Hz) and slight heating up at further increased loading frequency (5 Hz). This cooling or heating trend caused the hysteresis loops to shift downwards or upwards with increasing number of load cycles until the temperature cycles are stabilized (as shown in Figure 3.4). Although the simulated temperature agrees fairly well with the test results for the loading frequencies of 0.001 Hz and 0.01 Hz, the simulation seems to over-predict the temperature variation at the loading frequency of 0.1 Hz. Such a discrepancy may arise from either inaccuracy of the identified model parameters or error in temperature measurement.

The energy dissipation capacity of superelastic SMA is crucial to its effectiveness in damping out structural vibration. Recent research in SMA-based damping devices found that for such applications the slope of transformation plateau of superelastic SMA also affects the control effectiveness such as reduction of maximum and residual story drift in building structures under earthquake loading. Experimental results show that these two properties of superelastic Nitinol wires are loading-rate dependent. It is thus desirable for a constitutive model to capture the effect of loading rate on these two properties –equivalent damping ratio and the stiffness ratio of transformation plateau. The equivalent damping ratio is defined as the energy dissipated per cycle divided by the product of 4π and strain energy; the stiffness ratio of transformation plateau is defined as the ratio of the stiffness of loading plateau to the initial stiffness

of austenite. It is seen in Figure 3.6 that the proposed constitutive model can fairly accurately reproduce the trend and offer a good estimate of the damping property and stiffness ratio of transformation plateau of superelastic Nitinol wires. Since at certain loading frequencies noticeable difference exists in the hysteresis loops of the first several cycles and the subsequent cycles, these two quantities are calculated from the cycle after the stabilization of the stress-strain curve. For loading frequencies in the range between 0.1 Hz and 1 Hz which is often the frequency range of interest for vibration control application, the error of both the equivalent viscous damping ratio and the stiffness ratio of transformation plateau is observed to be less than 12%.

Figure 3.7 shows the hysteresis of superleastic Nitinol wires corresponding to experimental data and numerical simulation respectively. The data in Figure 3.7 corresponds to at a loading frequency of 0.1 Hz but with different strain amplitude. It is seen that the proposed constitutive model can generate a fairly good estimate of the hysteresis loops for different strain amplitudes. Slight discrepancy is also observed along the unloading path for small amplitude cases, which may result in an overestimate of the energy dissipation capacity in small amplitude vibration. This discrepancy is due to the difference between the real transformation kinetics and that given by Equation (3-22).

3.2.7 Summary

This section presents an improved thermo-mechanical constitutive model which can be used to predict the uniaxial superelastic behavior of SMA wires at varying strain-

rate. The mechanical law governing the stress-strain behavior and the energy balance equation reflecting the rate-dependent thermal effect are derived within a thermodynamics framework. Alternatively, the Voigt model can be used to explain the physical meaning of the energy balance equation. A new form of transformation kinetics is also proposed to describe the evolution of martensite fraction for improved agreement with experimental stress-strain relation of superelastic Nitinol wires. These three principal components – mechanical law, energy balance equation and transformation kinetics comprise the proposed constitutive model for superelastic SMA wires. Expressions for both constant and non-constant elastic modulus are presented in this paper and non-constant elastic modulus has more complex expression for the derivative mechanical law and the energy balance equation. The integration scheme proposed in this paper facilitates the numerical simulation of the proposed constitutive model, especially for dynamic analyses of large scale structural systems with SMA based device.

A series of unaxial tensile tests on 0.58-mm diameter superelastic Nitinol wires were compared with the simulation results by the thermo-mechanical constitutive model. Both the experimental and simulation results indicate that loading rate affects the thermo-mechanical behavior of superelastic Nitinol wires. The proposed constitutive model exhibits a good agreement with the experimental stress-strain relationship at the loading rates considered. It can predict reasonably well the reduction in hysteresis area, rise of the transformation plateau and the increased slope of the loading transformation plateau with increasing loading rates. It can also capture the tendency of temperature change in superelastic Nitinol wires under various loading

rates: under quasi-static loading rate the temperature fluctuation is ignorable, and under medium loading rate the wire cools down in the first a few cycles, while under fast loading rate the average of the wire temperature rises in the first few cycles due to self-heating effect. This temperature change leads to a change in hysteresis with increasing number of cycles, which is consistent with the experimental observations. The equivalent viscous damping ratio and stiffness ratio of transformation plateau were also evaluated in this study for different loading frequencies, for both the experimental data and the simulation data. The proposed constitutive model is able to reflect the trend of these properties with increasing loading rates and a reasonably good agreement between the experimental and simulation data can be achieved.

3.3 MODIFIED WILDE MODEL

3.3.1 Introduction

This section employs a modified version of the constitutive model for SMA initially developed by Grasser and Cozzarelli (1992). The Graesser-Cozzarelli model for SMA is an extension of a rate-independent model for hysteretic behavior proposed by Ozdemir (1976). The Graesser-Cozzarelli model which simulates the one-dimensional stress-strain relationship of superelastic SMA wires is written as (Grasser and Cozzarelli 1992):

$$\dot{\sigma} = E\left[\dot{\varepsilon} - \left|\dot{\varepsilon}\right| \cdot \left(\frac{\sigma - \beta}{Y}\right)^{n}\right] \tag{3-32a}$$

$$\beta = E\alpha\left\{\varepsilon_{in} + f_T \cdot \left|\varepsilon\right|^{c} \cdot \mathrm{erf}(a\varepsilon) \cdot \mathrm{H}(-\varepsilon\dot{\varepsilon})\right\} \tag{3-32b}$$

where σ, ε are the one-dimensional stress and strain, respectively; β is the one-dimensional backstress; E is the initial modulus of elasticity of SMA; Y is the upper (loading) plateau stress (i.e., the 'yielding'-like plateau in the loading stage); $\alpha = E_y/(E-E_y)$ is a constant that controls the slope of the stress-stain curve, where E_y is the slope after yielding; f_T, a, and c are material constants controlling the recovery of the inelastic strain upon unloading; n is a constant controlling the sharpness of transition between different phases; dot implies ordinary time derivative; erf(·) and H(·) are the error function and unit step function (i.e., Heaviside function), respectively. and they are mathematically defined as,

$$\mathrm{H}(x) = \begin{cases} 0 & \text{if} \quad x < 0 \\ +1 & \text{if} \quad x \geq 0 \end{cases} \tag{3-33}$$

$$\mathrm{erf}(x) = \frac{2}{\sqrt{\pi}} \int_0^x e^{-t^2} dt \tag{3-34}$$

Additionally, $\varepsilon_{\mathrm{in}}$ is the inelastic strain, which is expressed as follows,

$$\varepsilon_{in} = \varepsilon - \frac{\sigma}{E} \tag{3-35}$$

The Graesser-Cozzarelli model was extended by Wilde et al. (2000) to include the hardening behavior of SMA material after the transition from austenite to martensite is completed. The constitutive model for SMA developed by Wilde et al. (2000) can be expressed as follows,

$$\begin{aligned} \dot{\sigma} = E \cdot \left[\dot{\varepsilon} - \left|\dot{\varepsilon}\right| \cdot \left(\frac{\sigma - \beta}{Y} \right)^n \right] \cdot u_I(\varepsilon) + E_m \cdot \dot{\varepsilon} \cdot u_{II}(\varepsilon) \\ + (3a_1 \cdot \dot{\varepsilon}\varepsilon^2 + 2a_2 \cdot \mathrm{sgn}(\varepsilon) \cdot \dot{\varepsilon}\varepsilon + a_3 \cdot \dot{\varepsilon}) \cdot u_{III}(\varepsilon) \end{aligned} \tag{3-36a}$$

$$\beta = E_t \alpha \left\{ \varepsilon_{in} + f_T \cdot |\varepsilon|^c \cdot \mathrm{erf}(a\varepsilon) \cdot \mathrm{H}(-\varepsilon\dot{\varepsilon}) \right\} \tag{3-36b}$$

The functions $u_{\mathrm{I}}(\varepsilon)$, $u_{\mathrm{II}}(\varepsilon)$ and $u_{\mathrm{III}}(\varepsilon)$ are expressed respectively as,

$$u_I(\varepsilon) = 1 - u_{II}(\varepsilon) - u_{III}(\varepsilon) \tag{3-37}$$

$$u_{II}(\varepsilon) = \begin{cases} 1 & \text{if } |\varepsilon| \geq \varepsilon_m \\ 0 & \text{otherwise} \end{cases} \tag{3-38}$$

$$u_{III}(\varepsilon) = \begin{cases} 1 & \text{if } \varepsilon \cdot \dot{\varepsilon} > 0 \text{ and } \varepsilon_1 < |\varepsilon| < \varepsilon_m \\ 0 & \text{otherwise} \end{cases} \tag{3-39}$$

In Equation (3-36), E_m is the elastic modulus of martensite; the second term in Equation (3-36) describes the elastic behavior of martensite, which is activated when the strain value is greater than ε_m. Strain ε_m defines the point where the transition of SMA from austenite to martensite is completed. A smooth transition from a curve of slope E_y to a curve of slope E_m is obtained by adding the last term in Equation (3-36*a*), which is evaluated only during loading and for the strain range $\varepsilon_1 < |\varepsilon| < \varepsilon_m$. The constants a_1, a_2 and a_3 in Equation. (3-36*a*) control the curvature of the transition from austenite to martensite. These constants are selected in such a way that the slopes of the function defined by the last term at points ε_1 and ε_m are consistent with those of SMA "plastic" behavior and martensite elastic response. Three terms in Equation (3-36*a*) control the different parts of stress-strain curve respectively, and at anytime only one of them is activated (as shown in Figure 3.8).

3.3.2 Model Description

In this study, the above-described Wilde model for SMA is further modified to enhance the stability of numerical simulation, speed up the computation time and improve the simulation effect. Thus the constitutive model employed in this study for SMA wires is called modified Wilde model. The modified Wilde model which simulates the one-dimensional stress-strain relationship of superelastic SMA is expressed as follows,

$$\dot{\sigma} = E \cdot \left[\dot{\varepsilon} - K \cdot |\dot{\varepsilon}| \cdot \mathrm{sgn}(\sigma - \beta) \cdot \left(\frac{|\sigma - \beta|}{Y}\right)^n \right] \cdot u_I(\varepsilon) + E_m \cdot \dot{\varepsilon} \cdot u_{II}(\varepsilon) + \left(E_y \frac{\varepsilon_m - \varepsilon}{\varepsilon_m - \varepsilon_1} + E_m \frac{\varepsilon - \varepsilon_1}{\varepsilon_m - \varepsilon_1}\right) \cdot \dot{\varepsilon} \cdot u_{III}(\varepsilon) \tag{3-40a}$$

$$\beta = \alpha \cdot E \cdot [\varepsilon_{in} + f_T \cdot \mathrm{H}(-\varepsilon\dot{\varepsilon}) \cdot \mathrm{sgn}(\varepsilon) \cdot g(a \cdot \varepsilon_{in} + \mathrm{sgn}(\varepsilon) \cdot b)] \tag{3-40b}$$

where sgn(·) is the Signum function. Since the slope of each segment and sharpness of the transition to the plateaus are different for the loading and unloading stages, different parameters E and n need to be used for the loading and unloading stages. a and b are material constants controlling the transition from lower plateau to elastic range during the unloading process; function $g(\cdot)$ is defined as

$$g(t) = 1 - e^{-t^2} \tag{3-41}$$

and coefficient K is defined by

$$K = \begin{cases} 1 & \text{if } \varepsilon\dot{\varepsilon} > 0, \text{ loading} \\ \mathrm{H}(\varepsilon_{in}\varepsilon) & \text{if } \varepsilon\dot{\varepsilon} \le 0, \text{ unloading} \end{cases} \tag{3-42}$$

and the function $u_{III}(\varepsilon)$ are re-defined as,

$$u_{II}(\varepsilon)=\begin{cases}1 & \text{if } \varepsilon\dot{\varepsilon}>0 \text{ and } |\varepsilon|\geq\varepsilon_m \\ 0 & \text{otherwise}\end{cases} \tag{3-43}$$

The segments on stress-strain curve corresponding to three terms in Equation (3-40*a*) are shown in Figure 3.9-(a), which are different from the original Wilde model.

It is assumed that SMA wires can only undertake tension force, i.e., $\sigma = 0$ if $\varepsilon < 0$. Equation. (3-40) can be rewritten as follows when $\varepsilon > 0$,

if $\dot{\varepsilon} > 0$, loading

$$\begin{cases}\dot{\sigma}=E\cdot\left[\dot{\varepsilon}-\dot{\varepsilon}\cdot(\dfrac{\sigma-\beta}{Y})^n\right]\cdot u_I(\varepsilon)+E_m\cdot\dot{\varepsilon}\cdot u_{II}(\varepsilon)+(E_y\dfrac{\varepsilon_m-\varepsilon}{\varepsilon_m-\varepsilon_1}+E_m\dfrac{\varepsilon-\varepsilon_1}{\varepsilon_m-\varepsilon_1})\cdot\dot{\varepsilon}\cdot u_{III}(\varepsilon) \\ \beta=\alpha\cdot E\cdot\varepsilon_{in}\end{cases} \tag{3-44a}$$

if $\dot{\varepsilon} < 0$, unloading

$$\begin{cases}\dot{\sigma}=E\cdot\left[\dot{\varepsilon}+\dot{\varepsilon}\cdot\mathrm{H}(\varepsilon_{in})\cdot\mathrm{sgn}(\sigma-\beta)(\dfrac{|\sigma-\beta|}{Y})^n\right] \\ \beta=\alpha\cdot E\cdot[\varepsilon_{in}+f_T\cdot g(a\varepsilon_{in}+b)]\end{cases} \tag{3-44b}$$

where α, E and n can take different values during the loading and unloading stages if different stiffness or sharpness of transition are demanded. The effects of loading rate and temperature were not considered in the Wilde model. Similarly, the modified Wilde model presented here for superelastic SMA does not include the loading rate and temperature effects as well, and thus it is a rate-independent phenomenological model.

Figure 3.9 shows the stress-strain curves of superelastic Nitinol wires obtained from a simulation of the modified Wilde model and test data under two different

frequencies—0.001 Hz (quasi-static test) and 2 Hz. The superelastic Nitinol wires (Type A), have a diameter of 0.58 mm (0.025 in). The details of test program and corresponding results are described in the Section 2.2.5. The corresponding parameter values of the modified Wilde model are listed in Table 3.2. It can be seen that the modified Wilde model well agrees with two experimentally measured hysteretic loops respectively. Compared with the original Wilde model, the modified Wilde model leads to smoother transition of stress-strain curve which is closer to experimental results of superelastic Nitinol wires. However, it should be noted that the modified Wilde model, like the original Wilde model, is still a rate-independent phenomenological model, and two different sets of parameters have to be used for two different frequencies respectively (as shown in Table 3.2). Thus it is unable to simultaneously capture hysteretic behavior under various loading rates. The effect of using such a rate-independent constitutive model in seismic response analyses will be further discussed in Section 3.5.

3.4 FLAG-SHAPED MODEL

The piecewise-linear flag-shaped hysteretic model has been widely used in the study of various self-centering systems, such as rocking walls, post-tensioned concrete or steel frames, SMA devices, and etc, for the sake of simplicity (e.g. Christopoulos et al 2002; Seo and Sause 2005; Mao and Li 2005; Andrawes and DesRoches 2005). A typical flag-shaped hysteretic model to describe the stress-strain relationship of superelastic Nitinol wires can be fully defined with five parameters - elastic modulus

of austenite E_a, elastic modulus of martensite E_m, 'yield' stress σ_y, post-'yield' stiffness coefficient α and energy dissipation coefficient β, as shown in Figure 3.11.

Figure 3.10 shows the stress-strain curves of superelastic Nitinol wires obtained from a simulation of the flag-shaped model and test data under two different frequencies—0.001 Hz (quasi-static test) and 2 Hz. The details of test program and corresponding results are described in the Section 2.2.5. Although the flag-shaped model can predict reasonably well the key features of superelastic Nitinol wires such as initial stiffness, post-'yield' stiffness, upper and lower plateau stress, apparent discrepancy can be observed between the test data and prediction from the flag-shaped model along the unloading path, which may lead to the overestimation of energy dissipation. Similar to the modified Wilde model, the flag-shaped model is rate-independent and it is unable to simultaneously capture hysteretic behavior under two different loading rates.

3.5 COMPARATIVE STUDY OF STRAIN RATE EFFECT

3.5.1 Introduction

The rate-dependent thermo-mechanical constitutive model described earlier can fairly well reproduce the hysteretic behavior of SMA materials under various loading rates. However, it is derived in a thermo-dynamics framework and the associated complexity often deters the use of this kind of model by engineers in seismic applications. Furthermore, the rate-dependent constitutive models for SMA cannot be directly used in nonlinear static analysis procedures such as push-over analyses, even if this model

can yield accurate and reliable results in nonlinear dynamic analyses. On the contrary, rate-independent phenomenological models for SMA cannot explicitly considered the temperature and loading rate effects, but they are very appealing to seismic applications because of their simpler mathematical expression and computationally less demanding than the thermo-mechanical constitutive models.

In light of this observation, this section presents the results of a feasibility study on using rate-independent constitutive model for superelastic SMA in seismic response analyses of structures through a comparative study of three nonlinear constitutive models for superelastic SMA wires. Three constitutive models for superelastic SMA wires described previously in this chapter are considered in the comparative study: (i) the rate-dependent thermo-mechanical model (TM model); (ii) the modified Wilde model (MW model); (iii) a piecewise linear flag-shaped model (FS model). For the rate-dependent constitutive model (i.e. MW model and FS model), the parameters of the model are tuned with the dynamic test results with the loading frequency of 2 Hz (as shown in Figure 3.9-(b) and Figure 3.10-(b)).

Parametric study of single-degree-of-freedom (SDOF) systems with superelastic SMA resistant element was carried out with varying initial elastic periods and strength reduction factors. Results of nonlinear dynamic analyses of a 6-story building with SMA-based damping devices are also presented here. The results of this study show that with properly tuned parameters, rate-independent constitutive models can fairly well predict the seismic response behavior of structures equipped with SMA-based seismic response modification devices.

3.5.2 Parametric Study: SDOF System

In order to compare the effect of different constitutive models on structural seismic response behavior, a parametric study of the nonlinear dynamic response of SDOF systems with superelastic SMA element was carried out in this study. The resisting force of the SDOF system is assumed to be provided by a superelastic Nitinol element.

3.5.2.1 *Equation of motion*

The governing equation of motion of a nonlinear SDOF system under earthquake loading is

$$m \cdot \ddot{x} + c \cdot \dot{x} + F(x, \dot{x}) = -m \cdot \ddot{x}_g \tag{3-45}$$

where m is the mass; c is the viscous damping coefficient; x, $\dot{x}$ and $\ddot{x}$ are the relative displacement, velocity and acceleration of the system; and $\ddot{x}_g$ is the ground acceleration; $F(x, \dot{x})$ is the nonlinear resisting force of the superelastic Nitinol element which is modeled using one of the afore-mentioned constitutive models. As noted before, the parameters of rate-independent models are corresponding to the dynamic test of superelastic Nitinol wires with the loading frequency of 2 Hz. The viscous damping ratio of the system is assumed to be 5% in this study.

With the constitutive model's parameters derived from experimental data, the values of the energy dissipation coefficient and the post-'yield' stiffness coefficient for the superelastic SMA element are thus specified. Two essential parameters of this SDOF system are its initial elastic period T_0 and 'yield' strength F_y, expressed as

$$T_0 = 2\pi \cdot \sqrt{m / k_0}$$

$$F_y = \frac{F_e}{R}$$

where k_0 is the initial stiffness of the system, F_e is the elastic strength demand. Here the yield strength F_y is found by dividing F_e with the strength reduction factor R. With known stress-strain relationship for the superelastic SMA element, the initial elastic stiffness and yield strength can be adjusted by altering its cross section area and length. The range of initial elastic period considered in this study is 0.2 sec $\leq T_0 \leq$ 2.5 sec which is typical for one- to 20-story steel braced frames. The values of the strength reduction factor R considered in this study are 2, 4 and 6 respectively.

The nonlinear time history analyses employ the suite of design basis earthquake (DBE) ground motions (i.e., with 10% probability of exceedance in 50 years) which was developed by Somerville et al. (1997). The details of ground motions are described in Appendix A. This earthquake suite contains 20 records designated as LA01 - LA20, and it is corresponding to site class D (firm soil) at downtown, Los Angeles.

3.5.2.2 *System response indices*

In this comparative study of the three afore-mentioned constitutive models for superelastic Nitinol wires, the following response indices of SDOF system were used in the evaluation:

Peak displacement ductility: $\mu = x_{\max} / x_y$, where x_y is the 'yield' displacement which corresponds to the 'yield' strain ε_y = 0.9% for the superelastic Nitinol wires, as

shown in Figure 3.10-(b). It should be noted that the 'yield'-like plateau is not due to plastic deformation but phase transformation, thus no damage accumulation occurs in superelastic Nitinol element as long as its strain does not exceed 8%. Beyond the 8% strain, residual strain may occur after unloading due to plastic deformation and thus 8% is assumed to be the maximum recoverable strain level for the superelastic Nitinol wires used in this study. If the damage-free and self-centering features of superelastic SMA element are desired under earthquake loading, the ductility ratio μ has to be limited to below 9.

Peak acceleration: $a_{\max}$, acceleration response is an important indicator of the base shear caused by earthquake loading as well as the potential damage of acceleration-sensitive elements.

Normalized dissipated energy: $e_{dis} = \frac{E_{dis}}{\frac{1}{2} k_0 x_y^2}$, where E_{dis} is the total hysteretic energy dissipated by the superelastic SMA element. This index provides a measure of the energy dissipating capacity predicted by different constitutive models.

3.5.2.3 *Results and discussion*

Figure 3.12 shows the statistical results of the above three key response indices for SDOF system with the three constitutive models respectively under twenty DBE earthquakes. Nine curves are drawn in each sub-figure. The middle set of curves in each sub-figure represents the ensemble average for the corresponding response index, while the upper and lower sets of curves represent one standard deviation from the ensemble average respectively. Here the ensemble average and standard deviation are

calculated based on the system response under twenty earthquakes from the DBE suite. The three constitutive models give similar results in terms of the trend of the response indices with varying initial period values of the SDOF system. The maximum difference between the ensemble average curves of the peak displacement ductility and peak acceleration for the three constitutive models is observed to be less than 8%. Similarly, only very little difference is observed in the curves corresponding to a standard deviation away from the ensemble average curve. In terms of energy dissipation, however, notable difference exists between the response index curves corresponding to the three constitutive models. Compared with the TM model, the FS model tends to overestimate the energy dissipation capacity for all three values of the strength reduction factor, and the error of the ensemble average could reach up to 35% as for the case of R = 2. In comparison with TM model, the MW model offers a fairly good estimation of the energy dissipation capacity for the cases of R = 2 or 4, but significantly overestimates the energy dissipation capacity for the case of R = 6, especially for short periods in which the error between the ensemble average curves could reach up to 60%. The difference between the curves corresponding to a standard deviation away from the ensemble average is even larger. For strength reduction factor R=6, peak displacement ductility ratios tend to exceed the limit of 9 for systems with short periods for which none of the three constitutive models can accurately predict the energy dissipation capacity of the superelastic SMA element.

Figure 3.13 presents the correlation between the response indices corresponding to the three constitutive models when the strength reduction factor is equal to 4. Each data point in the sub-figure of Figure 3.13 represents the respective response index

result corresponding to a different earthquake record and initial period of the SDOF system. It should be noted that in a few cases the values of the displacement ductility exceeded 9，which is the maximum allowable ductility ratio corresponding to the maximum recoverable strain of the superelastic Nitinol element. These cases with $\mu > 9$ are excluded from Figure 3.13 since none of the three constitutive models can reproduce the complex hardening behavior of superelastic Nitinol wires beyond 8% strain. The dashed lines in these figures delineate the boundary corresponding to a 10% difference, i.e. any data point outside the boundaries implies the difference between the response indices from the corresponding two constitutive models are greater than 10%. It is seen from Figure 3.13 that the differences in the peak displacement ductility and peak acceleration between the concerned constitutive models are relatively small, and in most cases the difference is less than 10%. However, slightly larger difference can be observed for the energy dissipation between the three constitutive models. Compared with the TM model, the FS model tends to overestimate the energy dissipation in most cases, while the MW model tends to overestimate the energy dissipation only in the cases with large energy dissipation which usually corresponds to large peak ductility ratios.

Figure 3.14 shows the typical stress-strain curve of superelastic SMA element from the TM model for the SDOF systems subjected to earthquake record LA09. The hysteretic loops in Figure 3.14-(a) and (b) were obtained from SDOF systems with an initial period of 0.3 sec and 3.0 sec respectively. It is seen that the TM model gives slightly different results in the unloading segment of the stress-strain curve as well as energy dissipation capacity of the superelastic Nitinol element. However, unlike in

Figure 3.4, no significant shift of the hysteretic loops is observed in this figure for both cases with different initial periods. As discussed earlier, the shift of the hysteretic loops or the change in zero-strain temperature is a gradual progress, and larger amplitude vibration always leads to larger temperature variation including change of zero-strain temperature; however, structural response of larger amplitude under strong earthquakes usually lasts for a limited time which is insufficient to induce the considerable change of zero-strain temperature as well as shift of hysteretic loops. The change in zero-strain temperature predicted by the TM model for both initial periods is less than 4ºC, which results in negligible shift of hysteretic loops.

It is observed that only minor difference exists in the first cycle hysteresis between cases with different loading rates, and no significant shift of hysteretic loops occur under earthquake loading. Therefore, replacing rate-dependent constitutive model with rate-independent models such as the MW model or FS model appears to be acceptable for seismic analyses of structures with superelastic SMA element. The results given in Figure 3.12 and Figure 3.13 also suggest that the rate-dependent thermal effect of superelastic SMA elements has little effect on its dynamic behavior under earthquake loading and all three aforementioned constitutive models for superelastic Nitinol wires give close estimations of the peak displacement ductility and peak acceleration.

3.5.3 Nonlinear Dynamic Analyses of MDOF System

This section presents nonlinear seismic analyses of a 6-story steel braced frame equipped with SMA based bracing elements. The structural response behavior

simulated using the aforementioned three constitutive models for superelastic Nitinol wires is discussed here.

3.5.3.1 *Prototype building*

In this study, the 6-story frame structure with a special SMA based bracing element termed self-centering friction damping brace (SFDB) is selected as the prototype structures for nonlinear time history analyses. The details about this 6-story building are described in Appendix B. The mechanical configuration of SFDB will be discussed in next chapter. Like BRB, typically SFDB would also be part of the bracing system of concentrically braced frame. Thus the SFDBs would be installed at the same locations as shown in Figure B.2. The 'yield' capacities of SFDBs are equal to the average of tensile and compressive strength of corresponding BRBs, i.e. 105% of the yield strength shown in Table B.1. The lengths of superelastic Nitinol wire strands in the SFDBs is 0.85 m for the 1st story and 0.7 m for all other stories, which translates into 8% strain in the superelastic Nitinol wires at a 2% story drift ratio. As mentioned earlier, in this study, 8% strain is taken as the maximum recoverable strain (without residual deformation) for superelastic Nitinol wires, that is, if the strain of Nitinol wires was lower than 8% during an earthquake, residual strain of the Nitinol wires would be negligible and thus no repair or replacement of SFDBs would be necessary after the earthquake if other parts are designed to remain elastic during design basis earthquakes. The friction force between the two sliding parts in the SFDBs is set to be 28% of brace 'yield' strength.

3.5.3.2 *Nonlinear time history analyses*

Nonlinear time history analyses of this 6-story prototype building with SFDBs was carried out using the computer program DRAIN-2DX (Prakash et al. 1993), and the 20 records from the DBE earthquake suite were also employed. In the nonlinear time history analyses, only one bay of the braced frame was modeled and analyzed. Thus the seismic mass of each floor was calculated by dividing the total seismic floor masses with the number of braced bays in each principal direction (i.e., 1/6 of the total dead load for the 6-story building). The detailed analytical model is described in Appendix B.

In order to simulate the hysteretic behaviors of SFDBs predicted using the aforementioned three constitutive models, three new elements which correspond to the TM model, MW model and FS model respectively were developed in DRAIN-2DX for this study. In addition to the constitutive relationships described in this chapter for superelastic Nitinol wires, the friction effect in SFDBs was also included in these three elements.

3.5.3.3 *Results and discussion*

Figure 3.15 to Figure 3.17 show the results of nonlinear seismic analyses of the 6-story SFDB frames using the three aforementioned constitutive models for superelastic Nitinol wires. Figure 3.15 shows the maximum inter-story drift ratios of the 6-story SFDB frames subjected to the earthquake ground motions in the aforementioned DBE suite. The mean values of the maximum inter-story drift ratios

for the case of the TM, MW and FS models are 0.63%, 0.63% and 0.59% respectively. Using the results of the TM model as datum, the difference in the maximum inter-story drift ratios between the MW and FS models are less than 15% under all twenty earthquake records, and is less than 6% under 15 out of the 20 earthquake records. For all three constitutive models, the residual inter-story drifts of the 6-story SFDB frames were negligible under all twenty earthquake records due to the self-centering behavior of SFDB. It is noted that with the specified Nitinol wire length, the maximum recoverable strain - 8% for the Nitinol wires corresponds to 2% story drift ratio for the prototype building. Therefore, whenever transient story drift ratio exceeds 2%, the friction surface 2 of SFDBs begins to slip and residual deformation of SFDBs would occur. Thus the SFDBs would have to be repaired and replaced after earthquakes. However, since the peak inter-story drift ratios of the 6-story SFDB frames are always less than 2% under the twenty earthquake ground motions, the SFDBs need not be repaired and the three constitutive models are considered valid for this study.

To better understand the effects of the three constitutive models on the seismic response behavior of the SFDB frame, Figure 3.16 shows typical time histories of its roof displacement and acceleration responses under the LA18 earthquake record. This LA18 record was derived from the ground motion recorded at the Sylmar station during the 1994 Northridge earthquake (Somerville et al 1997). It is seen that three constitutive models yield very similar seismic responses in the time history curves as well as peak values of the roof displacement and absolute acceleration. It is noted again that two of these three constitutive models considered in this study are rate-independent models.

Figure 3.17 shows the statistical results of the nonlinear seismic response of the 6-story SFDB frame under the DBE suite using the TM model, MW model or FS model. Figure 3.17-(a), (b) and (c) show the distribution of the ensemble average of the peak displacements, peak acceleration and peak story drift ratio along the height of the 6-story SFDB frames, respectively. The ensemble average was calculated based on the twenty earthquake ground motions in the DBE suite. It is clearly seen that all three constitutive models give similar distribution patterns for the structural seismic response along the height of the building, and the structural response ensemble average of these three models are very close to each other. Using the results of the TM model as a datum, the error of the seismic response predicted by the MW model is less than 3.6% in peak displacements and peak story drift ratios, and less than 8.5% in peak floor accelerations, while the error of the FS model is less than 4.5% for the peak floor displacements and accelerations, and less than 7.8% for the peak story drift ratios.

3.5.4 Summary

Most SMA materials exhibit strain rate dependent mechanical behavior, and implementing strain rate-dependent constitutive model in structural analysis software is rather complicated and computationally demanding. This study looks into the feasibility of replacing rate-dependent models with rate-independent constitutive models for superelastic SMA elements in seismic time history analyses of structures.

Three uniaxial constitutive models for superelastic SMA are considered in this study: (i) modified rate-dependent thermo-mechanical model; (ii) the modified Wilde

model; and (iii) the piecewise-linear flag-shaped model. Although the latter two are rate-independent phenomenological models, their parameters can be more conveniently tuned based on experimental data from a series of unaxial dynamic test on superelastic Nitinol wires. These three constitutive models give different features in the stress-strain curves of superelastic Nitinol wires, such as the transition smoothness, which might yield different estimation of Nitinol's energy dissipation capacity.

A parametric study based on time history analyses of SDOF systems with different initial periods and strength reduction factors was carried out to study the effect of constitutive models on system response behavior. The parameters of the two rate-independent constitutive models were calibrated using experimental data with a loading frequency of 2 Hz. Twenty design basis earthquakes for Los Angeles region were used in this study to get statistics on performance difference. It is found from the statistical results that the two rate-independent constitutive models give peak displacement ductility ratios and accelerations very close to the rate-dependent thermo-mechanical model, while noticeable difference in energy dissipation can be observed between the three constitutive models. Additionally, the seismic behavior of a 6-story prototype building equipped with special SMA-based damping devices term self-centering friction damping brace (SFDB) was also analyzed using the three constitutive models. Slight difference was observed in the seismic responses of the prototype building as predicted by the three constitutive models.

In view of the similar seismic responses predicted by the three constitutive models for superelastic SMA element, it seems acceptable to use rate-independent constitutive models for superelastic SMA in seismic analyses of structures, as along as the

parameters of this rate-independent model are tuned to dynamic test data. Substantial difference of hysteresis shapes due to temperature variation under earthquakes was not observed in most cases of seismic response analyses. However, the use of more sophisticated thermo-mechanical constitutive models for SMA is still required in certain situations such as where significant change in environmental temperature is expected.

3.6 CONCLUSIONS

Two improved nonlinear constitutive models for SMA wires are proposed in this chapter. One is rate-dependent thermo-mechanical constitutive model which is composed of three principal components—mechanical law, energy balance equation and transformation kinetics. The other is a rate-independent phenomenological model, termed as the modified Wilde model, which is an extension of the model developed by Grasser and Cozzarelli (1992). Then a comparative study of these two constitutive models, along with piecewise-linear flag-shaped model, was carried out in order to investigate the feasibility of using rate-independent constitutive models for superelastic SMA elements in seismic time history analyses of structures. The nonlinear time history analysis results of both SDOF systems and one 6-story prototype building are presented. The study of nonlinear constitutive models for SMA elements has led to the following conclusions:

- In the proposed thermo-mechanical model for superelastic SMA wire, non-constant elastic modulus has more complex expression for the derivative

mechanical law and the energy balance equation than constant elastic modulus. The integration scheme proposed in this study can facilitate the numerical simulation of the proposed thermo-mechanical model. Alternatively, the Voigt model can be used to explain the physical meaning of the energy balance equation.

- The proposed thermo-mechanical model exhibits a good agreement with the experimental stress-strain relationship at the various loading rates. It can predict reasonably well the loading rate-induced thermo-mechanical effect on the superelastic behavior of Nitinol wires, such as the reduction in hysteresis area, rise of the transformation plateau and the increased slope of the loading transformation plateau with increasing loading rates. It can also capture temperature variation in superelastic Nitinol wires under various loading rates. It is able to reasonably well reflect the trend of change of equivalent viscous damping ratio and stiffness ratio of transformation plateau with increasing loading rates
- The modified Wilde model is capable of simulating well the experimental hysteretic behavior of superelastic Nitinol wires at one single loading rate. However, as a rate-independent model, it cannot accurately simulate the hysteresis of Nitinol wire under different loading rates.
- The comparative study indicates that two rate-independent constitutive models give the seismic response of SDOF systems and prototype buildings very close to that from the rate-dependent thermo-mechanical model. Only slight difference was observed in the seismic response such as displacement and acceleration,

while noticeable difference in energy dissipation can be observed between the three constitutive models. Thus it is acceptable to use rate-independent constitutive models for superelastic SMA in seismic analyses of structures if the statistical results of displacement and acceleration are of concern.

- Considering the mathematical complexity, computational demanding and inconvenience in nonlinear static analyses of the rate-dependent constitutive models, the rate-independent constitutive models for superelastic SMA materials are very appealing to the engineer community for seismic applications of SMA-based devices.
- The use of more sophisticated thermo-mechanical constitutive models for SMA is still required in certain situations such as where significant change in environmental temperature is expected.

Table 3.1 Parameters of thermo-mechanical model for superelastic Nitinol wires

Parameter	Units	Value
M_s	°C	-53
M_f	°C	-86
A_s	°C	-29
A_f	°C	-5
E_A	GPa	40
E_M	GPa	22
ε_l	--	0.035
c_A	MPa/K	5.5
c_M	MPa/K	4.0
C_p	J/(kg·K)	600
L	J/kg	10,000
k	W/K	0.042

Table 3.2 Parameters of the modified Wilde model for superelastic Nitinol wires

		Value	
Parameter	Units	0.001 Hz	2 Hz
E	MPa	40,000	40,000
E_m	MPa	21,000	21,000
ε_m	--	0.065	0.063
ε_1	--	0.043	0.041
Y	MPa	360	340
α	--	0.02	0.1
f_T	--	0.65	0.128
a	--	150	150
c	--	0.75	0.75
n_1 (loading)	--	3	3
n_2 (unloading)	--	0.9	1

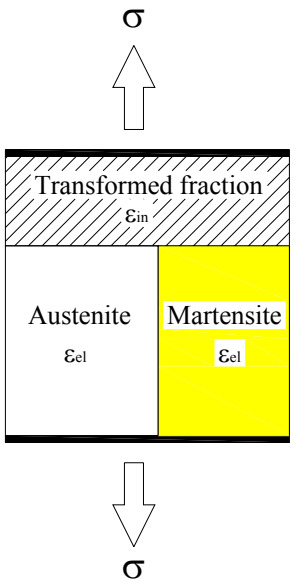

Figure 3.1 Viogt model for superelastic SMA with constant elastic modulus

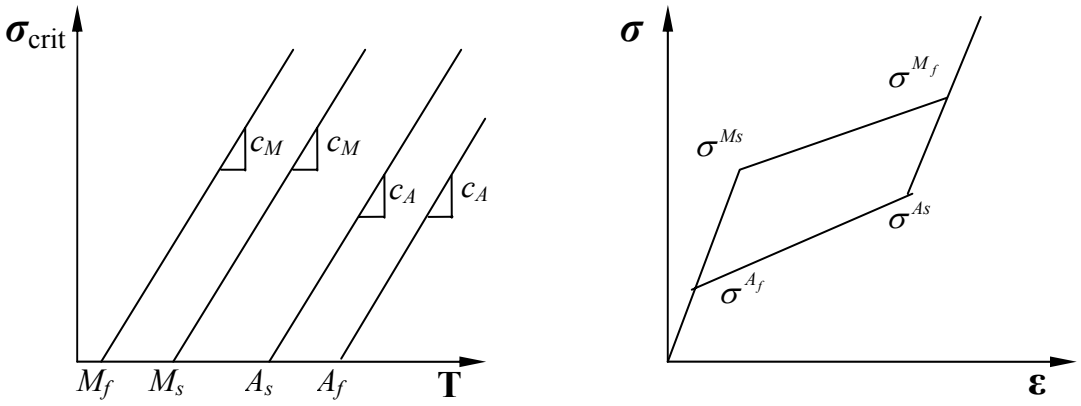

(a) Critical stress-temperature diagram (b) Typical stress-strain curve

Figure 3.2 The relationship between critical stress and temperature for superelastic SMA

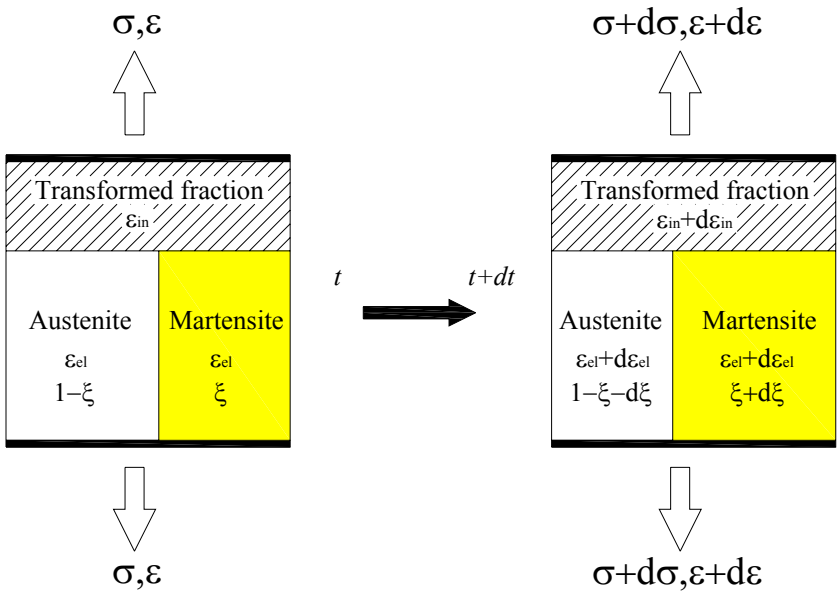

Figure 3.3 Viogt model for superelastic SMA with non-constant elastic modulus

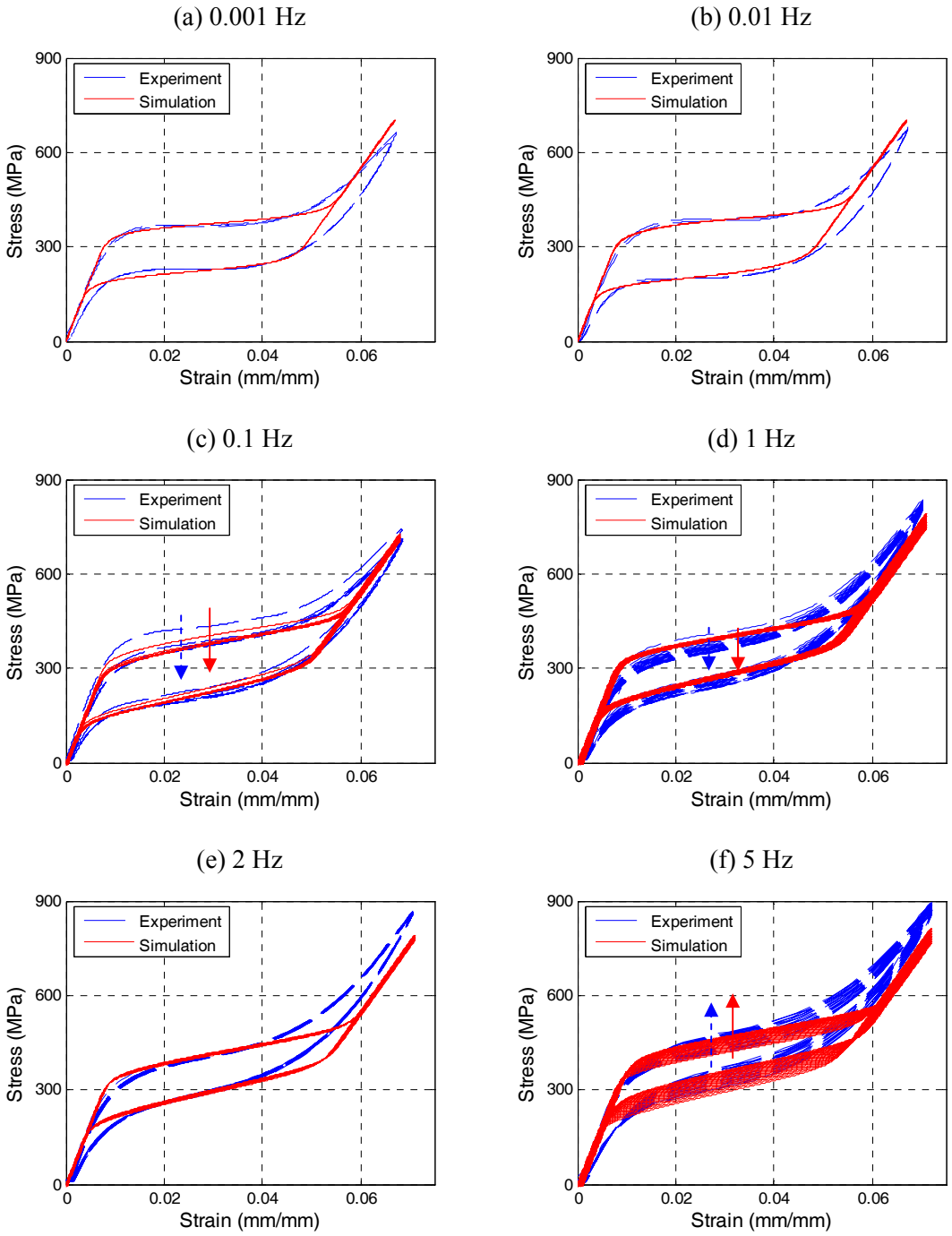

Figure 3.4 Stress-strain curve of superelastic Nitinol wire at various loading rates

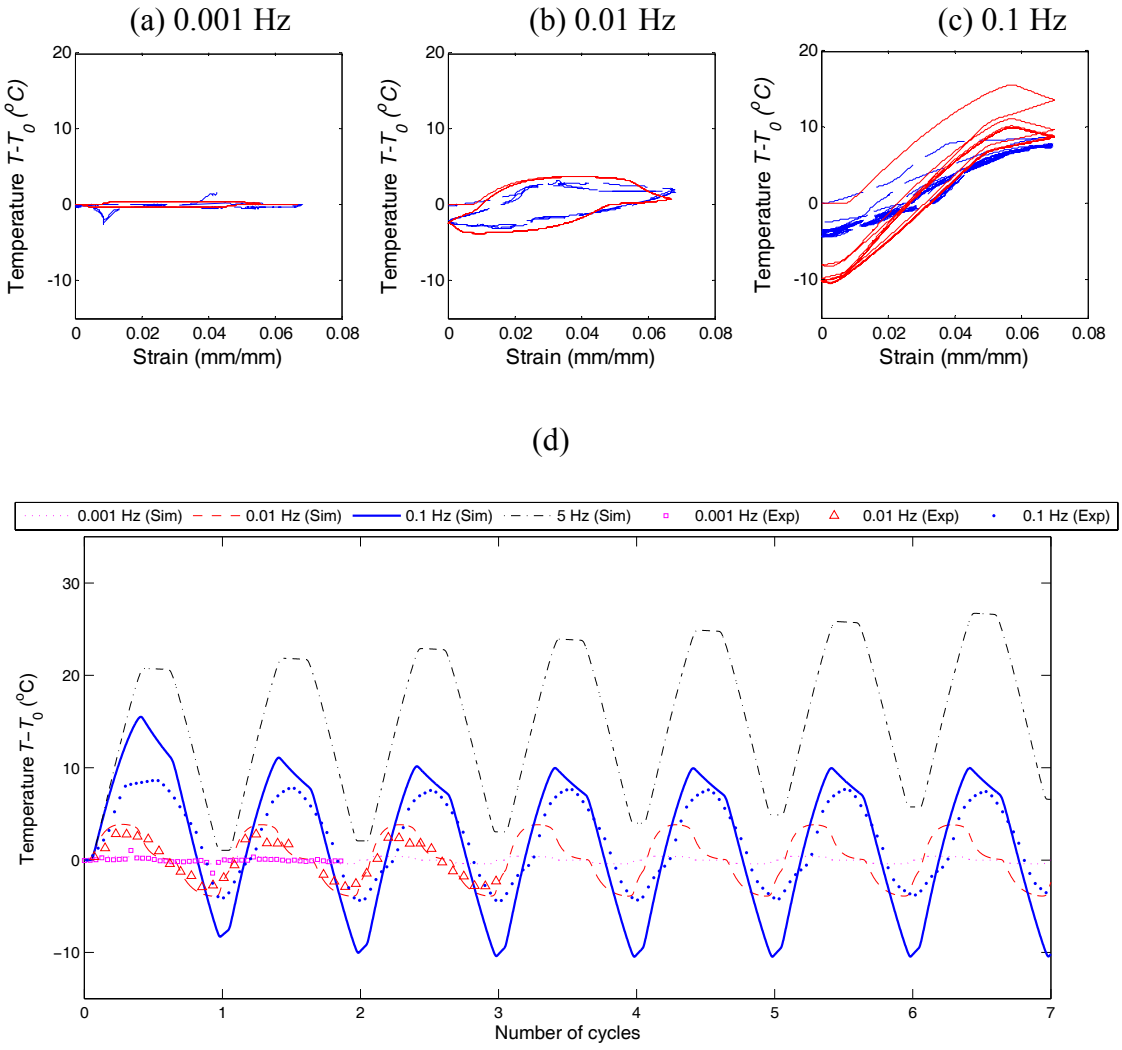

Figure 3.5 Experimental and simulated temperature variation of Nitinol wire specimen

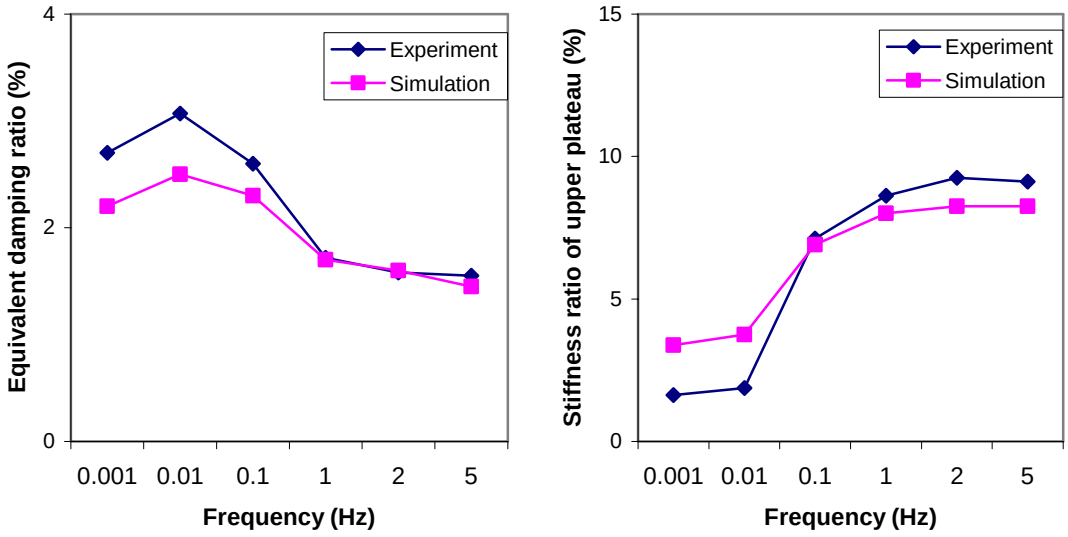

(a) (b)

Figure 3.6 Damping capacity and stiffness ratio of upper transformation plateau of superelastic Nitinol wires from experiment and simulation data

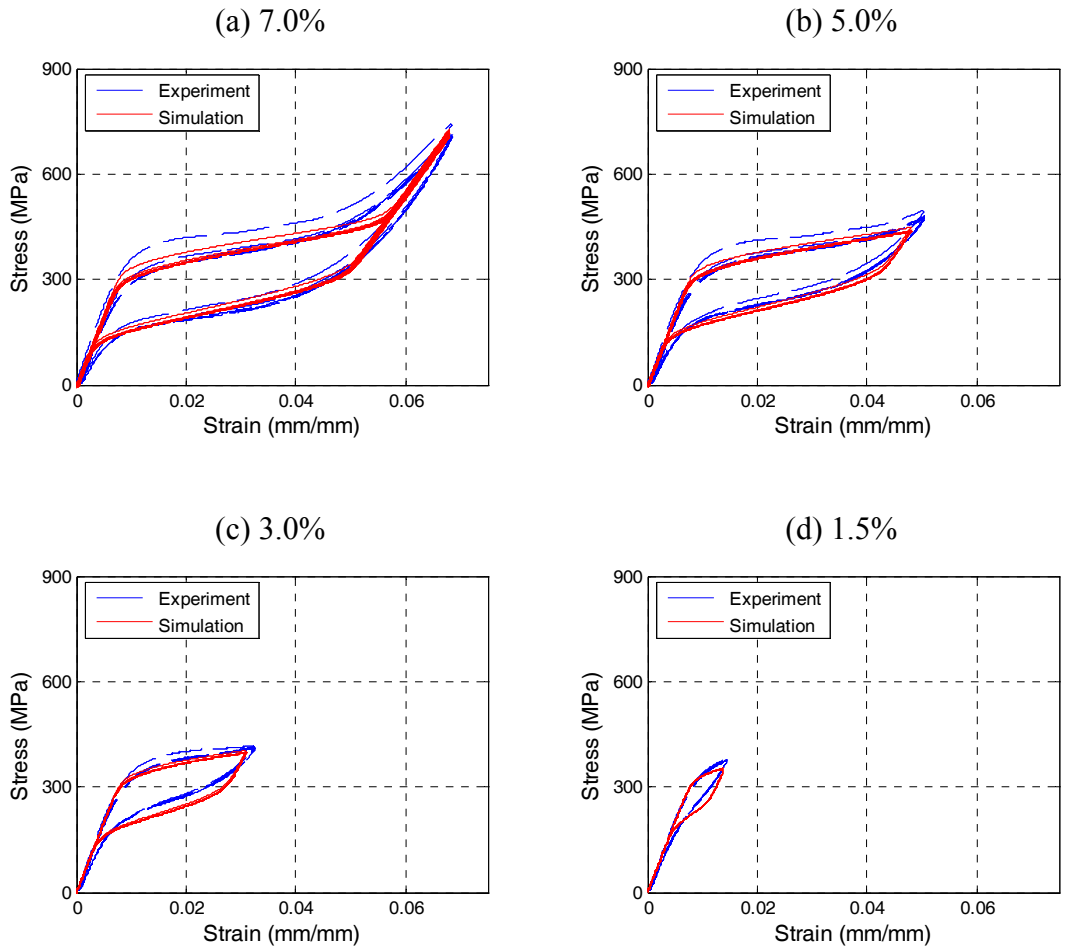

Figure 3.7 Stress-strain curve of superelastic Nitinol wires with various strain amplitudes (loading frequency = 0.1 Hz for all cases)

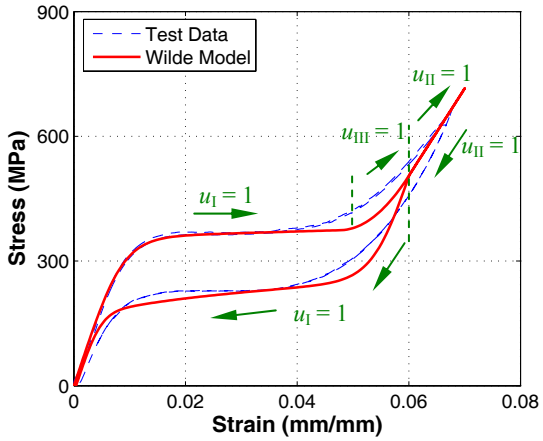

Figure 3.8 Stress-strain curve of superelastic Nitinol wires from test data (0.001 Hz) and the Wilde model

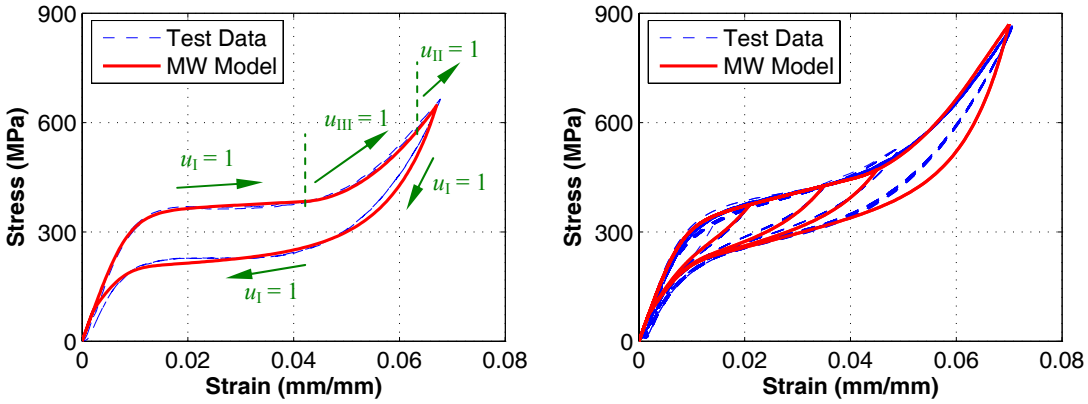

(a) 0.001 Hz (b) 2 Hz

Figure 3.9 Stress-strain curve of superelastic Nitinol wires from test data and the Modified Wilde model

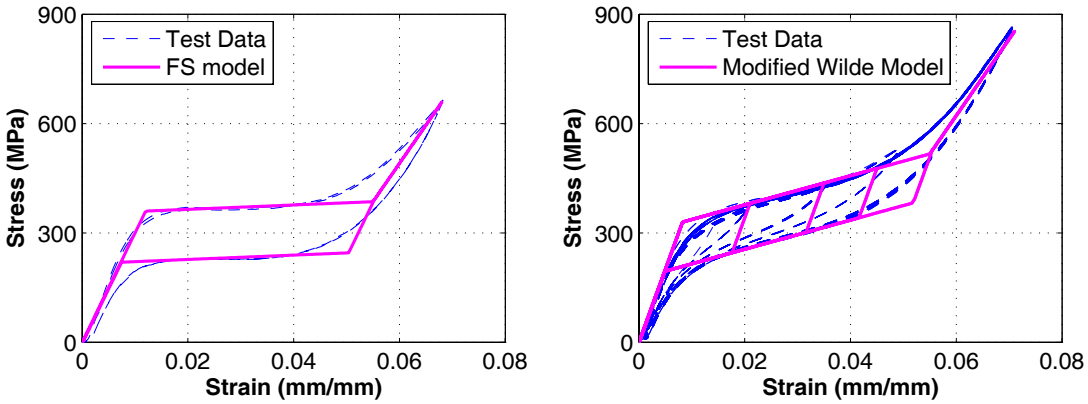

(a) 0.001 Hz (b) 2 Hz

Figure 3.10 Stress-strain curve of superelastic Nitinol wires from quasi-static test data and the multi-linear flag-shaped model

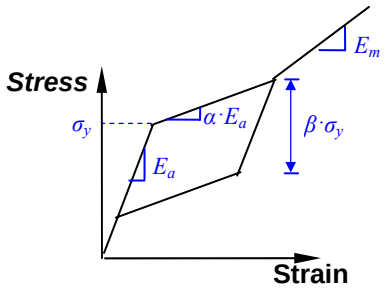

Figure 3.11 Typical flag-shaped hysteretic loop for superelastic Nitinol wires

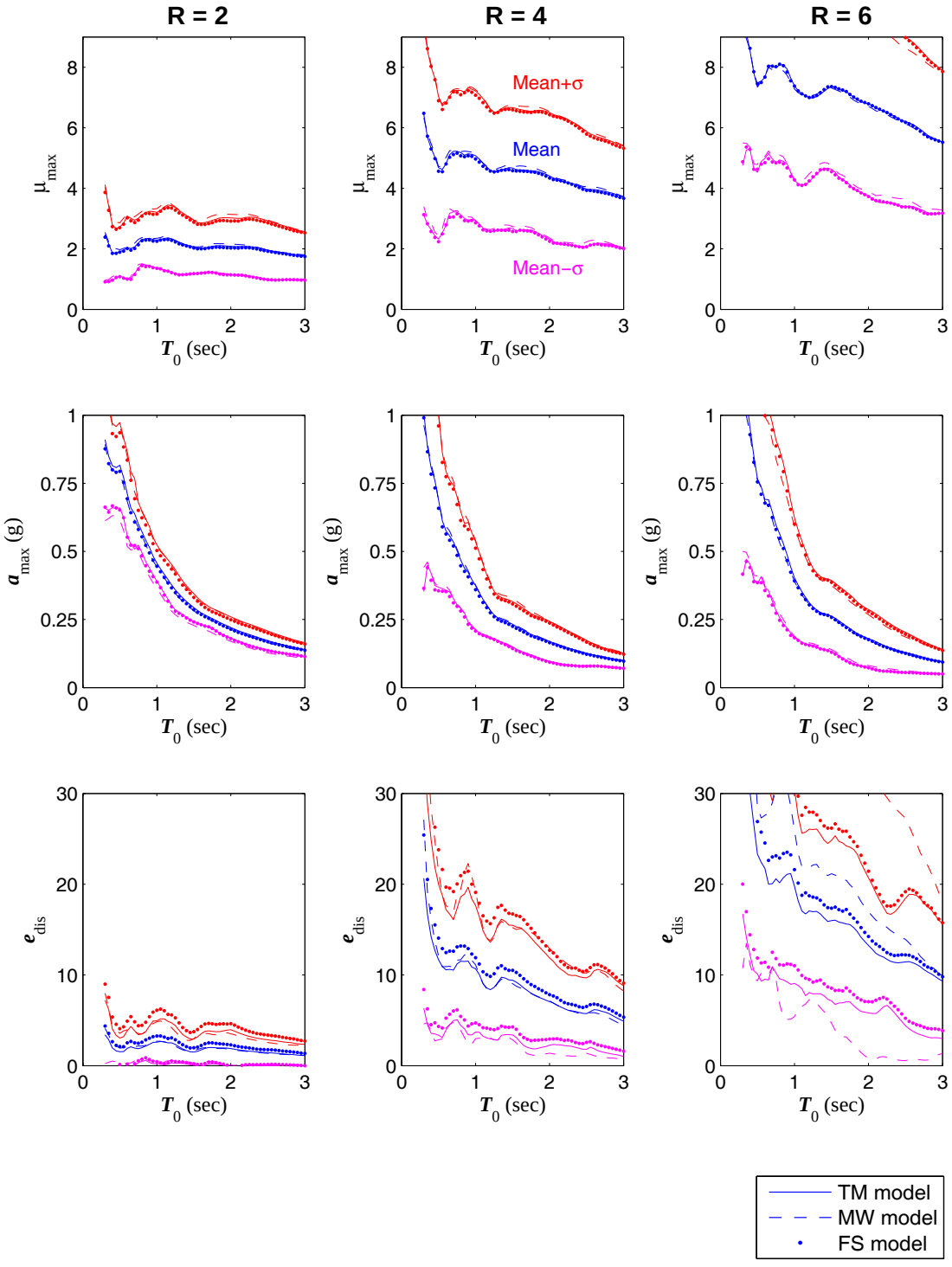

Figure 3.12 Statistical results of the response indices for SDOF system

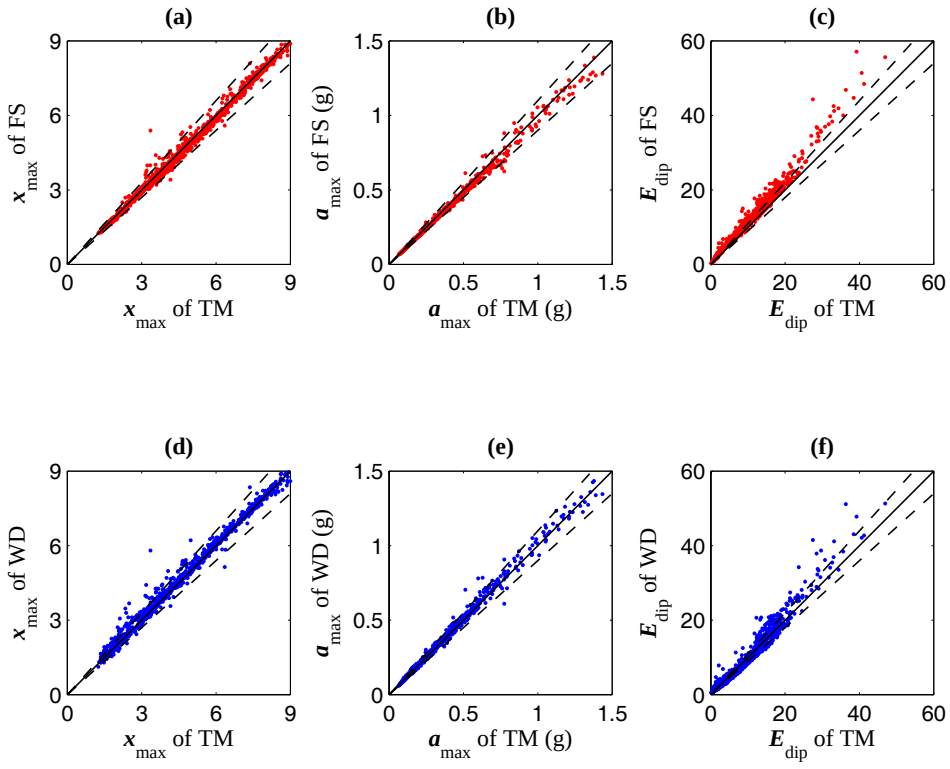

Figure 3.13 Comparison of response indices for R=4: (a), (b) and (c) - FS model vs. TM model; (d), (e) and (f) - WD model vs. TM model

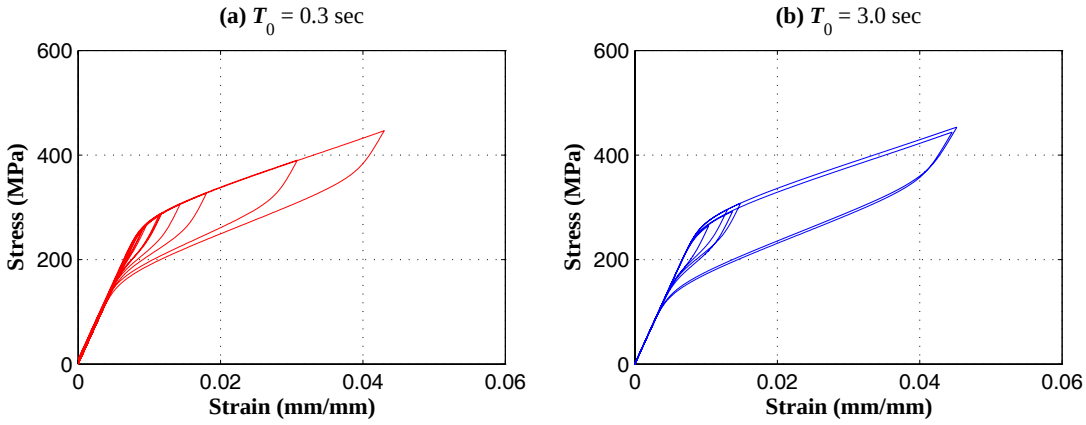

Figure 3.14 Typical stress-strain relationship of superelastic Nitinol elements under earthquake record LA09

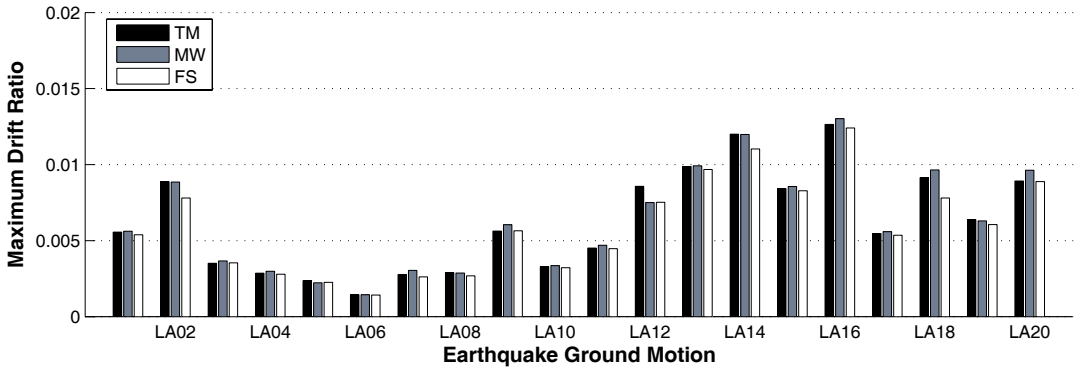

Figure 3.15 Maximum inter-story drift ratio for the 6-story SFDB frame

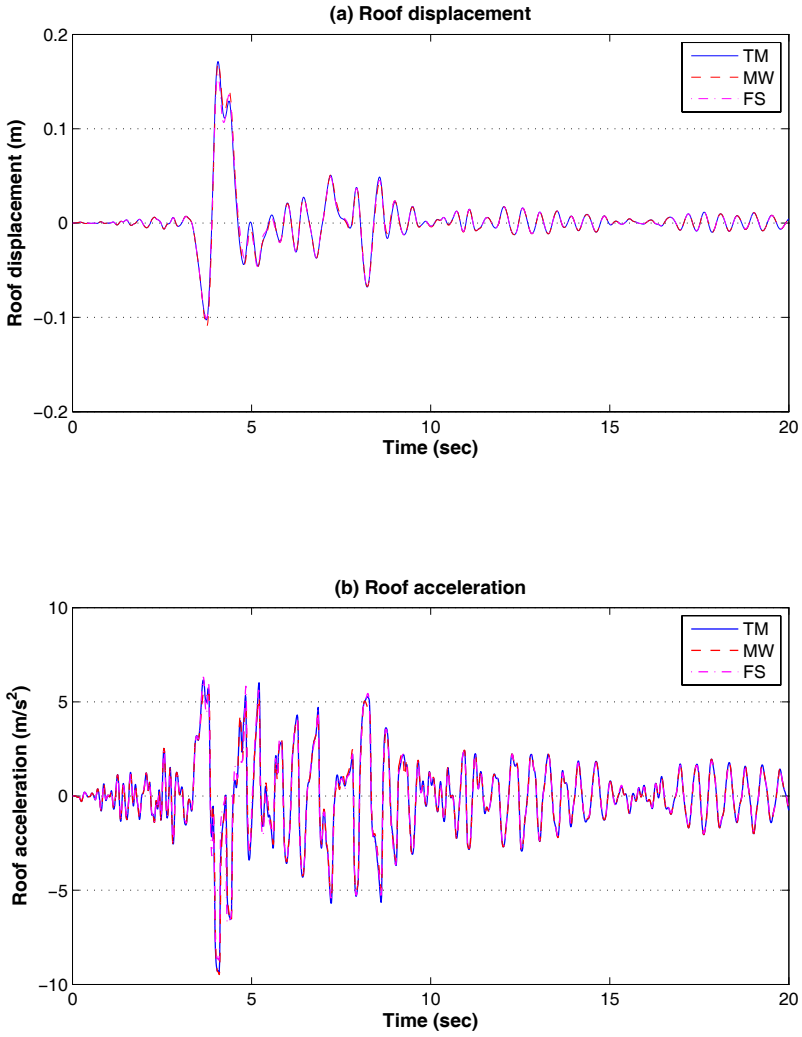

Figure 3.16 Time history response of the 6-story SFDB frame under earthquake ground motion LA-18: (a) roof displacement; (b) absolute roof acceleration

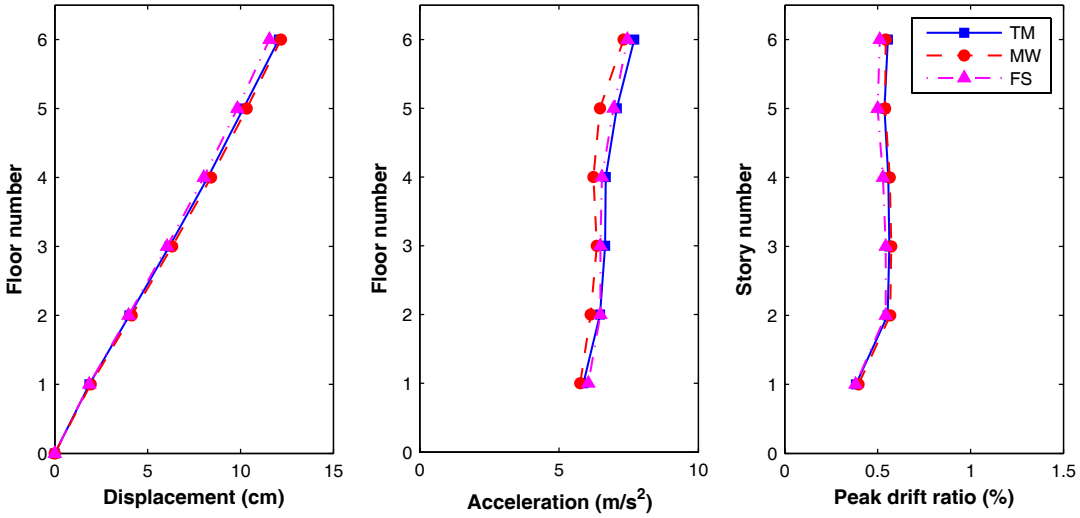

(a) Peak displacement (b) Peak acceleration (c) Peak inter-story drift ratio

Figure 3.17 Ensemble average of seismic response of the 6-story SFDB frame under design basis earthquakes

CHAPTER 4 DEVICE MECHANICS

This chapter presents a special type of bracing element termed self-centering friction damping brace (SFDB). The SFDB, with its core component made of superelastic Nitinol wires, exhibits a flag-shaped hysteresis loop, and thus it has a potential to establish a new type of concentrically braced frame systems with self-centering capability. This chapter describes the mechanical configuration and experimental test results of SFDB.

4.1 CONFIGURATION AND MECHANICS OF SFDB

The SFDB is a passive energy dissipating device that would be typically installed in a concentrically braced frame building as part of the bracing system which resists lateral seismic loads. The mechanical configuration of SFDB is schematically illustrated in Figure 4.1. The SFDB is comprised of three major steel parts, designated as block “A”, block “B” and block “C” respectivley. The slot on the block “B” enables these three parts to slide past each other at the contact surface. Stranded superelastic Nitinol wires are attached to block “A” and “B” using anchoring fixtures similar to that used in prestressed concrete. When the SFDB is subjected to either tension or compression force, the Nitinol wire strands in one direction will be always in tension. In order to enhance its energy dissipation capacity, a pre-determined amount of normal force is applied at the sliding surface 1 by tightening the bolts (as shown in Figure 4.1) and

thus produces a specified level of friction force at the sliding surface 1 of the SDB. Such a specified level of friction force is generally less than the 'yield' force of Nitinol wire strands in order to maintain the nearly self-centering effect of the brace. Meanwhile, much larger friction coefficient and normal force is applied at the sliding surface 2 to result in a friction force level that is larger than the 'yield' force of Nitinol wire strand by a pre-specified amount. Under low external force no sliding would occur along the surface 2 and two parts—blocks "B" and "C"—will move as one piece. Therefore without sliding of surface 2, the hysteretic behavior of the SDB is the superposition of the superelastic behavior of Nitinol wire strands and the friction effect at sliding surface 1, as illustrated in Figure 4.2.

Figure 4.2-(a) shows the typical hysteretic behavior of superelastic Nitinol wire strands which enable the self-centering capability of SFDB. This unique hysteresis is a result of stress-induced phase transformation from austenite to martensite and reverse transformation upon unloading. This important superelastic behavior involves certain energy dissipation with zero residual strain upon unloading. Figure 4.2-(b) shows the friction-induced hysteresis. The rectangular hysteretic loop corresponding to the friction effect indicates effective energy dissipation. By properly adjusting the ratio between the 'yield' strength of Nitinol wire strands and the friction forces, the final combined hysteresis loop exhibits a nearly self-centering behavior with enhanced energy dissipation, as illustrated in Figure 4.2-(c).

Energy dissipation by friction is a relatively inexpensive and reliable method which is insensitive to loading frequency and ambient temperature. Here friction damping is a critical part of energy dissipation in SFDB and it is also crucial to

achieve a predetermined level of friction force. Therefore special caution must be exercised on the design and fabrication of the frictional surfaces. Previous researches on friction dampers indicated that the cyclic response of frictional surface may be erratic due to stick-slip phenomenon and the degradation of slip load, and the friction coefficients of sliding interfaces especially those bimetallic interfaces may vary over time due to the corrosion, contaminants or other physiochemical process (Soong and Dargush 1997). However a repeatable and durable frictional performance can still be achieved through careful design of the friction surface and the device configuration. For example, using heavy duty brake lining pads at sliding surface can provide consistent and predictable frictional response which is quite similar to classic Coulomb behavior (Pall et al. 1980). Employing nonlinear disc springs or Belleville washers can also help maintain consistent bolts tension and therefore slip load (FitzGerald et al. 1989). A sealed outer casing can effectively preclude the environmental factors (e.g. corrosion of metal sliding interface).

Nitinol alloys, as most practical SMA, have an inherent self-centering capability, high ductility and corrosion resistance, and very long fatigue life compared to other shape memory alloy (SMA) materials. As mentioned earlier, the maximum recoverable strain of superelastic Nitinol wires can reach up to 8%, and they can sustain over two thousands load cycles under 8% strains cycles. These superior properties of superelastic Nitinol wires form the physical basis on which properly designed SFDB can re-center itself and withstand several design basis earthquakes without performance deterioration. Self-centering behavior is able to reduce (or even eliminate) residual structural deformation which is emphasized as a fundamental

complementary parameter in the evaluation of structural (and non-structural) damage in the performance-based seismic design and assessment approach. Additionally, as long as the strain of Nitinol wires does not exceed 8% during an earthquake, residual strain of the Nitinol wires would be negligible and thus no repair or replacement of SFDBs would be necessary after the earthquake if other parts of SFDBs are designed to remain elastic during earthquakes. The reusability of SFDB for several frequent and design level earthquakes is very appealing in the sense that it can enhance the robustness of structural system performance during strong aftershocks following a significant earthquake event, thus leading to minimized service interruption after strong earthquakes.

However, the plastic deformation and strain hardening associated with Nitinol wires in excess of 8% strain (as shown in Figure 2.5) will cause certain undesirable effects in SFDB frame. For example, the strain hardening behavior results in large peak force of SFDB, which may overload the brace connections and adjacent members. The plastic deformation may lead to the residual deformation of Nitinol wires after unloading and thus Nitinol wires would have to be replaced after earthquakes. One potential solution is to place a fuse device in series with the SFDB device so its strength is capped by the fuse device strength. In this study, a slotted bolted connection (i.e. the sliding surface 2 in Figure 4.1) with specified friction force level can be added at the end of SFDB so that this additional friction device begins to slip when the superelastic Nitinol wires reach a relative large strain (e.g. 8% strain). In this way, the maximum force of SFDB can be limited. However, when this additional

friction device slips, SFDB loses its self-centering capacity and residual deformation will result.

4.2 TESTING RESULTS

To validate the hysteretic behavior of SFDB, cyclic testing of scaled SFDB specimens was conducted. Figure 4.3 shows one of such SFDB specimens under test, which has a length of 2.3 feet. Each wire strand was comprised of superelastic Nitinol wires acquired from Johnson Matthey, Inc. The Nitinol wire had a diameter of 0.58 mm and the length of the wire strands was 254 mm (10 inch). It should be noted that the fuse friction device in SFDB is not included in scaled specimens under test. The cyclic test was carried out at room temperature on an MTS servohydraulic test machine and the loading frequency was 2 Hz. The Nitinol wires were preloaded for 50 cycles before formal cyclic test in order to minimize the accumulation of residual strain and degradation of strength in Nitinol wires. Figure 4.4-(a), (b) and (c) show the measured hysteretic loops of the SFDB specimens with different levels of friction force. The friction force was measured with the same loading protocol for the MTS test machine after removing the Nitinol wires. Figure 4.4-(d), (e) and (f) show the hysteresis of friction forces corresponding to Figure 4.4-(a), (b) and (c) respectively. For the tests corresponding to Figure 4.4-(a) and (d), no bolts were used to apply the normal force and lubricant oil was added to the sliding surfaces in the SFDB in order to minimize the friction force. As shown in Figure 4.4-(a) and (d), the friction force is negligible and this SFDB specimen has very limited energy dissipation capacity. With increasing

level of friction force, the SFDB specimens exhibit a hysteresis loop with enhanced energy dissipation capacity, as shown in Figure 4.4-(b) and (c).

It was observed that the load-displacement behaviors of both the friction force and the SFDB device were quite repeatable during the cyclic loading. No obvious residual strain and strength degradation in Nitinol wires were observed after the 50-cycle training, as shown in Figure 4.4-(a). The behavior of friction force is also repeatable with nearly rectangular hysteretic loops. It is seen in Figure 4.4-(a), (b) and (c) that the behavior of SFDB is almost symmetrical under tension and compression, which is another advantage of SFDB derived from its unique mechanical configuration in contrast to directly using SMA bars as bracing members in a concentrically braced frame structure. The unique configuration of SFDB enables the direct transfer of applied load to the Nitinol wire strands in tension. Although SMA bars can undertake both tension and compression forces, a significant difference in the behavior of SMA bars under compression and tension stresses has been observed by Cardone et al. (1999), which may cause problems in beam design due to the unbalanced forces in chevron-braced configurations of framed structures.

4.3 ANALYTICAL MODELING OF SFDB

This section discusses the analytical models for SFDB which are based on the nonlinear constitutive models for superelastic Nitinol wires along with the consideration of friction forces at two different sliding surfaces. Correspondingly, three new elements which utilize three different constitutive models described in last

chapter were developed in computer program DRAIN-2DX (Prakash et al. 1993) in order to simulate the behavior of SFDB.

The comparative study of three constitutive models in last chapter, which includes the nonlinear time history analyses of both SDOF systems and one 6-story prototype frame building equipped with SFDBs, indicates that it is acceptable to use rate-independent constitutive models for superelastic SMA in seismic analyses of structures, as along as the parameters of this rate-independent model are tuned to dynamic test data. Additionally, the SFDB is supposed to be installed inside buildings and thus not subject to significant thermal change. Considering its relative simple mathematical expression and good agreement with experimental results, the modified Wilde model is preferred in this study. Unless otherwise noted, the analytical model for SFDB base on the modified Wilde model for superelastic Nitinol wires will be used in the seismic analyses of SFDB frames in the following chapters.

The dynamic test results of Nitinol wires, acquired from Johnson Matthey, Inc, are used in this study to tune the parameters of the modified Wilde model because of their desirable properties such as later occurrence of strain hardening and larger yield strain than those from Memry Corporation. Figure 4.5 shows the stress-strain relationship of superelastic Nitinol wires from the experimental data and the modified Wilde model respectively. The cyclic tensile test was conducted at the loading frequency of 2 Hz. The details of the testing program are described in Section 2.2.4. The corresponding parameters of the modified Wilde model are listed in Table 4.1. As seen in Figure 4.5, the modified Wilde model can predict the stress-strain relationship of superelastic Nitinol wires reasonably well.

Figure 4.6 and Figure 4.7 show the typical hysteretic behavior predicted by the analytical model of SFDB with identical “yield strength” but two different friction force levels at sliding surface 1. The wire length in SFDBs is equal to 0.7 m. Figure 4.6 shows the hysteretic behavior of SFDB without contribution of friction damping at sliding surface 1, denoted as SFDB-NF, while Figure 4.7 shows the hysteretic behavior of SFDB with friction force at sliding surface 1 equal to 28% of total “yield” strength. Figure 4.6-(a) shows the completely self-centering behavior with relative small energy dissipation. But Figure 4.7-(a) indicates that the friction force can considerably enhance the energy dissipation of the device. Additionally, with the contribution of friction force, SFDB uses less volume of Nitinol wires, a relatively expensive material, to achieve the same “yield” strength. Meanwhile SFDB still retains a nearly self-centering behavior and only slight residual deformation after unloading can be observed in Figure 4.7-(a). Larger levels of friction force at sliding surface 1 are not recommended in order to keep the nearly self-centering properties. It is also seen in Figure 4.7-(a) that the stiffness value of SFDB changes before and after SFDB starts to slip over its friction surface. But the secant stiffness at the “yield” point of SFDB (as shown by dashed line in Figure 4.7-(a)) is almost equal to the initial stiffness of SFDB-NF.

In both braces shown in Figure 4.6 and Figure 4.7, the friction fuse devices are designed to slip when the strain in Nitinol wires reaches 8% for the reasons mentioned before. Figure 4.6-(b) and Figure 4.7-(b) show the hysteretic behavior of two braces under large amplitude vibration. The maximum strength of SFDB or SFDB-NF is about two times as large as their ‘yield’ strength. Such overstrength has to be taken

into account in the design of the brace connections and adjoined members. The activation of fuse friction devices leads to considerable residual deformation after unloading, and SFDB or SFDB-NF will lose its self-centering properties.

Unless otherwise noted, the setting of the SFDB or SFDB-NF, including the parameters of the modified Wilde model and the friction force levels at two sliding surfaces, will also be used in the nonlinear time history analyses of SFDB frames in the following chapters.

4.4 SUMMARY

This chapter presents a new special bracing element termed self-centering friction damping brace (SFDB) and the seismic behaviors of SFDB frame buildings. SFDB would be typically installed as part of the bracing system to resist lateral seismic load. In the SFDB, stranded superelastic Nitinol wires are used as its core self-centering component while enhanced energy dissipation is achieved through friction. By properly adjusting the ratio between the 'yield' strength of superelastic Nitinol wire strands and friction force in the SFDB, hysteresis loops with nearly self-centering behavior can be obtained for the SFDB. A validation-of-concept test on scaled SFDB specimens was carried out at a dynamic loading rate and the experimental result clearly demonstrates the nearly self-centering behavior of the SFDB with enhanced energy dissipation from friction.

Compared with conventional braces for steel frame buildings, properly designed SFDB has several desirable performance characteristics such as minimized residual

drifts of CBF system and its ability to withstand several design level earthquakes without the need for replacement, due to the unique behavior of superelastic Nitinol wires such as re-centering effect, full strain recovery and long fatigue life. The SFDB thus has a potential to establish a new type of CBF systems with self-centering capability.

The analytical models for SFDB are developed based on the nonlinear constitutive models for superelastic Nitinol wires (as described in Chapter 3) along with the consideration of friction forces at surfaces. Correspondingly, three new elements were developed in computer program DRAIN-2DX (Prakash et al. 1993) in order to simulate the behavior of SFDB. The analytical model for SFDB and the associated parameters which will be used in the following chapters are also presented.

It should be noted that classic Coulomb behavior is assumed for frictional response in the analytical model for SFDB and predetermined levels of slip load are assigned to two frictional surfaces. But actual frictional response may be affected by selection of material, surface condition, mechanical configuration and other environmental factors. Future research still needs to be done on the design of the frictional surface to achieve the specified friction force levels with acceptable tolerance.

Table 4.1 The parameters of the modified Wilde model for superelastic Nitinol wires (Type B)

Parameter	Units	Value
E	MPa	38,800
E_m	MPa	16,500
ε_m	--	0.065
ε_1	--	0.053
Y	MPa	395
α	--	0.036
f_T	--	0.045
a	--	110
c	--	0.77
n_1 (loading)	--	7
n_2 (unloading)	--	0.9

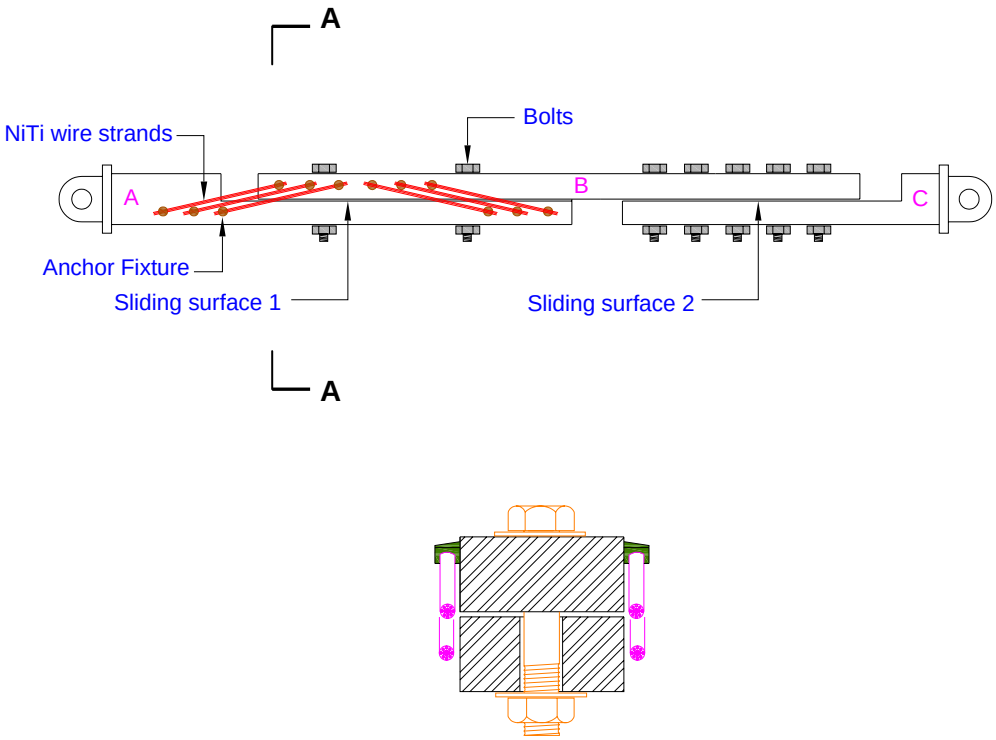

Cross section A-A

Figure 4.1 Schematic of the mechanical configuration of SFDB

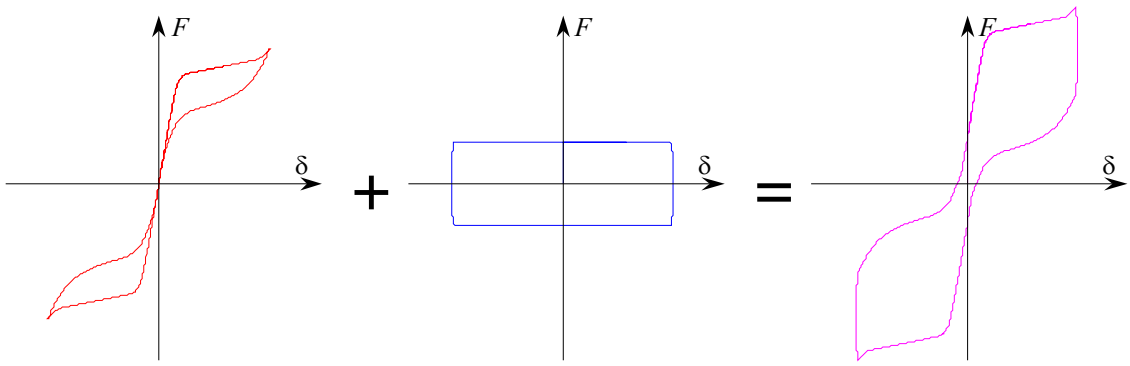

(a) self-centering *by* **superelastic Nitinol wires**

(b) Energy dissipation *by* **friction**

(c) Final behavior *of* **SFDB**

Figure 4.2 Illustration of the self-centering mechanism of SFDB

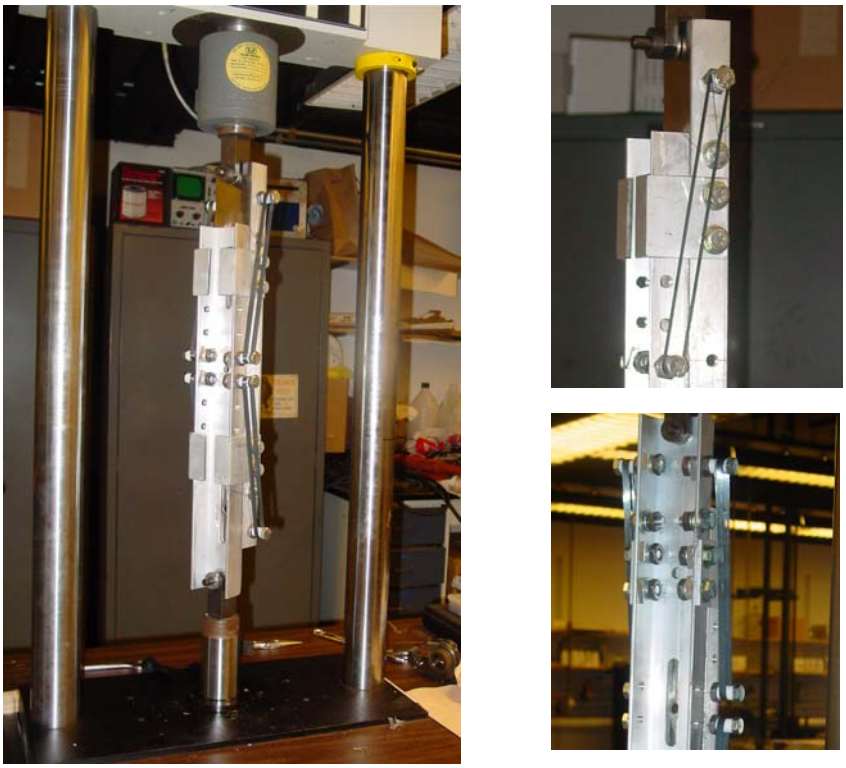

Figure 4.3 View of scaled SFDB specimen under test

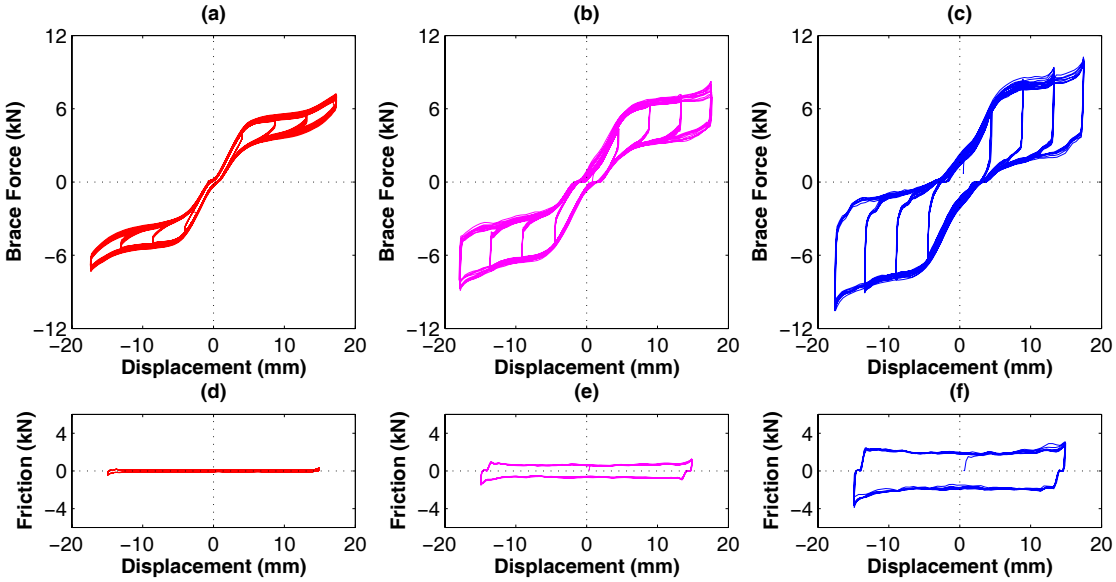

Figure 4.4 Test results of SFDB specimens

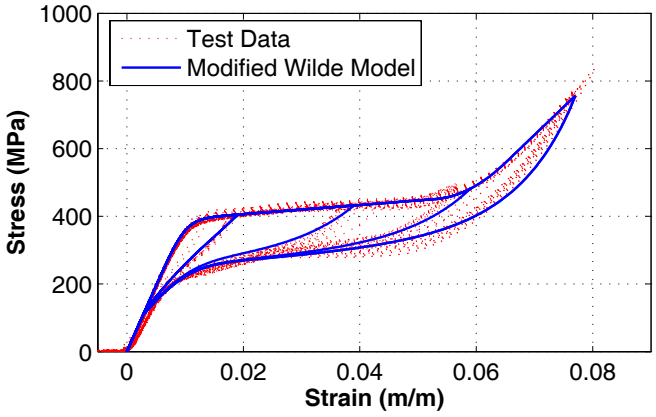

Figure 4.5 Stress-strain curve of superelastic Nitinol wire

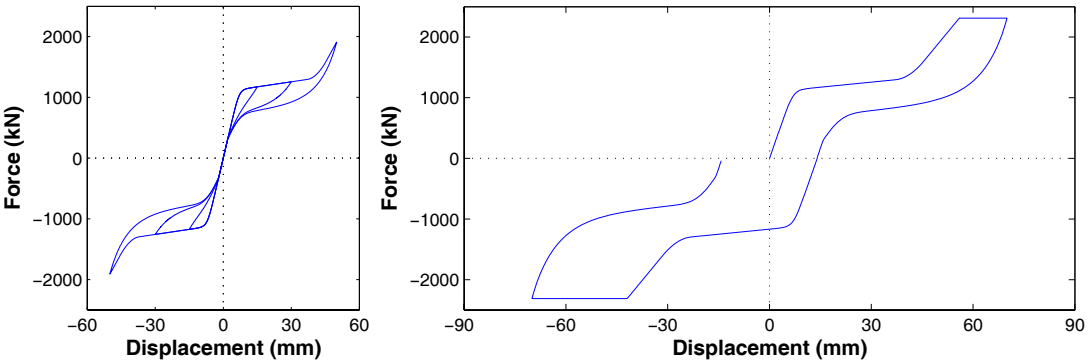

(a) (b)

Figure 4.6 Typical hysteresis of SFDB-NF under small and large amplitudes

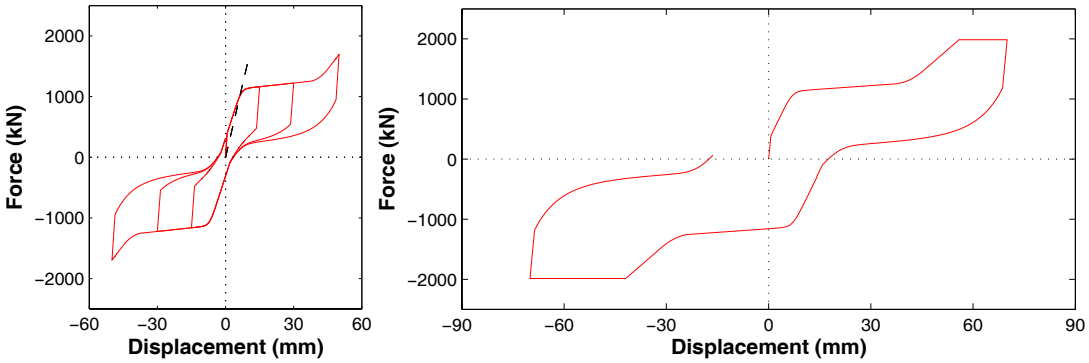

(a) (b)

Figure 4.7 Typical hysteresis of SFDB under small and large amplitudes

CHAPTER 5 COMPARATIVE STUDY OF SFDB AND BRB

5.1 INTRODUCTION

Buckling-restrained braces (BRB), which are capable of yielding in both tension and compression, have been developed to overcome the buckling problem of conventional braces in concentrically braced frame (CBF) systems (Fahenstock et al. 2003; Sabelli 2003; Uang 2004). In buckling-restrained braced frames (BRBF), BRB is used to replace the bracing members of concentrically braced frames. BRBF has been used extensively for seismic applications in Japan after the 1995 Kobe earthquake and is also gaining popularity in the United States. BRBFs are desirable for seismic design and rehabilitation for their superior ductile performance in comparison with conventional CBFs. Clark et al. (1999) redesign of a 3-story steel special moment-resisting frame into a BRBF resulted in about 50% reduction of the total weight of the steel. Nonlinear dynamic analyses by Sabelli et al. (2003) have shown that the behavior of BRBFs is comparable and often better than that associated with conventional concentrically braced frames and moment frames. However, several potential problems have also been identified for BRBF by a few researchers (Sabelli 2003; Kiggins and Uang 2004): (1) large residual story drifts that could be as high as 40% to 60% of the peak drifts; (2) tendency of BRBs to yield at frequent earthquakes

with a 50% probability of exceedence in 50 years. Costly repair after strong earthquakes might be necessary due to these problems.

This chapter presents a comparative study of SFDB frames and BRBF, both of which are concentrically braced frame system. The configuration and mechanism of SFDBs are described in Chapter 4. The results of nonlinear time history analyses under different seismic intensity levels, as well as nonlinear pushover analyses, are presented for both types of frames. The comparative study shows that SFDB frames are capable of achieving a seismic response level comparable to that of BRBF while having significantly reduced residual drifts under frequent and design basis earthquakes.

5.2 NONLINEAR SEISMIC ANALYSES

This section presents the results of nonlinear time history analyses and pushover analyses of both SFDB frames and BRBFs.

5.2.1 Prototype Steel Braced Frame Building

In this study, a 3-story and a 6-story CBF with either SFDBs or BRBs are selected as the prototype structures for the comparative study. These prototype structures have been used by Sabelli et al. (2003) and Kiggins and Uang (2006) in their study of BRBF previously. The details about these prototype structures are described in Appendix B. For 3-story building, the seismic mass is 5.86×10^5 kg for 1st and 2nd levels, 5.95×10^5 kg for 3rd levels; for 6-story building, it is 6.49×10^5 kg for the 1st

through 5th levels, and 5.66×10^5 kg for 6th level. Like BRB, typically SFDBs would also be part of the bracing system of concentrically braced frame. Thus the SFDBs would be installed at the same locations as shown in Figure B.1 and Figure B.2. The 'yield' capacities of SFDBs are equal to the average of tensile and compressive strength of corresponding BRBs. The lengths of superelastic Nitinol wire strands in the SFDBs is 0.85 m for the 1st story and 0.7 m for all other stories, which translates into 8% strain in the superelastic Nitinol wires at a 2% story drift ratio. The friction force at sliding surface 1 in the SFDBs is set to be 28% of brace 'yield' strength.

In order to examine the effectiveness of friction in energy dissipation, a self-centering brace without friction, denoted as SFDB-NF, was also included as a reference case in this study. The 'yield' capacities of SFDB-NFs are assigned to be equal to the corresponding SFDBs'. It should be noted that without friction damping, the SFDB-NF requires the use of more Nitinol materials than regular SFDBs in order to achieve the same 'yield' strength.

It is noted that the stiffness value of SFDB changes before and after SFDB starts to slip over its friction surface. Therefore, the effective initial stiffness of SFDB is defined as the secant stiffness corresponding to the 'yield' point on the load-displacement curve, which is very close to that of the SFDB-NF. With the aforementioned 'yield' strength and Nitinol wire length, the effective initial stiffness of SFDB-NF in each story is about 75% that of corresponding BRBs. Modal analysis was conducted to determine the natural periods of the prototype buildings. For the BRBFs, the fundamental periods for the 3-story and 6-story buildings are 0.41 seconds

and 0.61 seconds, respectively; for the SFDB-NF frames, the first periods for the 3-story and 6-story buildings are 0.45 seconds and 0.67 seconds, respectively.

As mentioned earlier, in this study, 8% strain is specified as the maximum recoverable strain (without residual deformation) of superelastic Nitinol wires. The friction surface 2 is designed to slip only when the strain in Nitinol wires strands reaches 8% strain for both types of SFDB braces. If the strain in Nitinol wires was lower than 8% during an earthquake, residual strain of the Nitinol wires would be negligible and thus no repair or replacement of SFDBs would be necessary after the earthquake if other parts are designed to remain elastic during design basis earthquakes. Once the slip of friction surface 2 occurs, the SFDBs will lose their self-centering capability, which could take place under maximum considered earthquakes. It should be noted that the friction force levels at different sliding surfaces in SFDBs are the same as described in Chapter 4.

5.2.2 Nonlinear Analysis Method

Nonlinear time history and pushover analyses were carried out using the computer program DRAIN-2DX (Prakash et al. 1993). Only one bay of the braced frame was modeled and analyzed in this study. Rigid floor diaphragm is assumed for both buildings and thus all nodes on the same floor are constrained together in the horizontal direction of the input ground motion. More description of analytical models can be found in Appendix B.

Element type 1 in DRAIN-2DX, i.e. inelastic truss bar element, was used to simulate the hysteretic behavior of BRB. In order to simulate the hysteretic behaviors of SFDBs, one new element in DRAIN-2DX was developed using the analytical model for SFDB. The details of the analytical model, including the parameters used in the model, can be found in Chapter 4. Figure 5.1-(a) to (c) shows the typical hysteresis (i.e., brace force vs. displacement) of a single brace in the top story of the 6-story building for the BRB, SFDB and SFDB-NF respectively.

In this study, equivalent viscous damping ratio, defined as the energy dissipated in one cycle divided by the product of 4π and maximum strain energy, is selected as a quantitative index to measure the energy dissipation capacity of SFDB. The equivalent viscous damping ratios of SFDB-NF at three different displacement levels (in ascending order, as shown in Figure 5.1-(c)) are 4.2%, 6.3% and 5.5% respectively; while the equivalent viscous damping ratios of SFDB at corresponding displacement levels as shown in Figure 5.1-(b) are 19.0%, 20.4% and 17.7% respectively. The equivalent viscous damping ratios of BRB at corresponding displacement levels indicated in Figure 5.1-(a) are 42.0%, 51.9% and 54.3% respectively. It can be seen the friction effect in SFDB enhances the energy dissipation capacity of the brace at various displacements. BRB is seen to have the largest energy dissipation capacity, and the equivalent damping ratios of BRB are over twice that of corresponding SFDB. However, it is pointed out by Christopoulos et al (2002a), Christopoulos and Pampanin (2004) that self-centering systems with flag-shaped hysteresis can achieve a similar seismic deformation level to elastoplastic systems even the self-centering system dissipates much less hysteretic energy than the elastoplastic system. It is seen

in Figure 5.1-(b) that the SFDB has a nearly self-centering behavior due to relatively large friction force. The largest residual deformation of this SFDB after fully unloading corresponds to a 0.075% inter-story drift in this study, which is negligibly small. Furthermore, the nonlinear time history analyses revealed that the residual story drifts of the prototype framed buildings under the two suites of frequent and design basis earthquakes are much lower than 0.075%.

5.2.3 Nonlinear Pushover Analyses

Nonlinear static analyses or pushover analyses were conducted to evaluate the nonlinear lateral load response and failure mechanism of SFDB frames. NEHRP *Recommended Provisions* (FEMA 2003) was followed to determine the lateral load distribution. Figure 5.2 and Figure 5.3 show the pushover curve (base shear versus roof drift ratio) for the 3-story and 6-story SFDB frames and BRB frames respectively. Various characteristic points such as the slip at friction surfaces of SFDB, 'yield' of braces (BRBs or SFDBs), are also indicated in Figure 5.2 and Figure 5.3.

Initial stiffness change in SFDB frame can be observed from its pushover curve shown in Figure 5.2 and Figure 5.3. The friction surfaces in SFDBs begin to slip at very small roof displacement. Before and after the slip, the stiffness of the SFDB frame changes. With the afore-mentioned definition of the effective initial stiffness for SFDBs, the effective initial stiffness of SFDB frame is slightly smaller than that of BRB frame. But the post-'yield' stiffness of the 6-story SFDB frame is slightly greater

than that of the BRB frame until the SFDB frame shows hardening behavior at roof drift ratio beyond 1.5%.

As shown in Figure 5.2 and Figure 5.3, the 'yield' strength and displacement of both frames is very close to each other. Both frames yield at relatively small roof drift ratio (about 0.25%). This explains why BRBs tend to yield even under frequent earthquakes. However, the 'yield'-like plateau of SFDB frame is induced by the phase transformation of superelastic Nitinol instead of plastic deformation. Before the occurrence of plastic deformation in beams and columns, there is essentially no damage in the SFDB frame. Therefore the SFDB frame can achieve the goal of damage-free structure for frequent earthquakes and design basis earthquakes, and thus leads to considerably reduced repair cost and service interruption after earthquakes.

As described earlier, the 8% strain of Nitinol wire corresponds to approximately 2% inter-story drift ratio for both the 3-story and 6-story SFDB frames. Figure 5.2 and Figure 5.3 shown that the friction surface 2 in SFDBs begins to slip at around 2% roof drift ratio. As a fuse device, the slotted bolted connection at the end of SFDB caps the maximum force of SFDB as well as the base shear force. Thus this fuse device can effectively prevent the occurrence of undesirable plastic deformation and potential overloading of brace connections and adjoined members that may be caused by apparent strain hardening associated with superelastic Nitinol wire in excess of 8% strain. However, when this additional friction device slips that may happen under MCE earthquakes, SFDB loses its self-centering capacity and residual deformation will result. The corresponding unloading path (in dashed line) of SFDB frames are also shown in Figure 5.2 and Figure 5.3. If SFDB is intended to be made self-

centering even under MCE earthquakes, the length of Nitinol wire strands can be increased as compared to the design length for DBE earthquake. However, doing so will sacrifice the performance under DBE since increased wire length leads to reduced initial effective stiffness of SFDB.

5.2.4 Nonlinear Time History Analyses

The time history analyses employ the suites of earthquake ground motions developed previously by Somerville et al. (1997) for use in the FEMA project on steel moment-resisting frames. Three earthquake suites corresponding to downtown Los Angeles, California, were selected in this study and they are designated as LA01 - LA20 (for DBE level), LA21 – LA40 (for MCE level) and LA41 - LA60 (for FE level), respectively. More details about these ground motion sets can be found in Appendix A.

Figure 5.4 to Figure 5.7 show the results of a comparative study of the seismic response behaviors of the BRB and SFDB frames under DBE suite of earthquake ground motions, i.e. with 10% of probability of exceedance in 50 years. Figure 5.4-(a) and (b) respectively show the maximum drift ratios and residual drift ratios of the 3-story BRB and SFDB frames subjected to the DBE suite of ground motions. SFDB-NF represents the case in which SFDB braces with no friction were used; therefore, in the SFDB-NF case, energy is dissipated only through the superelastic Nitinol wires and SFDB-NF has reduced energy dissipation capacity compared with normal SFDB. Under the DBE suite, the mean values of the maximum drift ratios of the BRB, SFDB and SFDB-NF frames are 0.77%, 0.88% and 1.51% respectively, while the mean

residual drift ratios are 0.28% and 0.11% for the BRB frame and SFDB-NF frame respectively, and almost zero for the SFDB frames.

Figure 5.5 shows the maximum drift ratios and residual drifts ratios for the 6-story building, from which similar observations can be made. The mean values of the maximum drift ratios of the BRB, SFDB and SFDB-NF frames are 0.84%, 0.77%and 1.51% respectively, while the mean residual drift ratios are 0.32% and 0.04% for the BRB frame and SFDB-NF frame respectively, and almost zero for the SFDB frame. The large maximum story drift corresponding to the SFDB-NF frame can be explained by the fact that the stiffness and energy dissipation capacity of the SFDB-NF are smaller than those of the corresponding BRB in this study. However, with the increase of energy dissipation capacity by utilizing the friction effect, the SFDB frames can achieve a control performance comparable to the BRB frames in terms of peak inter-story drifts under the DBE suite of ground motions, despite the fact that SFDB has less energy dissipated in each cycle than BRB. This is consistent with the observation made by other researchers (e.g., Christopoulos et al 2002a, Christopoulos and Pampanin 2004). The residual story drifts of SFDB frames were negligible under all twenty ground motions, while non-trivial residual story drifts were observed in the BRB frames under over 10 ground motions. Therefore the SFDB frame has the potential to achieve a control performance comparable to the BRB frame under DBE earthquakes in terms of peak story drift ratios, but has considerably reduced residual drifts. Even with much greater peak drift ratios, the SFDB-NF frames still have smaller mean residual drifts than the BRB frames. This reduction of residual drifts in

both the SFDB-NF and SFDB frames manifests the benefit of SFDB which is derived from its self-centering capability.

In this study the largest recoverable strain of Nitinol wires and the slip of friction surface 1 in SFDB correspond to a transient inter-story drift ratio value of 2% for the prototype building structures. For SFDB-NF frames, the peak story drift ratios exceed 2% under five ground motions for both 3-story and 6-story frames due to inadequate energy dissipation capacity of SFDB-NF, and consequently noticeable residual drifts can be observed in those cases. With the peak story drift below 2% in other cases, the residual drifts of SFDB frames are still negligible. But the peak story drift ratios of both 3-story and 6-story SFDB frames were always less than 2% under the twenty ground motions, and thus the SFDBs need not be repaired and the reusability of SFDB is validated in a statistical sense.

Figure 5.6 and Figure 5.7 show the statistical results of the nonlinear seismic response, including the distribution of the peak displacements, peak acceleration, peak story drift ratio and residual story drift ratio along the building height, of the 3-story and 6-story prototype structures respectively under the DBE suite. The ensemble average was calculated based on the twenty earthquake ground motions in the DBE suite. It is clearly seen that the SFDBs are capable of achieving the same level of seismic response control as the BRBs in terms of structural displacement, acceleration and peak story drifts. Furthermore, the SFDB frames have almost zero residual story drifts in all six stories, while for the BRB frame non-trivial residual story drifts were observed in all stories of both prototype structures (as shown in Figure 5.6-(d) and Figure 5.7-(d)), and the maximum residual story drifts are about 0.25% for both

prototype structures. The ensemble average of the residual drift ratios of the BRB frames are about 30% of the peak story drift ratio under the design basis earthquakes. However, without the contribution of energy dissipation from friction force, the SFDB-NF frames have greater structural response than the BRB frames except for the residual story drift. It is worth noting that although the SFDB is capable of achieving much superior performance than the SFDB-NF in seismic response control and reusability, SFDB uses less volume of Nitinol wires which is a relatively expensive material.

Figure 5.8 and Figure 5.9 show the statistical results of the seismic responses of 3-story and 6-story frames respectively under FE suite (i.e. with 50% probability of exceedence in 50 years). Observations similar to what was made for the DBE suite can also be made here. The SFDB frame can achieve a similar seismic response control level to that of the BRB frame, but it has much smaller residual drifts. It was noted that even under the FE suite, some BRBs exceeded the yield strain under about fifteen ground motions out of a total of twenty records for both the 3-story and 6-story building. This observation confirms the findings by other researchers (e.g., Sabelli et al. 2003) that BRB tends to yield even under frequent earthquakes.

Figure 5.10 and Figure 5.11 show the statistical results of the seismic responses of the 3-story and 6-story frames respectively under the MCE suite (i.e. with 2% probability of exceedence in 50 years). It is seen that under the MCE suite residual drifts with a varying degree of severity occur in all three types of frames. In general, under MCE earthquake, the SFDB frame has larger seismic response than the BRB frame in terms of structural displacement, acceleration and peak story drifts, while

they are still much smaller than those corresponding to the SFDB-NF frame. Compared with the BRB frame, the SFDB frame has much smaller residual drifts even if it is not completely self-centering after activating the friction surface 2 under MCE earthquake. It is also observed that the residual drifts of SFDB-NF frame are close or even larger than those of BRB frames.

Caution should be exercised on the relatively high acceleration demands in SFDB frames under MCE earthquakes, compared with BRB frames. Especially for 6-story prototype buildings, the maximum acceleration for SFDB and SFDB-NF frames is about 2 g and 3 g respectively. Such a large acceleration may cause undesirable damage to building contents and acceleration sensitive components. These potential issues associated with MCE earthquakes need to be carefully considered in future study of SFDB frames.

To better understand the seismic response behaviors of the SFDB frames, Figure 5.12 and Figure 5.13 show the typical time histories of the inter-story drifts and acceleration responses of the 3-story BRB and SFDB frames subjected to the LA18 earthquake ground motion. This LA18 record was derived from the ground motion recorded at Sylmar during the 1994 Northridge earthquake (Somerville et al 1997). It is seen in Figure 5.12 that the BRB frame has non-trivial residual story drifts in all stories after this earthquake, while the corresponding SFDB frame has almost zero residual story drifts in all stories. Figure 5.13 shows the acceleration response of the 3-story SFDB frame has the same magnitude as that of the BRB frame at all floor levels. The observation similar to Figure 5.12 can also be made to Figure 5.14, which shows

the time history of inter-story drifts of 6-story BRB and SFDB frames under LA18 ground motions.

Figure 5.15 is a scatter plot of spectral displacement versus the maximum drift ratios for both the BRB and SFDB frames. The spectral displacement is defined as the peak displacement response of an equivalent single-degree-of-freedom (SDOF) system under an earthquake ground motion and is calculated based on the fundamental period of the respective frame buildings. It is believed that the spectral displacement reflects the earthquake intensity level to certain extent. Figure 5.15 involves the results corresponding to FE, DBE and MCE levels, totaling 60 ground motions. The dispersion of the data points increases with the spectral displacement. Other factors such as building height, different seismic regions and seismic levels, higher modes, P-Δ effect and inelastic behavior of different hysteresis may also affect the relation between the spectral displacement and maximum story drift ratio (Gupta and Krawinkler 2000; Pampanin et al. 2003). For the 3-story and 6-story buildings under consideration, at small spectral displacements, the SFDB frame has smaller maximum drift ratios than the BRB frame, while with the increase of spectral displacement, the maximum story drift ratios of SFDB frame become larger than BRB frame.

The damage in other structural members was also evaluated in this study. For the 3-story BRB and SFDB frames, no plastic hinges except at column bases occurred under the DBE suite earthquakes. In the 3-story BRB frame, column base yielded under only two earthquake records - LA16 and LA18, and the corresponding column base plastic rotations are 0.0012 and 0.0056 respectively. In the 3-story SFDB frame, column bases yielded under three earthquake records - LA14, LA16 and LA18, and

the corresponding plastic rotations are 0.0021, 0.0033 and 0.0017 respectively. The larger roof displacement and maximum story drifts of the SFDB frame than those of the BRB frame under LA14 and LA16 is the cause for large plastic base rotations. Figure 5.16 shows the axial load-bending moment interaction at the column base for both the BRB and SFDB frames under LA16. It is noted that in all the 'yielded' cases, minor yielding at column base only occurred in one load cycle. For both 6-story BRB and SFDB frames, no column base yielding was observed for all 20 records in the DBE suite.

5.3 CONCLUSIONS

This chapter presents a comparative study between BRB frames and SFDB frames through nonlinear time history and pushover analyses of two prototype buildings – a 3-story and a 6-story steel braced frame. The time history analyses involve three suites of earthquake ground motions which represent the frequent, design basis and maximum considered earthquake levels respectively in Los Angeles, California. The following conclusions are drawn based on the results of nonlinear time history and pushover analyses:

- SFDB frames have almost negligible residual story drifts under the FE and DBE earthquakes, while noticeable residual drifts occur in SFDB frame under MCE earthquakes. In general, SFDB frames have significantly reduced residual story drifts in comparison with BRB frames which is a beneficial effect derived from the self-centering behavior of SFDBs.

- In terms of peak story drifts and absolute acceleration response, SFDB frames are capable of achieving a seismic response control level comparable to that of the BRB frames under FE and DBE earthquake levels. However, BRB frames are seen in this research to have better control performance under MCE earthquakes.
- The pushover analyses result discloses the nonlinear lateral load response behavior and failure mechanism of SFDB frames. Characteristic performance points of SFDB frame such as the slip at friction surfaces and 'yielding' of braces are indicated in the pushover curve.
- Due to the unique behavior of superelastic Nitinol wires such as full strain recovery and long fatigue life, SFDB, if properly designed, has the potential to withstand several frequent or even design basis earthquakes without the need for replacement.
- Incorporating friction damping in SFDB can significantly improve its seismic performance.
- The friction fuse mechanism in SFDBs can effectively cap the maximum strength of SFDBs, which prevents possible overloading of adjoined connections and members under MCE earthquakes.

It is worth noting that the prototype buildings considered in this chapter were originally designed for BRB frames by other researchers. For a fair comparison, the 'yield' strength of the SFDB is intentionally set to be equal to that of the corresponding BRBs. However, considering SFDB's different energy dissipating and hardening behavior at large drift, the parameters of the SFDBs considered in this study do not represent an optimal design for the SFDB frame. For example, the overloading

to brace connections and very high acceleration demands may occur under MCE earthquakes. A design procedure developed for SFDB frames are presented in next chapter.

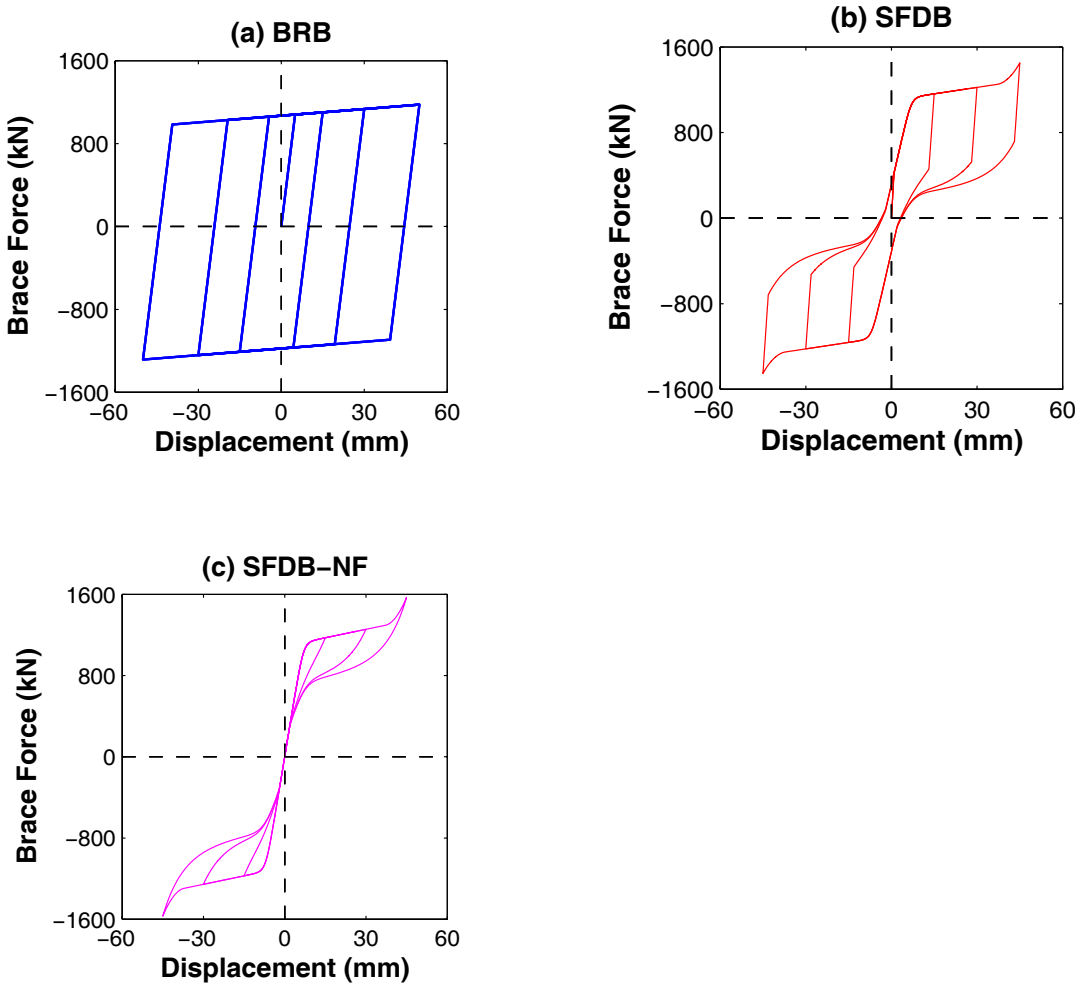

Figure 5.1 Typical hysteresis of single brace in the 6th story of the prototype building

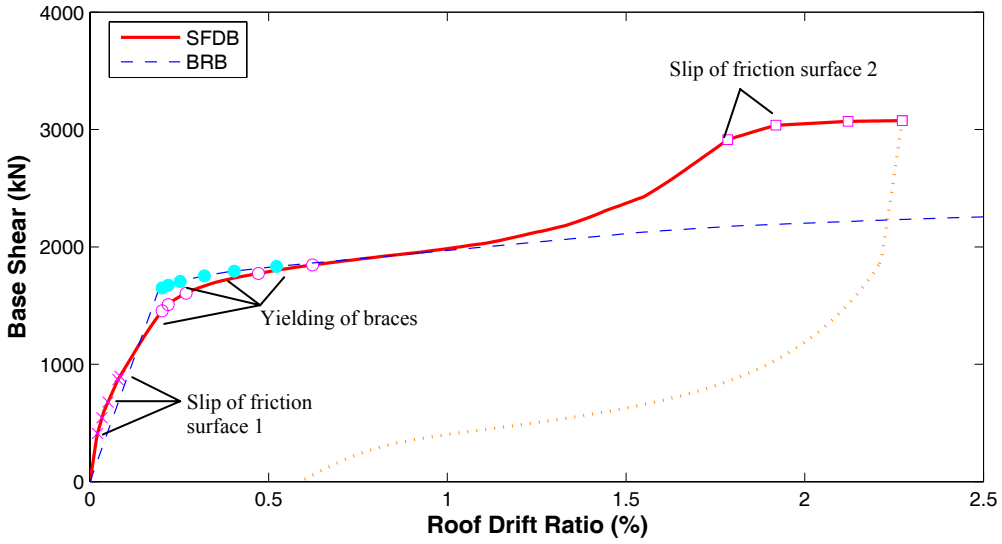

Figure 5.2 Static pushover analyses of the 3-story BRB frame and SFDB frame

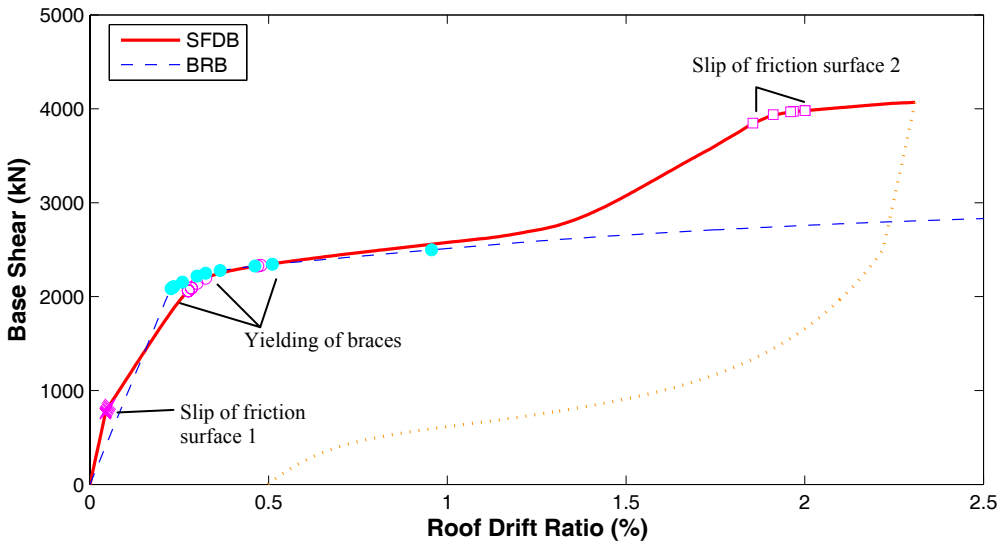

Figure 5.3 Static pushover analyses of the 6-story BRB frame and SFDB frame

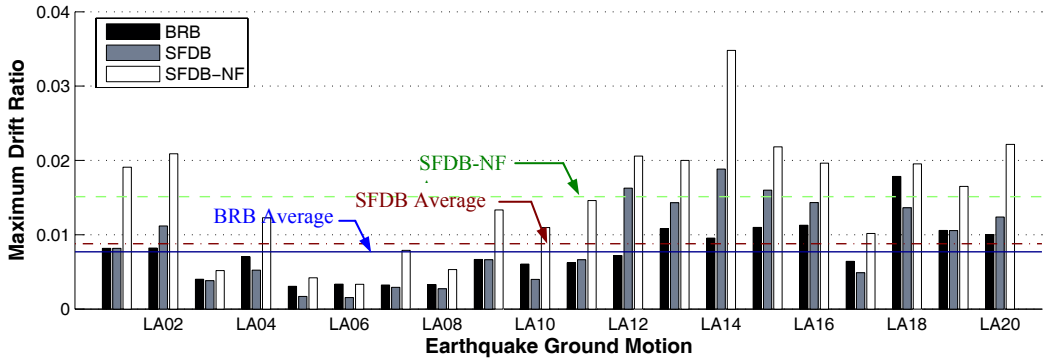

(a) Maximum inter-story drift ratios

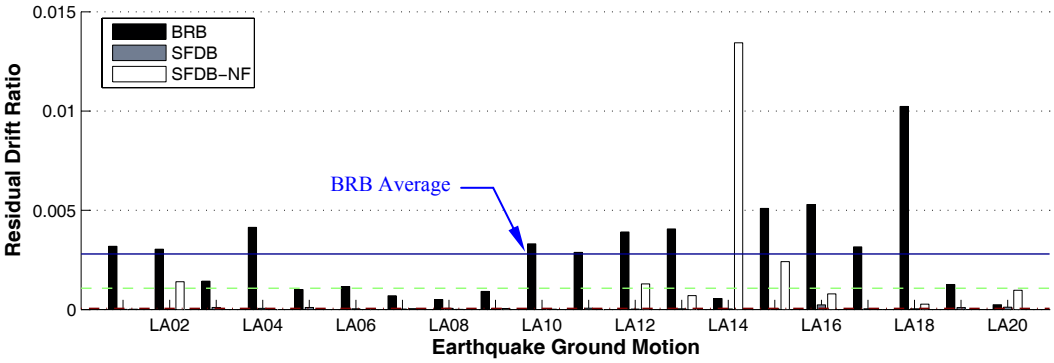

(b) Residual inter-story drift ratios

Figure 5.4 Maximum and residual drift ratios for the 3-story frame building under DBE earthquake

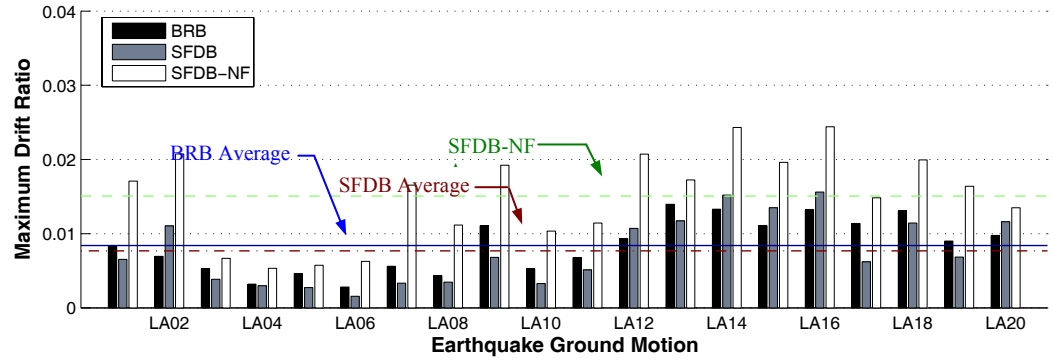

(a) Maximum inter-story drift ratios

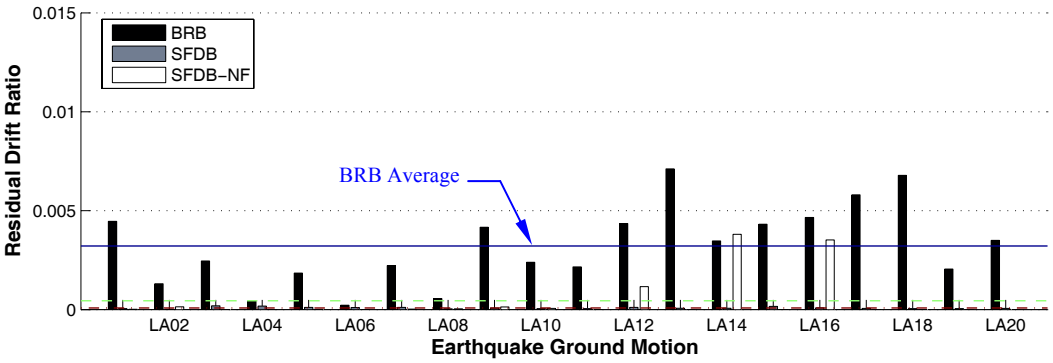

(b) Residual inter-story drift ratios

Figure 5.5 Maximum and residual drift ratios for the 6-story frame building under DBE earthquake

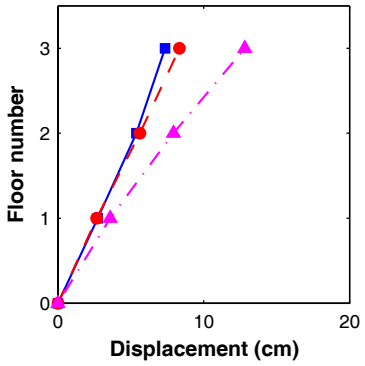

(a) Peak displacement

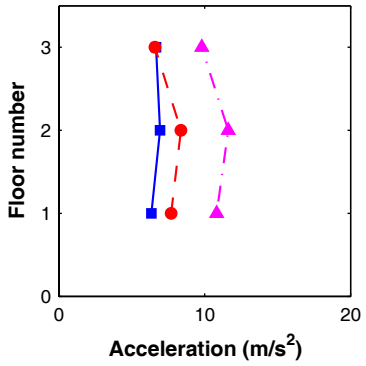

(b) Peak acceleration

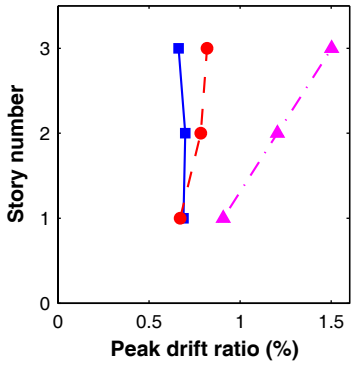

(c) Peak story drift ratio

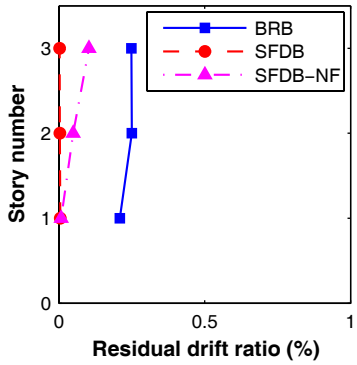

(d) Residual story drift ratio

Figure 5.6 Ensemble average of seismic response of the 3-story prototype building under design basis earthquakes

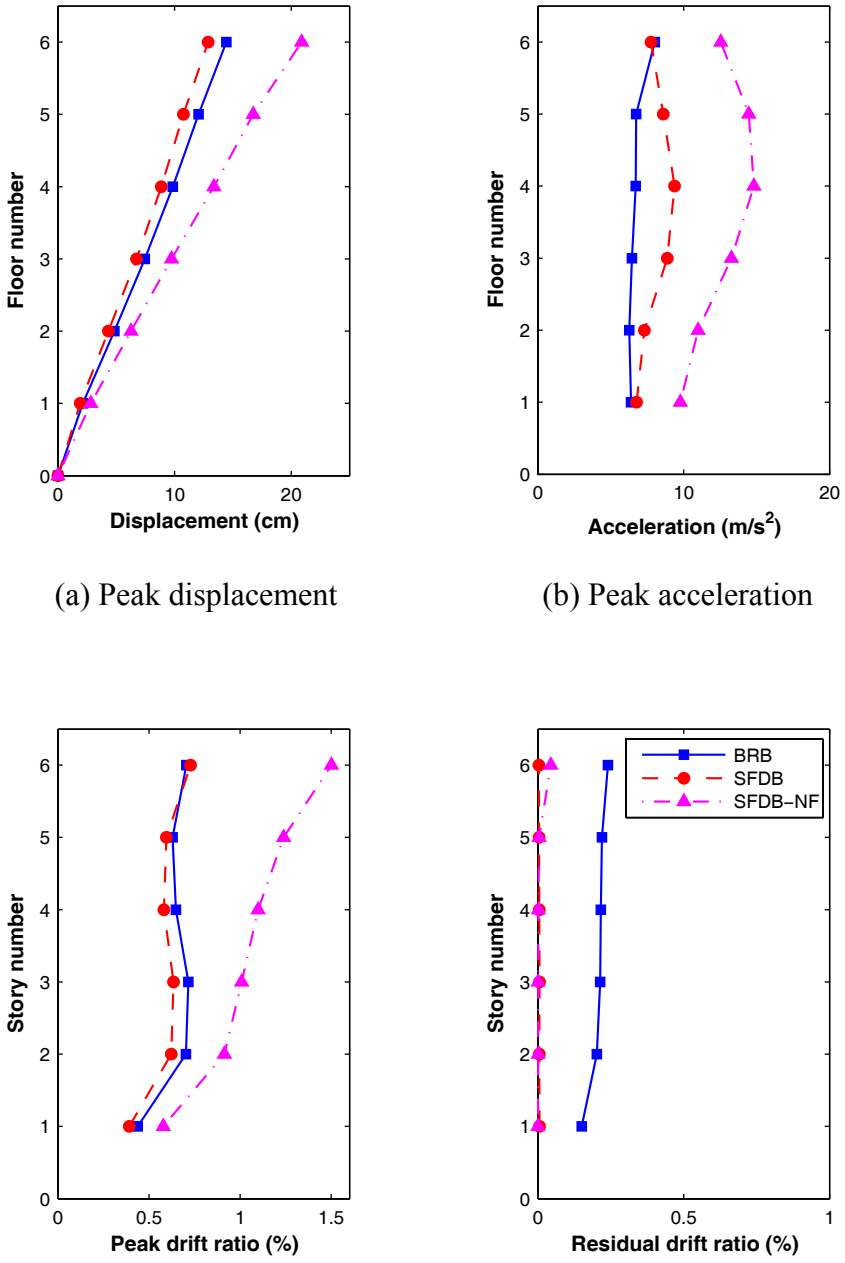

(a) Peak displacement (b) Peak acceleration

(c) Peak story drift ratio (d) Residual story drift ratio

Figure 5.7 Ensemble average of seismic response of the 6-story prototype building under design basis earthquakes

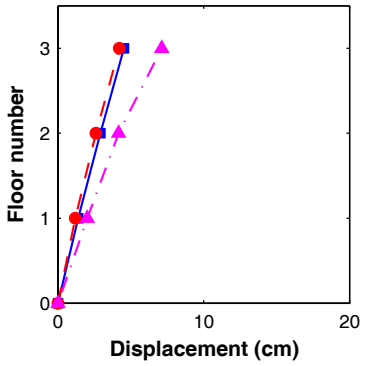

(a) Peak displacement

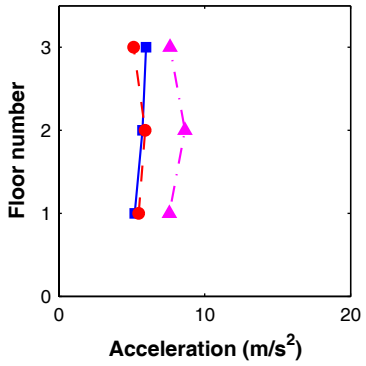

(b) Peak acceleration

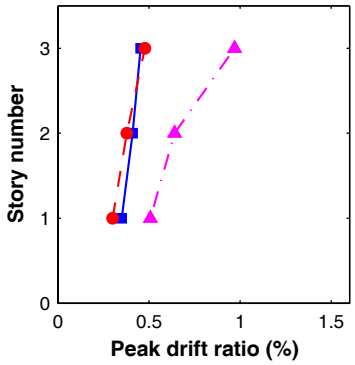

(c) Peak story drift ratio

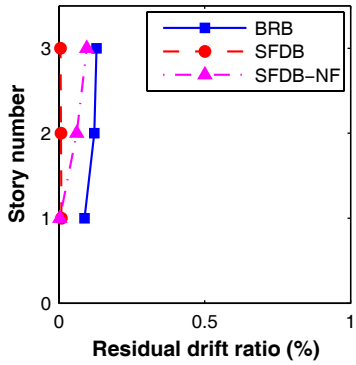

(d) Residual story drift ratio

Figure 5.8 Ensemble average of seismic response of the 3-story prototype building under frequent earthquakes

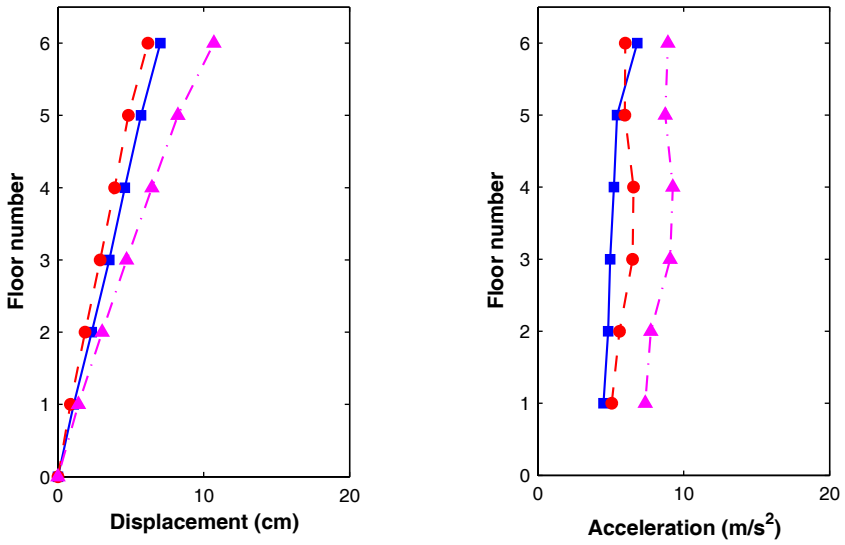

(a) Peak displacement (b) Peak acceleration

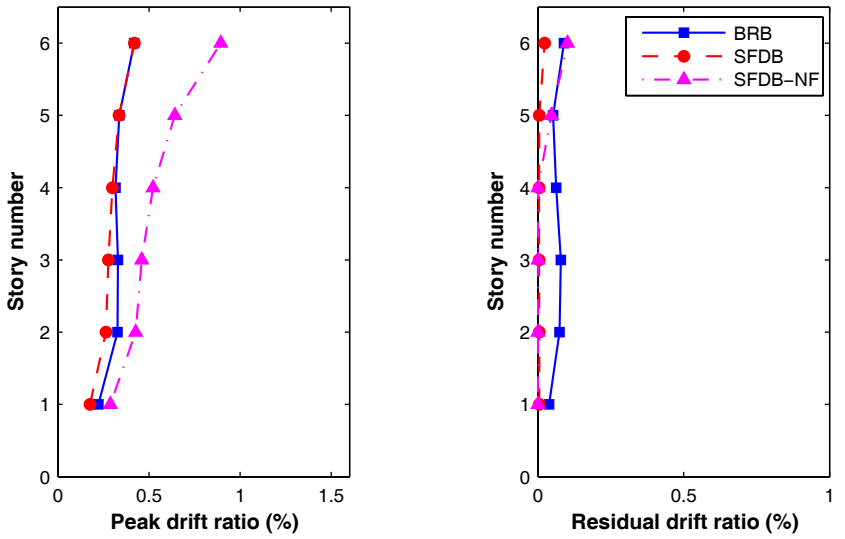

(c) Peak story drift ratio (d) Residual story drift ratio

Figure 5.9 Ensemble average of seismic response of the 6-story prototype building under frequent earthquakes

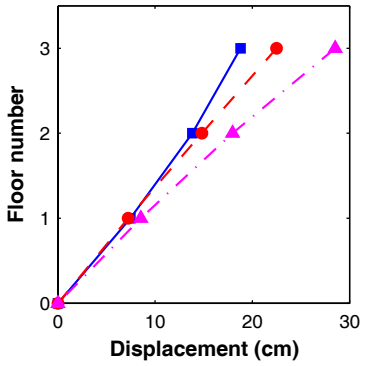

(a) Peak displacement

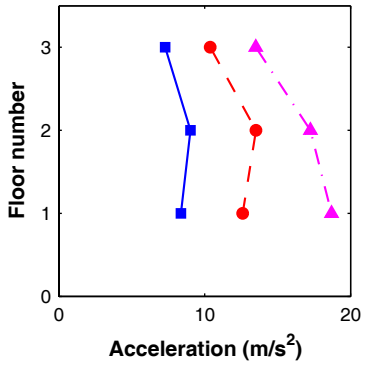

(b) Peak acceleration

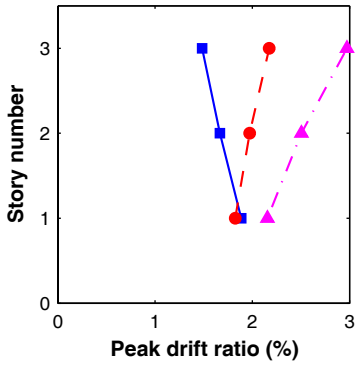

(c) Peak story drift ratio

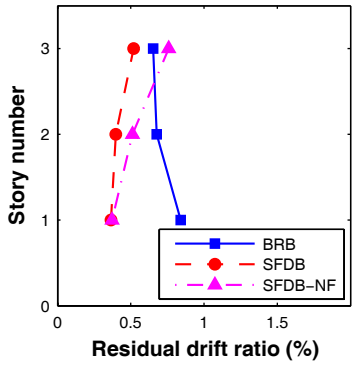

(d) Residual story drift ratio

Figure 5.10 Ensemble average of seismic response of the 3-story prototype building under maximum considered earthquakes

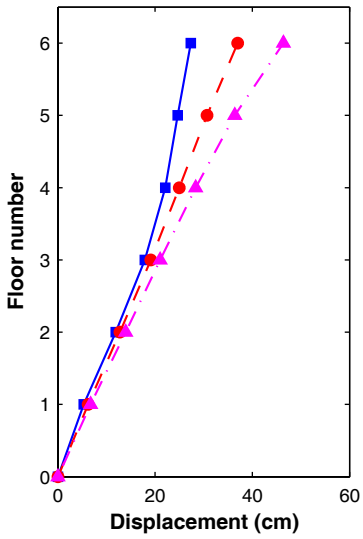

(a) Peak displacement

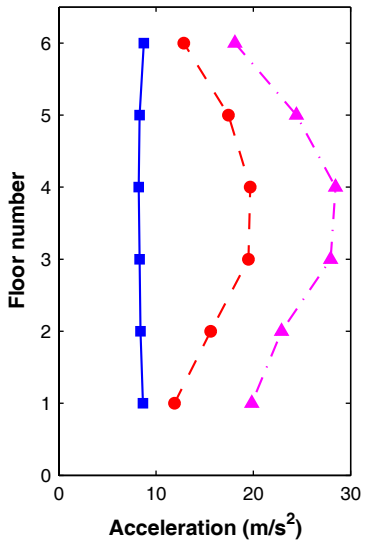

(b) Peak acceleration

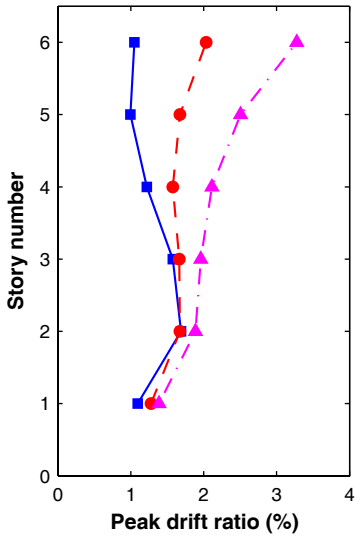

(c) Peak story drift ratio

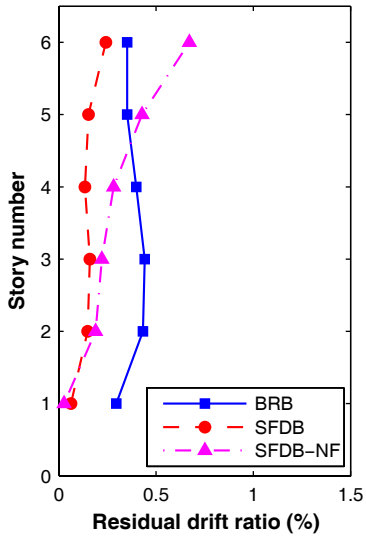

(d) Residual story drift ratio

Figure 5.11 Ensemble average of seismic response of the 6-story prototype building under maximum considered earthquakes

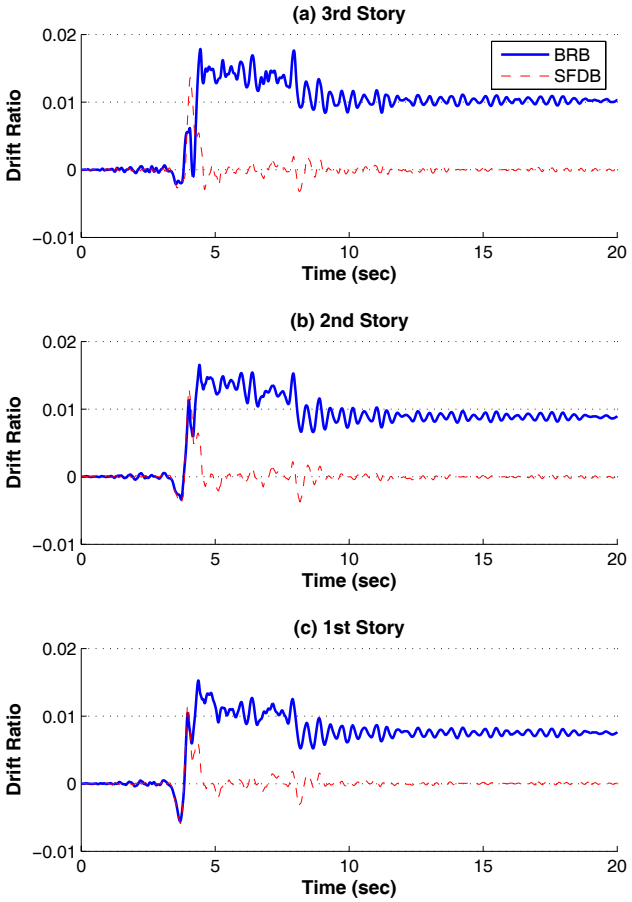

Figure 5.12 Inter-story drift time histories of the 3-story building under earthquake ground motion LA18

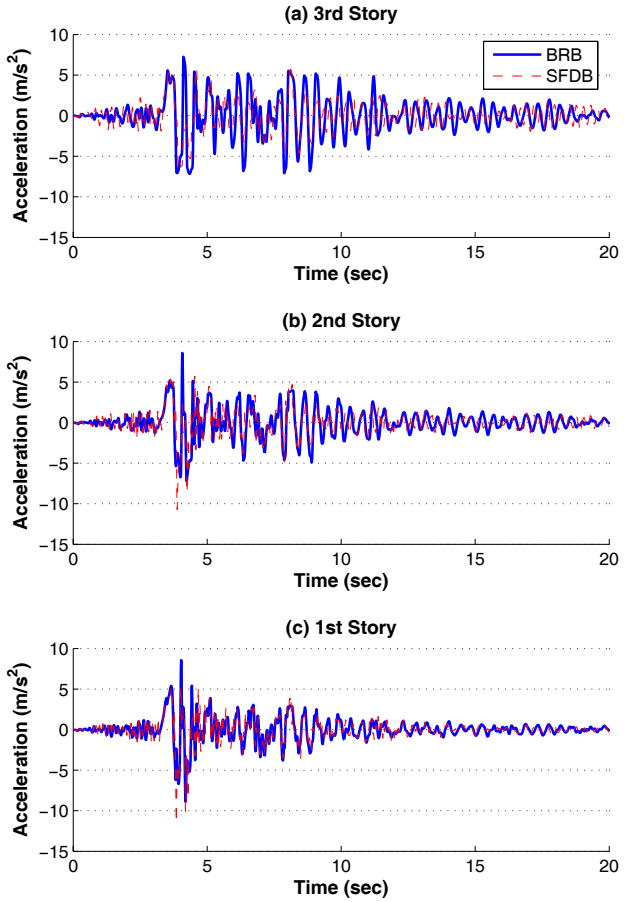

Figure 5.13 Acceleration time histories of the 3-story building under earthquake ground motion LA18

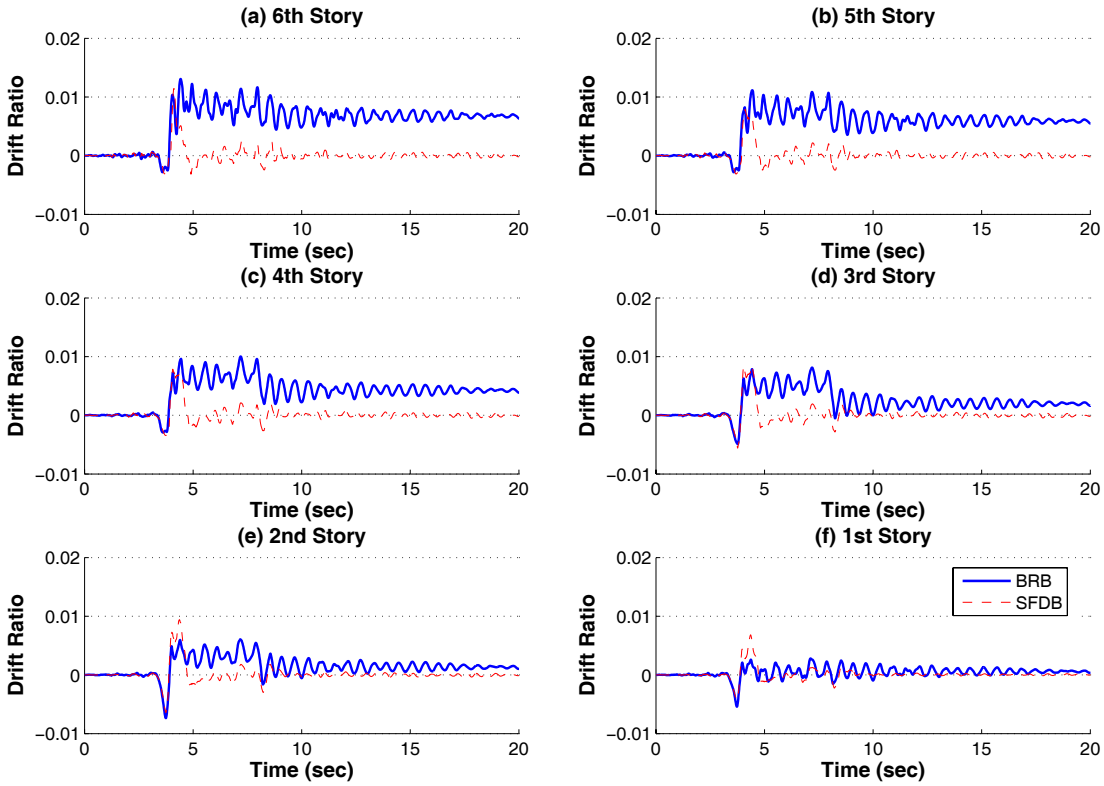

Figure 5.14 Inter-story drift time histories of the 6-story building under earthquake ground motion LA18

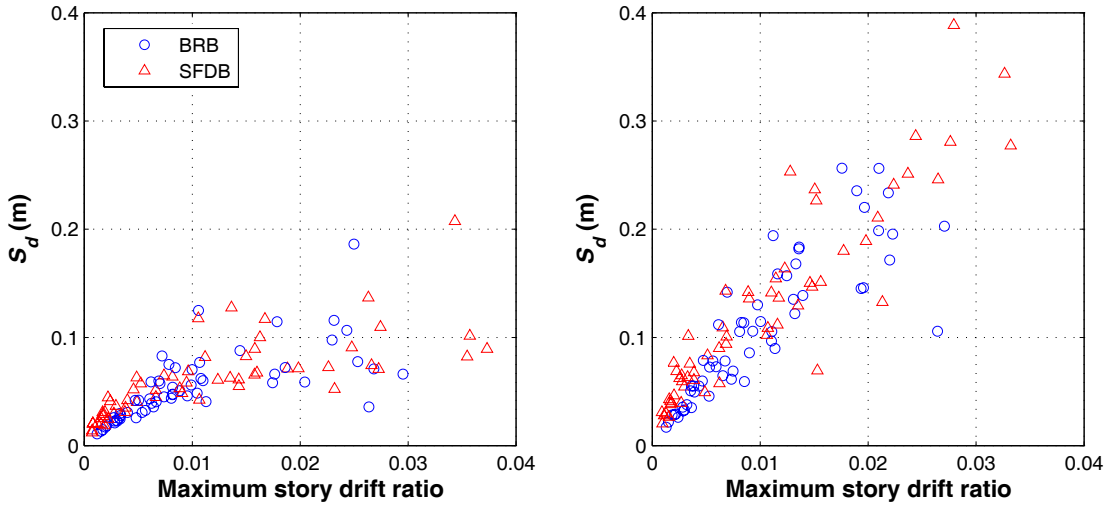

(a) 3-story building (b) 6-story building

Figure 5.15 Scatter plot of spectral displacement vs. maximum drift under FE, DBE and MCE for Los Angeles, California

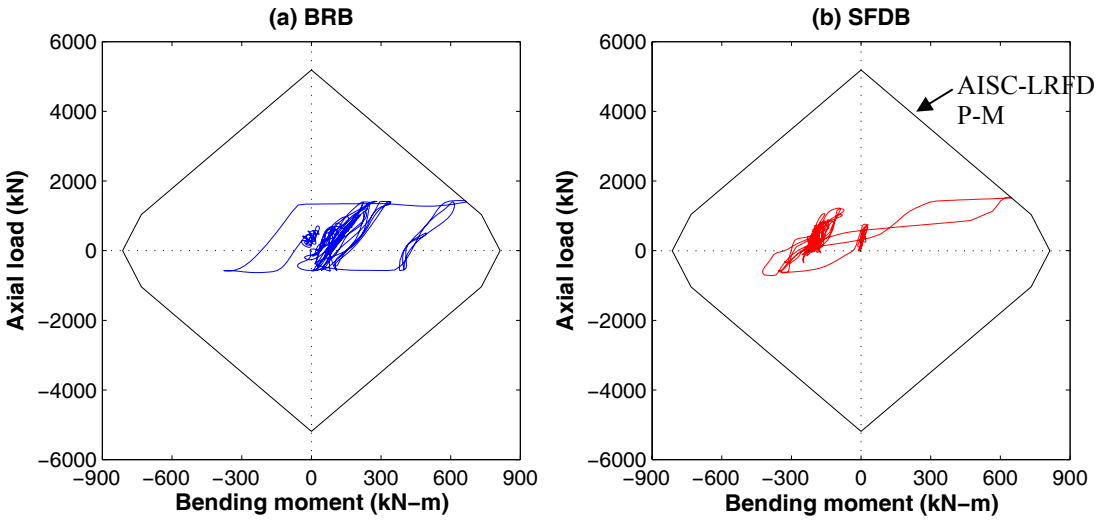

Figure 5.16 Axial load vs. bending moment interaction at column base under earthquake record LA16

CHAPTER 6 DISPLACEMENT-BASED DESIGN PROCEDURE

6.1 INTRODUCTION

Performance-based earthquake engineering (PBEE) has been extensively researched in recent years (Fajar and Krawinkler 1997, 2004). In PBEE, performance objectives are expressed as a set of performance levels such as immediate occupancy, life safety or collapse prevention, associated with earthquake ground motions of specific intensities, as defined in Vision 2000 (SEAOC 1995), FEMA-356 (2000), FEMA-450 (2003) and ATC-58 (2002). Figure 6.1 shows the performance objectives defined in FEMA-450 (2003).

As noted by a number of researchers such as Priestley (2000), conventional force-based seismic design method tends to result in non-uniform risk structures, e.g., two buildings designed to the same code and with the same strength reduction factor may experience distinctive levels of damage under a given earthquake. In some cases, the risk, expressed in terms of the annual probability of occurrence of a given level of damage, can vary by more than an order of magnitude from structure to structure (Priestley 2000). In order to incorporate performance-based criteria into force-based seismic design, significantly increased design effort, which involves the addition of displacement check afterwards and successive iteration of the initial elastic

characteristics, is required (Priestley 2000). Recognizing the deficiencies in the current force-based approaches, a more rational alternative design procedure, displacement-based design (DBD) procedure, has been developed and advocated in the past decade (Priestley 1998, 2000; Calvi and Kingsley, 1995; Kowalsky et al. 1995; Priestley and Kowalsky, 2000; Sullivan et al. 2003; Priestley and Calvi 1997; Fajar 2000; Chopra 2001; Chopra and Goel 2001; Christopoulos and Pampanin 2004). In a direct DBD procedure, the maximum target displacement is a predetermined goal to be achieved under the design-level earthquake, and this design approach would result in an inventory of uniform risk structures, philosophically compatible with the uniform-risk seismic intensity incorporated in most codes (Priestley 2000).

In a self-centering friction braced (SFDB) frame building, its displacement/drift level is not only related to non-structural damage, but also governs the ductility level and response behavior of the SFDBs, the main lateral resisting element in frame structure. For example, at very large displacement the occurrence of slip at friction surface 2 would impair the self-centering capability of the SFDB. Consequently it is very likely to result in residual drift in the braced frame structure and significantly increase the repair cost after earthquakes. For this reason, the drift target in the design of SFDB frames is selected as the performance objective in this study. Considering the inefficiency of the conventional force-based design method in explicit displacement control, the DBD method is adopted here for the seismic design of SFDB frames. It is noted that similar direct DBD procedure has also been used for the design of various structures by other researchers (Kowalsky 2002; Calvi and Kingsley 1995; Kowalski

and Priestley 1996; Priestley 2000; Anderson and Mahin 1997), such as a 3-story CFT/BRB concentrically braced frame by Tsai el al. (2004).

6.2 DESIGN PROCEDURE

While Priestley and his co-workers (Priestley 1998; Priestley and Calvi 1997; Priestley and Kowalsky 2000) proposed a DBD procedure using elastic design spectra for equivalent linear systems, Chopra and Goel (2001) demonstrated that this equivalent linear system, based on the secant stiffness and equivalent damping ratio, may result in inaccurate estimation of seismic deformation and ductility of inelastic structures. Alternatively, inelastic design spectra was proposed for use in DBD procedure, which is shown to produce a structural design that satisfies the design criteria. The DBD approach by Chopra and Goel (2001) using inelastic design spectra is adopted as the basis of the proposed design procedure for SFDB frame in this study, and the flow chart of the DBD approach is shown in Figure 6.2. The details of this DBD procedure for SFDB frame is given as follows..

STEP 1: Design Data

The design parameters of the SFDB frame building under consideration such as the total number of stories n, number of braced bays, seismic mass at each floor level (i.e., m_i), story height (i.e., h_i), need to be specified first. Consequently, a planar MDOF model can be defined for the SFDB frame, as illustrated in Figure 6.3-(b). The design response spectrum should be determined based on the site conditions using the

national seismic hazard maps (NEHRP 2003). A typical pseudo acceleration spectrum (S_{ae}) and displacement spectrum (S_{de}) for SDOF system with 5% damping is shown in Figure 6.4. Figure 6.4-(a) shows the conventional format of response spectrum with respect to period, while Figure 6.4-(b) shows the acceleration-displacement (AD) format as used by Fajar *et al.* (1997). An elastic SDOF system satisfies the following relationship,

$$S_{de} = \frac{T^2}{4\pi^2} S_{ae} \tag{6-1}$$

STEP 2: Set Target Performance Level

The target performance indices that need to be defined for the SFDB frame in this step include the design ductility demand of SFDB (i.e., μ) and design maximum inter-story drift ratio (i.e., θ_d) under the design basis earthquake (DBE). In order to minimize the residual deformation and provide a safety margin, the maximum brace ductility of SFDB has to be limited within a certain range so that the activation of friction surface will not occur. Since the maximum inter-story drift ratio offers an important measure of both the structural and non-structural damage, the limiting values for these two performance indices should be selected to meet the desired performance level.

Once the design inter-story drift is determined, the displacement profile of the multistory frame structure needs to be approximately estimated. For the design examples in this study, only 3-story and 6-story buildings are considered and a linear displacement profiles are assumed to in the design of these two buildings:

$$\Delta_i = \theta_d h_i \tag{6-2}$$

where h_i is the height of story i and Δ_i is the design displacement at floor i (as illustrated in Figure 6.3-(b)). Special caution has to be exercised on this displacement profile. Such a linear displacement profile is usually applicable to the low-rise buildings. Higher buildings generally have a nonlinear displacement profile over height. Therefore, a nonlinear displacement profile suitable to concentrically braced frames should be assumed in the design of medium-rise or high-rise SFDB frames.

Given the design displacement profile and the ductility of SFDB, the length of SMA wires in SFDB can be determined by:

$$l_i = \frac{(\Delta_i - \Delta_{i-1}) \cdot \cos(\alpha)}{\mu \cdot \varepsilon_y} \tag{6-3}$$

where ε_y is the 'yield' strain (i.e., transformation stress) of SMA wires and α is the angle formed by the brace and beams of the braced frame (see Figure 6.3-(a)).

STEP 3: Transform to Equivalent SDOF System

Assuming the seismic response of the frame building is dominated by the fundamental mode, the effective displacement and mass of the equivalent SDOF system is given by

$$\Delta_e = \sum (m_i \Delta_i^2) \Big/ \sum (m_i \Delta_i) \tag{6-4}$$

$$m_e = \sum (m_i \Delta_i) \Big/ \Delta_e \tag{6-5}$$

STEP 4: Calculate Design Base Shear

For a nonlinear SODF system, the acceleration and displacement can be determined as:

$$S_a = \frac{S_{ae}}{R_\mu} \tag{6-6}$$

$$S_d = C_\mu S_{de} \tag{6-7}$$

where R_μ is the strength reduction factor, C_μ is the nonlinear displacement coefficient and μ is the ductility level of SDOF system which is assumed to be equal to the ductility demand of SFDBs. Both factors are functions of ductility μ and initial period T_i, that is,

$$R_\mu = R(\mu, T_0) \tag{6-8}$$

$$C_\mu = C(\mu, T_i) = \frac{\mu}{R(\mu, T_0)} \tag{6-9}$$

The details of R_μ and C_μ will be discussed in the next section. To achieve the target displacement Δ_e, the initial elastic period, the strength reduction factor R_μ and nonlinear displacement coefficient C_μ of the equivalent SDOF system can be determined using nonlinear response spectrum. Given a specified value of the ductility μ of SDOF system, the nonlinear spectrum of the equivalent SDOF system can be constructed for the frequency range of interest using Equations (6-6) to (6-9). With the target displacement Δ_e, the required initial period T_i and the corresponding acceleration S_a are to be determined from the nonlinear response spectrum (as illustrated in Figure 6.5). Here $S_a = S_{de}/R_\mu$ is the acceleration corresponding to the 'yield' strength of the SDOF system, which is used to determine the required design

strength in order to achieve the target performance. Therefore it does not stand for the peak acceleration response during earthquake which is usually larger than S_a due to strain hardening. An alternative approach is to use the elastic displacement spectrum and solve T_i by iteration as illustrated below,

$$S_{de}(T_{0,k}) = \frac{\Delta_e}{C_{\mu,k-1}} \Rightarrow \text{solve}\, T_{0,k} \Rightarrow C_{u,k} = C(\mu, T_{0,k})$$

where k starts from zero until the results converge, and $C_{\mu,0}$ is assumed to be unity.

The design base shear of the equivalent SDOF system is given as,

$$V_b = m_e S_a \tag{6-10}$$

STEP 5: Design Strength of SFDB

The base shear calculated in the last step can be distributed over the braced frame height in proportion to the seismic mass and displacement profile in accordance with the following relationship,

$$F_i = V_b \frac{m_i \Delta_i}{\sum (m_i \Delta_i)} \tag{6-11}$$

Such a force distribution is based on the fundamental mode shape and does not account for the contribution of higher modes. The seismic design story shear in any story is then determined from the equation below,

$$V_i = \sum_{j=i}^{n} F_j \tag{6-12}$$

In the SFDB frame, it is assumed that all design story shear V_i is to be resisted by the concentric braces – SFDBs. Thus the required 'yield' strength of the SFDB, and the cross sectional area of SMA wires in the SFDB can be determined as,

$$A_i = \frac{P_{brc}}{\sigma_y} = \frac{V_i}{2 \cdot \cos\alpha \cdot \sigma_y} \tag{6-13}$$

where σ_y is nominal 'yield' stress (i.e., transformation stress) of SMA wires or actual 'yield' stress determined from material tests.

STEP 6: Design for Other Members in SFDB frame

Since the SFDBs are the primary lateral load resisting and energy dissipating elements of the braced frame building, bracing connections and adjoining members shall be designed to resist the maximum possible brace force. Similar to *Provisions for Buckling-Restrained Braced Frames* (AISC 2005), the adjusted brace strength, $\omega R_y P_{brc}$ is used in the design of bracing connections and adjoining beams and columns. Here the expected yield strength coefficient R_y is the ratio of the expected 'yield' stress to the nominal 'yield' stress of SMA wires, and it needs not to be applied if σ_y is established using experimentally determined 'yield' stress values of SMA wires. The factor ω considers the strain hardening behavior after the 'yielding' of SFDBs, and it is the ratio of the maximum brace force to the yield strength of SFDBs. With the maximum brace force being capped by the slotted bolted connection at the end portion of the SFDB, a strain hardening adjustment factor ω of 2.0 is recommended here.

It should be noted that although no apparent discrepancy was observed in this study between the brace strength in tension and compression, a vertical unbalanced

concentrated force of $0.05\omega R_y P_{bre}\sin(\alpha)$ is still assumed in the design of floor beams. Thus the beam design considers the axial loads caused by adjusted brace strength and the flexural demand resulting from the vertical unbalanced concentrated force, as well as dead and live load. The possible contribution of the concrete slab to the beam stiffness and strength is neglected. Similar to the design of BRB frame (AISC 2005), both pinned beam-column connections and moment-resisting beam-column connections are allowed to be utilized although the braced frame is not explicitly designed to be moment resisting.

STEP 7: Check Performance Level under MCE and FE

The seismic performance levels of the SFDB frame under maximum considered earthquakes (MCE) and frequent earthquakes (FE) need to be checked through inelastic analysis procedures such as pushover analysis or nonlinear time-history analysis. If the performance levels under the MCE and FE are not acceptable, the revision of brace strength, i.e., the cross-sectional area of the SMA wires in SFDBs, would have to be made in order to achieve satisfactory performance level under the MCE and FE. Accordingly, the design of adjoining members and bracing connections also need to be modified.

6.3 SEISMIC RESPONSE OF SDOF SYSTEM

The preceding section refers to a procedure of transforming a multistory braced frame to an equivalent SDOF system. In this procedure, the following assumptions have been made:

(1) A multistory frame responds predominantly in its first vibration mode, and displacement profile during ground shaking can be approximated by the assumed first mode shape.

(2) The seismic-induced story shear forces are mainly resisted by the bracing elements, i.e., the SFDBs in the braced frame, and the contribution to the lateral resistance from other elements is neglected.

(3) As long as the braced frame retains its assumed displacement profile during ground shaking, the braces in different stories would yield simultaneously, and the ductility demands of these SFDBs are assumed to be the same as each other.

Based on the above assumptions, the resulting equivalent SDOF system has a hysteretic shape similar to those of SFDBs but having different parameter values. The displacement response of the multistory frame can be predicted using this equivalent SDOF system and the ductility levels of the SFDBs in multistory frame is assumed to be equal to that of the equivalent SDOF system.

Numerous case studies confirm that the global displacement response of multistory frames, such as roof drift, can be fairly well estimated using the equivalent SDOF system (Shimazaki and Sozen 1985; Qi and Moehle 1991). It is noted, however, that

the maximum inter-story drift ratios could be affected by concentration of inelastic deformation in some stories, higher mode effects and P-Δ effect (Gupta and Krawinkler 2000; Pampanin et al. 2003; Moehle 1992). The ratios of story drift to roof drift over the height of the building has been found to be dependent on structural height, level of inelastic deformation and ground motion characteristics, and they are likely to be larger than 1.0 for most or all stories (Gupta and Krawinkler 2000). In general, the larger the number of stories and/or the larger the maximum story displacement ductility ratio, the larger the ratios of peak story drifts to peak roof drift (Miranda and Reyes 2002). Thus for a relatively high structure, the design procedure using equivalent SDOF system tends to underestimate the value of inter-story drift ratios and therefore the ductility levels of SFDBs.

6.3.1 Nonlinear Response Spectra

Nonlinear response spectra of SDOF system with various hysteretic behaviors have been extensively studied (Chopra 1996; Chopra and Chintanapakdee 2001, 2004; Nassar and Krawinkler 1991; Newmark and Hall 1982; Vidic et al. 1994; Borzi et al. 2001; Miranda 2000, 2001; Miranda and Bertero 1994; Ruiz-Garcia and Miranda 2003; Christopoulos et al. 2002; Farrow and Kurama 2003; Seo and Sause 2005; Seo 2005).

In this study the nonlinear response spectra of SDOF system with flag-shaped hysteresis (representing SFDBs' self-centering hysteretic behavior) were studied. The hysteretic behavior of SFDBs was simulated using the analytical model described in Chapter 4. The analytical model of SFDB utilizes the modified Wilde model for

superelastic Nitinol wires with the consideration of friction forces. The parameters of the modified Wilde model which are tuned based on the dynamic test of Nitinol wires are listed in Table 4.1.

Two different hysteretic behaviors were considered for SDOF system – high damping and low damping to simulate two cases corresponding to SFDB with or without friction effect. The hysteresis representing these two cases respectively is shown in Figure 6.6. The friction force levels at two sliding surface for SFDB and SFDB-NF are described in Chapter 4.

For the above-described two types of hysteresis loops, their 'post-yield' stiffness ratio, the friction force level and the energy dissipation ratio are fixed values that correspond to the SFDB configurations. The viscous damping ratio of the equivalent SDOF system is assumed to be 5% in this study. Thus the dynamic properties of the equivalent SDOF system are defined by two essential parameters — its elastic period T_0 and 'yield' strength F_y, which can be expressed as

$$T_0 = 2\pi \cdot \sqrt{m / k_0} \tag{6-14}$$

$$F_y = \frac{F_e}{R} \tag{6-15}$$

where k_0 is the initial stiffness of the SDOF system, R is the strength reduction facto, F_e is the elastic design strength. With known stress-strain relationship for the superelastic SMA element, the initial elastic stiffness and yield strength can be adjusted by altering its cross-sectional area and wire length. The range of the initial elastic period considered in this study is 0.2 sec $\leq T_0 \leq$ 3.0 sec, typical of one- to 20-story steel braced frames.

It is noted that the stiffness value of SFDB changes before and after SFDB starts to slip over its friction surface. Therefore, the effective initial stiffness of SDOF system with SFDB is defined as the secant stiffness corresponding to the point of 'yield' strength on the load-displacement curve (as shown by the dashed line in Figure 6.6-(b)). Thus with the same 'yield' strength and SMA wire length, the initial stiffness of SFDB and SFDB-NF is identical.

Seo (2005) proposed to use smooth median response as the likely response value for a set of earthquake ground motions based on the assumption that nonlinear response follows a lognormal distribution. The median value is associated with 50% probability of exceedance, and for lognormal distribution the median value of the sampled data can be calculated as the geometric mean (Ang and Tang 1975):

$$\tilde{x} = \exp\left(\frac{1}{n}\sum_{j=1}^{n}\ln x_j\right) \tag{6-16}$$

where x_j, j = 1,2, …, n represent the sampled data. It was defined by Seo (2005) as the smooth median, denoted by "~", in order to differentiate it from the counted median (MED):

$$MED(x) = \begin{cases} x_{(n+1)/2} & n = \text{odd number} \\ (x_{n/2} + x_{n/2+1} & n = \text{even number} \end{cases} \tag{6-17}$$

The findings by Seo (2005) indicate that: (1) the smooth median nonlinear response spectra for systems with their yield strength determined from the smooth median pseudo acceleration spectrum for a set of ground motions are similar to the smooth median response spectra for systems with the yield strength determined from the pseudo acceleration spectrum for the individual ground motions in the ground

motion set; (2) There exists a simple and direct relationship between the smooth median nonlinear spectral responses for a system with a constant μ and the smooth median nonlinear spectral responses for a system with a constant R.

Therefore the smooth median nonlinear response spectra were used in this study to investigate the SDOF system with hysteretic behaviors shown in Figure 6.6. Constant R method was used and the values of the strength reduction factor R considered in this study were 2, 3, 4, 5, 6, 7 and 8 respectively.

The ground motions developed by Somerville et al. (1997) were employed in the time history analyses. Only the suite corresponding to DBE level was selected in this section and it contains 20 records designated as LA01 - LA20 respectively. More details about these ground motion sets can be found in Appendix A. Figure 6.7 shows the 5%-damped elastic response spectra of considered ground motions, as well as the design spectrum corresponding to site class D (firm soil) in Los Angeles (zip code 90019). The smooth median elastic acceleration spectrum, along with the Equation (6-6), is used to determine the 'yield' strength of SDOF system in this study. It is seen that the smooth median acceleration response spectrum of 20 records is in reasonable agreement with the design response spectrum given by NEHRP code (2003). The profiles of the maximum and minimum response spectra are also shown in Figure 6.7.

The nonlinear response of the SDOF systems with two types of hysteresis loops were studied for varying parameters R and T_0 under a suite of twenty ground motions. Figure 6.8 and Figure 6.9 show the smooth median constant-R spectra of ductility level and nonlinear displacement coefficient, which are denoted as $\widetilde{\mu}_R$ and $\widetilde{C}_R$ respectively. With the same strength reduction factor, R, i.e., the same yield strength,

F_y, the SDOF system with the SFDB-type hysteresis always leads to smaller $\widetilde{\mu}_R$ and $\widetilde{C}_R$ than that of SFDB-NF. This improved control effect on the displacement and less demand on brace ductility is due to the enhanced energy dissipation in SFDB through friction force which increases the damping ratio of the SDOF system, especially for small values of R. For example, when $R = 2$, $\widetilde{C}_R$ of SFDB system is less than 1 for the period range considered in this study, i.e. 0.2 sec $\leq T_0 \leq$ 3.0 sec, implying that the peak nonlinear displacement is smaller than that of an elastic SDOF system with 5% critical damping ratio.

6.3.2 Regression Analyses

The regression analyses were carried out on the $\widetilde{\mu}_R$ spectra to establish a mathematical function for use in the design procedure. The regression result, denoted as $\hat{\mu}_R$, is usually a function of T_0 and R. The following expression of the regression function was proposed by Seo (2005) for four different hysteresis models:

$$\hat{\mu}_R = R^{\exp(c1/T_0^{c2})} \tag{6-18}$$

This function is also used in this study to estimate the $\widetilde{\mu}_R$ spectra of the SDOF system with SFDB-NF-type hysteresis. For the SDOF system with SFDB-type hysteresis it is slightly modified as follows:

$$\hat{\mu}_R = R^{\exp(c_1/T_0^{c2})} - c_3 \tag{6-19}$$

For SFDB-NF-type SDOF system, Equation (6-18) can be rewritten as,

$$\ln\left(\ln\left(\frac{\ln\hat{\mu}_R}{\ln R}\right)\right) = \ln c_1 - c_2 \ln T_0 \tag{6-20}$$

Therefore the coefficient c_1 and c_2 can be obtained through linear regression such as the least square method. Figure 6.10-(a) shows the data points $\left(\ln\left(\ln\left(\frac{\ln\tilde{\mu}_R}{\ln R}\right)\right), \ln T_0\right)$ and linear equation of regression results. Based on this data set, c_1 and c_2 can be calculated as

$$c_1 = \exp(-1.8) = 0.1653, \qquad c_2 = 0.83$$

The regression function $\hat{\mu}_R$ for the SFDB-NF-type SDOF system becomes

$$\hat{\mu}_R = R^{\exp(0.1653/T_0^{0.83})} \tag{6-21}$$

For SFDB-type SDOF system, Equation (6-19) satisfies the following relationship:

$$T_0 \to \infty, \qquad \hat{\mu}_R = R - c_3$$

Therefore the coefficient c_3 in Equation (6-19) can be evaluated using the $\tilde{\mu}_R - R$ relationship at long period (T_0 > 3 sec). A procedure similar to that for the SFDB-NF system was followed to determine the values of coefficient c_1 and c_2 (as shown in Figure 6.10-(b)). The regression values of the coefficients and regression function for the SFDB-type SDOF system are expressed as follows:

$$c_1 = \exp(-2.0) = 0.1353, \qquad c_2 = 0.8, \qquad c_2 = 0.75$$

$$\hat{\mu}_R = R^{\exp(0.1353/T_0^{0.8})} - 0.75 \tag{6-22}$$

Seo (2005) indicated that the regression function $\hat{\mu}_R$ for the smooth-median constant-R response spectrum $\tilde{\mu}_R$ can be inverted without knowledge of the dispersion to estimate corresponding $\tilde{R}_\mu$ spectrum—smooth-median constant-μ

spectrum which expresses R as a function of T_0 and μ. The resulting function is denoted as $\hat{R}_\mu$. Functions $\hat{\mu}_R$ and $\hat{R}_\mu$ can also be used to develop functions to estimate the smooth-median spectrum of nonlinear displacement coefficients, $\widetilde{C}_R$ and $\widetilde{C}_\mu$ respectively. The resulting functions for the SFDB-NF system and SFDB system are listed as follows:

For SFDB-NF-type SDOF system:

$$\hat{R}_\mu = \mu^{\exp(-0.1653/T_0^{0.83})} \tag{6-23}$$

$$\hat{C}_\mu = \mu / \hat{R}_\mu = \mu^{1-\exp(-0.1653/T_0^{0.83})} \tag{6-24}$$

$$\hat{C}_R = \hat{\mu}_R / R = R^{\exp(0.1653/T_0^{0.83})-1} \tag{6-25}$$

For SFDB-type SDOF system:

$$\hat{R}_\mu = (\mu + 0.75)^{\exp(-0.1353/T_0^{0.8})} \tag{6-26}$$

$$\hat{C}_\mu = \mu / \hat{R}_\mu = \mu /(\mu + 0.75)^{\exp(-0.1353/T_0^{0.8})} \tag{6-27}$$

$$\hat{C}_R = \hat{\mu}_R / R = (R^{\exp(0.1653/T_0^{0.83})} - 0.75) / R \tag{6-28}$$

Figure 6.11 show the comparison between the regression function $\hat{\mu}_R$ and smooth-median response spectrum, $\widetilde{\mu}_R$. In general, the $\hat{\mu}_R$ function matches well with the $\widetilde{\mu}_R$ data over the period range for the strength reduction factor values considered and the two hysteresis models. Figure 6.12 shows the regression function $\hat{C}_R$ and smooth-median response spectrum $\widetilde{C}_R$ for both hysteresis models. It can be seen that function $\hat{C}_R$ can fairly well estimate the values of $\widetilde{C}_R$.

Figure 6.13 and Figure 6.14 show the values of functions $\hat{R}_\mu$ and $\widetilde{C}_\mu$ respectively over the period range considered for the two hysteresis models. It is noted again that these functions $\hat{R}_\mu$ and $\widetilde{C}_\mu$ are used in the STEP 4 of the proposed design procedure for SFDB frame in the preceding section. It can be seen from these figures that the SFDB system results in relatively larger strength reduction factors and smaller nonlinear displacement coefficient compared to the SFDB-NF system.

6.4 DESIGN EXAMPLES

Two design examples for SFDB frames are presented in this section. The nonlinear static analyses (i.e., pushover analyses) and nonlinear time history analyses of the designed SFDB frame are carried out to evaluate the effectiveness of the proposed design procedure.

6.4.1 Design examples

A 3-story and a 6-story office building are designed using the above-mentioned design procedure. The details about these two frame buildings are described in Appendix B. Figure B.1 and Figure B.2 show the plan and elevation view of these 3-story and 6-story buildings, as well as the story height and location of the bracing elements in SFDB frames. These two steel braced frame buildings are designed for a location in downtown Los Angeles (zip code: 90019) with site class D (firm soil). Accordingly the design spectrum given in Figure 6.7 can be used in the design. For the 3-story

building, the seismic mass is 8.73×10^5 kg for the 1st and 2nd floor, 7.88×10^5 kg for the 3rd floor; while for the 6-story building, the seismic mass is 9.06×10^5 kg for the 1st through 5th floor, and 8.19×10^5 kg for the 6th floor. The design drift ratio is specified as 1% under the DBE earthquake for both the 3-story and 6-story buildings, and the design ductility levels of SFDBs/SFDB-NFs are assumed to be equal to 4. In comparison with the ductility of SFDBs/SFDB-NFs corresponding to the slip of friction surface 2 (i.e. μ = 8.0), such a target ductility performance would lead to minimal residual displacements of frames after DBE earthquakes. The details of the design example of the 6-story SFDB frame are shown as follows.

Structural Data	Location: Los Angeles, zip code: 90019	
	Design acceleration parameters: S_{DS} = 1.212, S_{D1} = 0.656	
	Design spectrum: as shown in Figure 6.7	
	6 stories, 6 bays of CBF	
	Story height: h_i = 4.88, 3.96, 3.96, 3.96, 3.96, 3.96 (m)	
	Seismic floor mass (1st~6th): 906, 906, 906, 906, 906, 819 (ton)	
	Frame tributary mass: m_i = 151, 151, 151, 151, 151, 136 (ton)	
Target Performance Level	Under DBE level	Inter-story drift: θ_d = 1.0%
		Ductility level: μ = 4.0
	Under FE	No significant structural yielding or residual strain
	Under MCE	Roof drift < 3%, inter-story drift < 4%
Equivalent SDOF System	Displacement profile: Δ_i = 0.048, 0.088, 0.13, 0.17, 0.21, 0.25 (m)	
	SMA wire length: l_i = 0.83, 0.75, 0.75, 0.75, 0.75, 0.75 (m)	
	Effective displacement: Δ_e = 0.177 (m)	
	Effective mass: m_e = 737 (ton)	

Design Base Shear

Iteration:

$C_\mu = 1.000 \rightarrow S_{de} = \Delta_e / C_\mu = 0.177$ m $\rightarrow T_0 = 1.087$ s

$C_\mu = 1.013 \rightarrow S_{de} = \Delta_e / C_\mu = 0.175$ m $\rightarrow T_0 = 1.075$ s

$C_\mu = 1.015 \rightarrow S_{de} = \Delta_e / C_\mu = 0.174$ m $\rightarrow T_0 = 1.068$ s

Thus, $T_0 = 1.068$ s,

$\mu = 4.0$, $R = 3.94$, $C_\mu = 1.016$, $S_{ae} = 0.614$ g

$V_b = m_e \cdot S_{ae}/\mathrm{R} = 1125$ kN

Strength of SFDBs

Lateral force: $F_i = 64, 115, 167, 218, 270, 291$ (kN)

Story shear force: $V_i = 1125, 1061, 946, 779, 561, 291$ (kN)

cross sectional area: $A_i = 15.1, 12.9, 11.5, 9.5, 6.8, 3.5$ (cm^2)

Design of Beams and Columns

Adjusted brace strength:

$P_{max,i} =$ 1645, 1404, 1251, 1031, 742, 385 (kN)

1.4D + 0.5L + 2.0QE

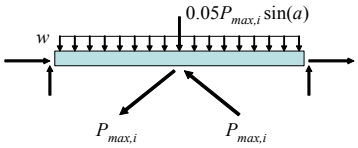

Beams:

1st to 3rd floor: W12x87

4th to 6th floor: W12x65

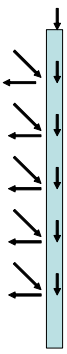

Columns:

1st to 3rd floor: W14x211

4th to 6th floor: W14x132

The design of other SFDB frame buildings follows a similar procedure. Table 6.1 presents the properties of the SFDB braces, including the 'yield' strength, cross-sectional area and length of the SMA wires (Nitinol is used here), in the four designed frame buildings. The friction forces at the two respective sliding surfaces are as specified before. Figure 6.15 shows the section sizes of the beams and columns in the four frames respectively. Steel A992 Grade 50 is assumed to be used for all beams and columns. All the beam-column connections in the braced bays are detailed with moment-resisting connection.

As shown in Table 6.1, the design of SFDB frame tends to yield smaller yield strength of braces than SFDB-NF frame. For example, the brace strength of the SFDB frame is 80% that of the SFDB-NF frame in the 3-story building, and only 64% for the 6-story building. This consequently results in smaller section sizes of beams and columns in the SFDB frames the design of which is governed by the adjust brace strength (as shown in Figure 6.15). The volume of Nitinol wires, which are relative expensive materials, used in SFDB frame is only 58% that in SFDB-frame for the 3-story building, and only 46% for the 6-story building. In comparison with SFDB-NF frame, the design of SFDB frames can significantly save the building cost and leads to a relative economical design. This is due to the enhanced energy dissipation and contribution of brace strength offered by the friction force in SFDBs.

Table 6.2 presents the fundamental periods of the four designed frame buildings. The estimate in the design procedure is seen to be in a good agreement with the actual fundamental elastic periods of the designed buildings. It can also be seen that the designed SFDB-NF frame building tends to have shorter periods, or larger stiffness, in

order to achieve the same level of target displacement, as compared to the SFDB frame building.

6.4.2 Pushover Analyses

Nonlinear pushover analyses were conducted to evaluate the lateral load response and failure mechanisms of the SFDB frames and SFDB-NF frames. *NEHRP Recommended Provisions* (FEMA 2003) was followed to determine the lateral load distribution. Figure 6.16 and Figure 6.17 show the pushover curves (base shear versus roof drift ratio) for the four designed frames—3-story SFDB frame, 3-story SFDB-NF frame, 6-story SFDB frame and 6-story SFDB-NF frame respectively. Various characteristic points such as the slip at friction surface of SFDB, 'yielding' of SFDB/SFDB-NF braces, yielding at beams and columns, are indicated in Figure 6.16 and Figure 6.17.

The base shear of SFDB-NF, for both 3- and 6- story buildings, is much larger than the corresponding value of the SFDB frame, as a result of larger design strength of the SFDB-NF braces. This larger base shear has to be taken into account in the design of building foundations. Initial stiffness change in the SFDB frame can be observed from its pushover curve shown in Figure 6.16-(a) and Figure 6.17-(a). The friction surfaces in the SFDBs begin to slip at very small roof displacement. Before and after the slip, the stiffness of the SFDB frame would change.

Both the SFDB and SFDB-NF frames yield at relatively small roof drift ratios (about 0.25%). The yield strength of SFDB or SFDB-NF frames is very close to the

design base shear, which indicates that the lateral forces are mainly resisted by the SFDBs in the braced frames and the contribution to the lateral resistance from other structural members is relatively small. The 'yield'-like plateau of SFDB or SFDB-NF frames is caused by the solid phase transformation in superelastic SMA wires instead of plastic deformation. Before the occurrence of plastic deformation in beams and columns, there is essentially no damage in the SFDB frame. Therefore the SFDB frame has the potential to achieve a damage-free structural system for frequent earthquakes and design basis earthquakes, which would lead to considerably reduced repair cost and service interruption after design-level earthquakes, particularly in seismic active regions.

The slip of friction surface 2 in SFDBs or SFDB-NFs occurs at a roof drift ratio around 2%. The strain hardening and plastic deformation associated with the superelastic Nitinol wire in excess of 8% strain would cause certain undesirable effects in the SFDB frame if the sliding surface 2 is not activated at this point. Below this roof drift ratio value, the SFDBs or SFDB-NFs in the frames do not have appreciable residual deformation after earthquakes and thus need not be repaired. However, above this roof drift ratio value the SFDBs or SFDB-NFs lose their self-centering capacity and residual deformation will occur. The corresponding pushover curves with unloading path (in dashed line) are also shown in Figure 6.16 and Figure 6.17, and apparent residual roof drift ratio after unloading can be observed. The relatively small residual drift ratio of the SFDB-NF frame after unloading is mainly due to its larger brace strength.

6.4.3 Nonlinear Time History Analyses

Three suites of earthquake ground motions developed by Somerville et al. (1997) are used in the nonlinear time history analyses in this study. In addition to the DBE level earthquakes considered in the previous nonlinear analyses of SDOF system, the earthquake suites with 50% and 2% probability of exceedance respectively in a 50-year period are also selected here for evaluating the seismic performance of the designed frame buildings under FE and MCE level earthquakes. Each suite of ground motions contains 20 records designated as LA01 - LA20 (for DBE), LA21 – LA40 (for MCE) and LA41 - LA60 (for FE), respectively. More details about these three ground motions can be found in Appendix A.

Figure 6.18 and Figure 6.19 show the smooth-median response of the 3- and 6-story building respectively under the DBE earthquakes. The smooth-median response is calculated based on the time history analysis results under 20 ground motions in the DBE suite. The peak floor displacement is normalized by the building height. It can be seen that the displacement profiles from the nonlinear time history analyses match well with the design displacement for all four braced frames. Clearly the SFDB or SFDB-NF frame buildings designed using the proposed DBD approach can achieve the target displacement pattern specified in the design procedure. In terms of the peak inter-story drift ratios and ductility levels of the SFDB braces, the 3-story building, including both the SFDB and SFDB-NF frames, can meet the design target performance reasonably well. For the 6-story buildings, the proposed DBD method tends to underestimate the peak inter-story drift ratios and brace ductility demands for

both the SFDB and SFDB-NF frames. Particularly, for the 6-story SFDB-NF frame, apparent non-uniform distribution of inter-story drift ratios and brace ductility demands can be observed along the building height, and smooth-median results from the time history analyses are seen to exceed the design estimation by up to 60%.

In the DBD procedure, the seismic response of a multi-story frame is assumed to be dominated by its fundamental vibration mode. As mentioned earlier, although its displacement response can be estimated with satisfactory accuracy from the equivalent SDOF system, other response quantities including maximum inter-story drift ratios may be affected by higher mode effects, concentration of inelastic deformation and P-Δ effect (Gupta and Krawinkler 2000; Pampanin et al. 2003, Moehle 1992). Therefore the proposed DBD procedure may underestimate the inter-story drift ratios for these cases and consequently the ductility levels of the SFDB braces. Compared to the 3-story building, the concentration of inter-story drift due to inelastic behavior and the effect of higher mode participation is more prevalent in the 6-story building, and as such the discrepancy between the design value and analysis results is more obvious.

Figure 6.20 and Figure 6.21 show the displacement response and inter-story drift ratios of the 3- and 6-story building under FE earthquakes respectively. The smooth median values of both peak and residual response are presented. The peak roof drift ratios are less than 0.5% for all four buildings. No significant structural damage occurs at such a small value of roof drift ratio (as shown in Figure 6.16 and Figure 6.17). The residual displacement and inter-story drift ratio is observed to be minimal for all four buildings. Therefore the design of all four frames satisfies the performance requirement under the FE earthquake. It is also seen that under the FE earthquakes the

peak displacement and inter-story drift ratio of the SFDB frame is less than those of the SFDB-NF frame, although their performance under the DBE earthquakes is very close to each other. This can be explained by the fact that under small amplitude vibration SFDB-NFs are mainly in elastic range and the energy dissipation is very small. However, the friction force in SFDBs can effectively dissipate the energy even under small amplitude vibration.

Figure 6.22 and Figure 6.23 show the smooth-median response of displacement and inter-story drift ratio under the MCE earthquakes. For all four designed frames, the peak roof drift ratio is less than 3% and the maximum inter-story drift ratio is less than 4%. Therefore the designed frames also satisfy the target performance specified for the MCE level. The performance levels of the four buildings under the MCE earthquakes are close to each other. Once the peak roof drift ratios exceed 2%, the friction surface 2 in SFDBs or SFDB-NFs will slip. Consequently residual displacement or story drift can be observed in all four frames in these cases. The maximum residual drift ratios of the SFDB frames are slightly larger than those of the SFDB-NF frames. This is consistent with the observations from the pushover analyses.

Figure 6.24 and Figure 6.25 show the smooth-median response of floor acceleration for both SFDB and SFDB-NF frames under three different seismic intensities—FE, DBE and MCE levels. For both 3-story and 6-story buildings, the SFDB frames have smaller acceleration demands than the SFDB-NF frames under all three seismic intensity levels due to the lower brace strength used in the design of SFDB frame. The peak smooth-median accelerations under MCE earthquakes are 1.1 g and 1.6 g respectively for 3-story SFDB and SFDB-NF frames, and are 1.4 g and 2.1

g respectively for 6-story SFDB and SFDB-NF frames. Cautions need to be exercised on the high acceleration demands observed in SFDB-NF frames which may cause undesirable damage to acceleration sensitive building contents and components.

Figure 6.26 to Figure 6.28 show the scatter plots of roof drift ratios, peak inter-story drift ratios and residual inter-story drift ratios for these buildings with different hazard levels. The peak and residual inter-story drift ratios are the maximum values in all stories. Additionaly, the smooth median and smooth median plus standard deviation is plotted in these figures.

6.5 CONCLUSIONS

This chapter presents a displacement-based procedure for the seismic design of steel concentrically braced frame (CBF) buildings with a special bracing element termed self-centering friction damping brace (SFDB). Through an equivalent SDOF system, the displacement-based design (DBD) procedure proportions SFDB frame based on the target performance level under design basis earthquakes, such as target building displacement and target ductility level of braces.

The proposed DBD method was applied to the design of a 3-story and 6-story building located in Los Angeles, California, respectively. The design examples of CBF buildings with self-centering braces without friction, denoted as SFDB-NF, are also included as reference cases in this chapter in order to evaluate the effect of friction force in SFDB. The design examples demonstrate that owing to the

contribution of friction force in SFDBs, SFDB frames are believed to yield more economical design than the SFDB-NF frames.

Nonlinear pushover and dynamic analyses of the prototype concentrically braced frame (CBF) buildings were performed to evaluate the effectiveness of the proposed design method. The time history analyses involve three suites of earthquake ground motions each containing 20 earthquake records which represent the frequent, design basis and maximum considered earthquakes in Los Angeles, California respectively. The results indicate that SFDB frames designed using the DBD procedure can often achieve their target displacement parameters with a high degree of accuracy. However, caution should be exercised on design of medium-rise buildings since the proposed DBD method tends to give underestimated values of maximum story drift ratios and brace ductility demands which can be attributed to the exclusion of concentration of story drift due to inelastic behavior and higher mode contribution in this simplified design method. Their effects generally increase with the displacement ductility ratio and the number of stories. Future work is expected to refine this design method by including these effects in the total response of medium or high-rise buildings.

The results of both the nonlinear time history and pushover analyses show that through proper selection of target performance levels, SFDBs has a potential to establish a new type of CBF systems with self-centering capability that can withstand several frequent or design basis earthquakes without the need for replacement.

Although the DBD procedure presented in this chapter for SFDB frames shows promise, further works need to be done in the future to address its limitations as follows: the nonlinear response spectrum is based on the ground motion set for site

class D in downtown Los Angeles. Previous work by other researchers suggests that nonlinear response spectrum is dependent on the characteristics of ground motions, such as locations, site soil conditions, earthquake magnitudes and site distances. Therefore additional work is required to extend the regression results of μ-R given in this chapter to different design cases. It is also noted that the near-field effect of earthquakes were not considered in this study.

Additionally, the probability of exceedence needs to be considered in the determination of target performance level. In current method the target performance levels are specified for the smooth median response under earthquakes. However, the failure probability or the probability of exceeding a threshold of response in the life time of structures rather than the median response is more interested in the structural design or the evaluation of structural performance. Thus probabilistic distributions of seismic responses of SFDB frames need to be studied in the future and the design criteria should be based on target performance levels with a certain reliability confidence. Furthermore, only two levels of friction forces were considered in this study. To make the design of SFDB frame more general, additional friction force levels should be considered in future design.

Table 6.1 Properties of the braces used in the designed frame

Building model	Story #	Yield strength (kN)	Cross sectional area* (cm^2)	Wire length (m)
3-story	3	587	10.8	0.75
SFDB frame	2	1021	18.7	0.75
	1	1237	22.7	0.75
3-story	3	736	18.7	0.75
SFDB-NF frame	2	1280	32.4	0.75
	1	1552	39.3	0.75
6-story	6	193	3.5	0.75
SFDB frame	5	371	6.8	0.75
	4	515	9.5	0.75
	3	626	11.5	0.75
	2	702	12.9	0.75
	1	823	15.1	0.83
6-story	6	300	7.6	0.75
SFDB-NF frame	5	578	14.6	0.75
	4	803	20.3	0.75
	3	975	24.7	0.75
	2	1094	27.7	0.75
	1	1282	32.5	0.83

* The cross sectional area of Nitinol wires is only for one side.

Table 6.2 Elastic fundamental periods of designed frames

	Elastic period (sec)	
	Design estimation	Actual value
3-story SFDB frame	0.51	0.56
3-story SFDB-NF frame	0.46	0.48
6-story SFDB frame	1.07	1.15
6-story SFDB-NF frame	0.86	0.93

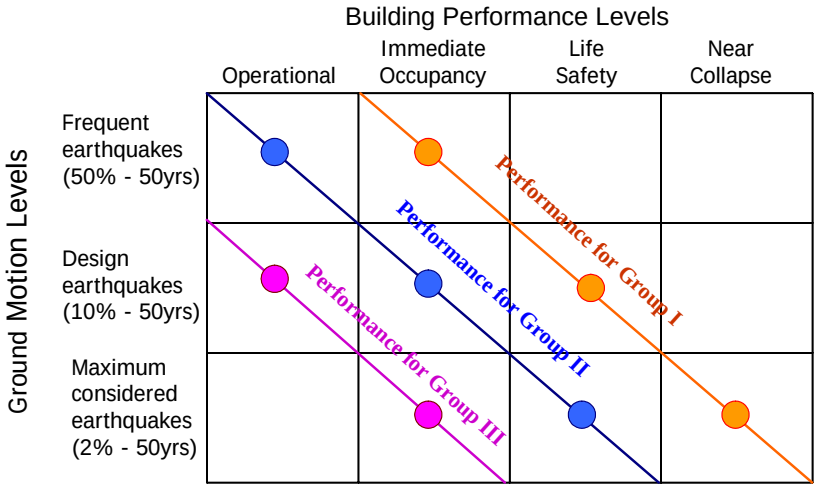

Figure 6.1 Performance objectives in FEMA-450

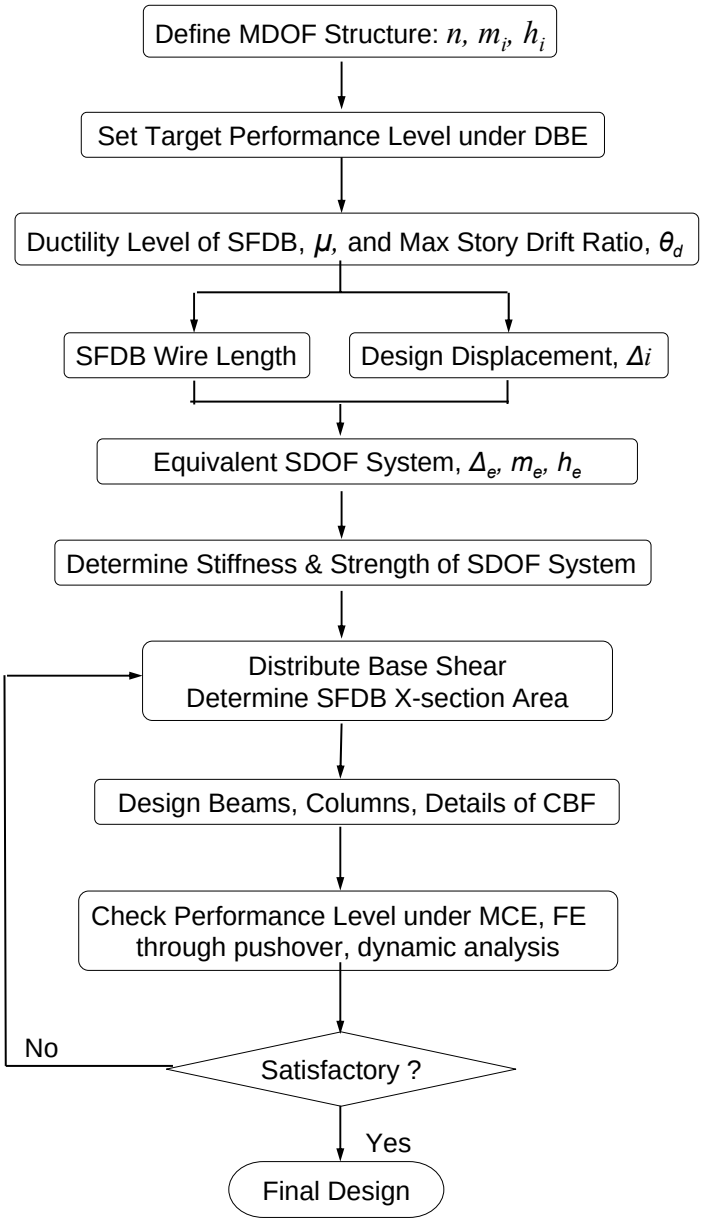

Figure 6.2 Flow chart for the proposed design procedure

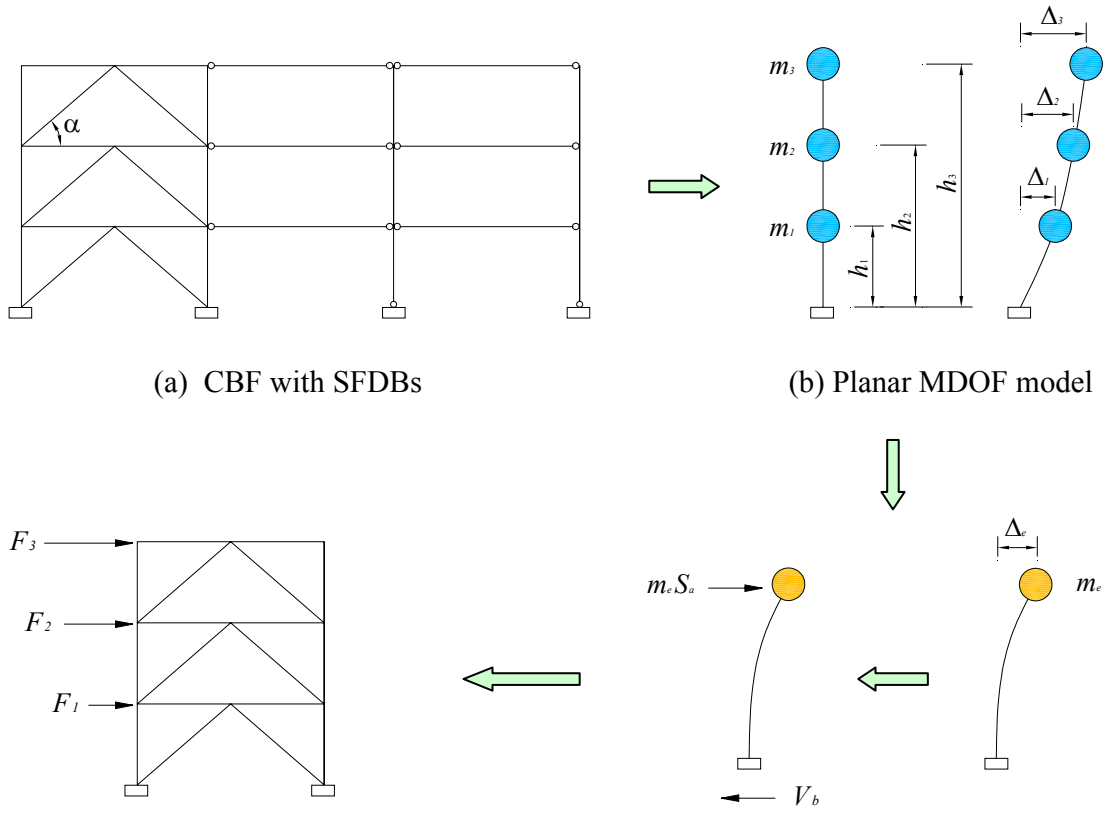

(a) CBF with SFDBs

(b) Planar MDOF model

(d) Distribution of design base shear

(c) Equivalent SDOF system

Figure 6.3 Schematic diagram of displacement-based seismic design procedure

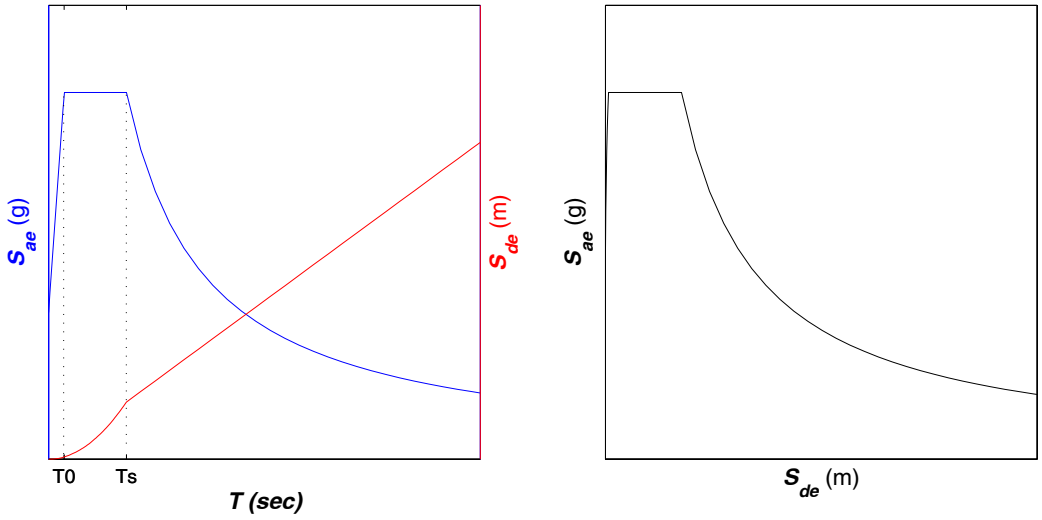

(a) Conventional format (b) AD format

Figure 6.4 Typical elastic design response spectrum for 5% damping

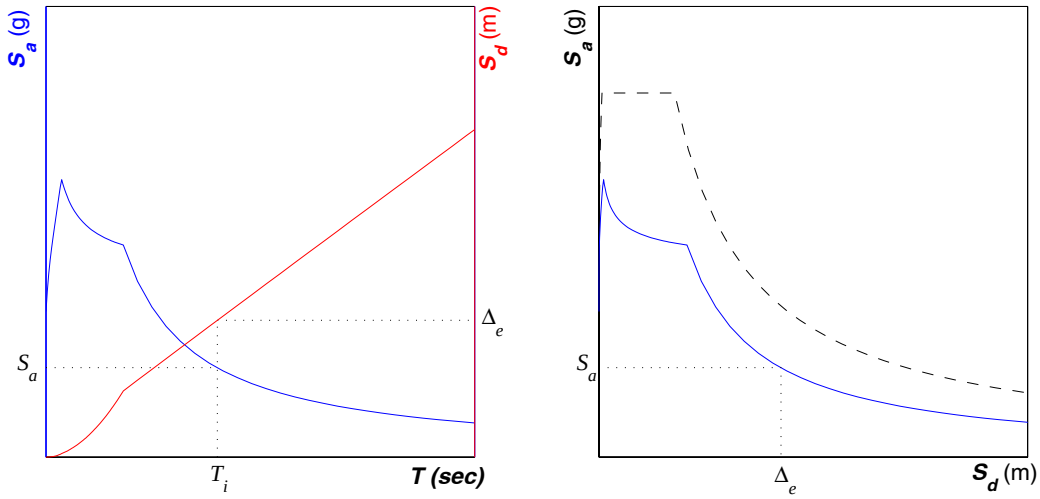

(a) Conventional format (b) AD format

Figure 6.5 Nonlinear response spectrum for SDOF system

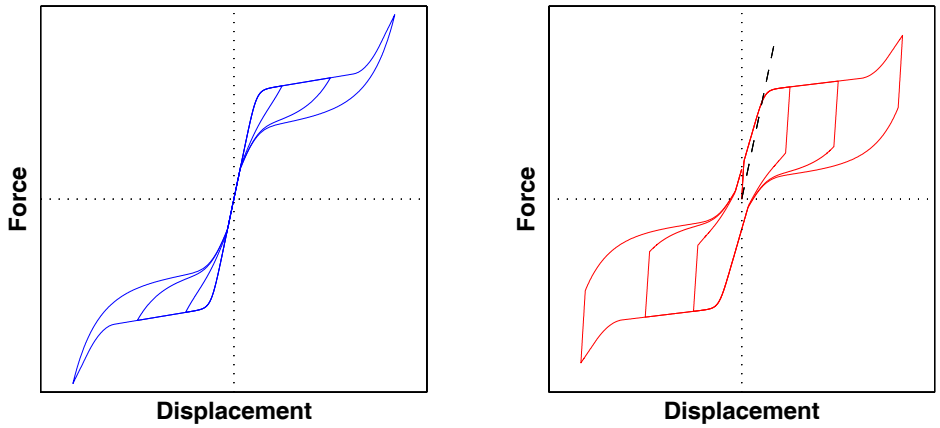

(a) SFDB-NF (b) SFDB

Figure 6.6 Two typical hysteretic behaviors for SDOF system

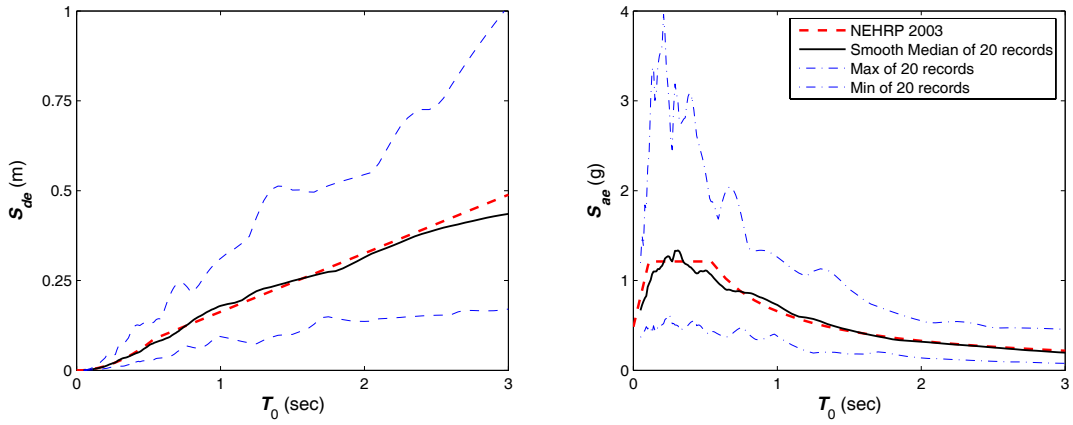

(a) Displacement spectrum (b) Acceleration spectrum

Figure 6.7 Elastic response spectra of SDOF system with 5% damping for considered ground motions

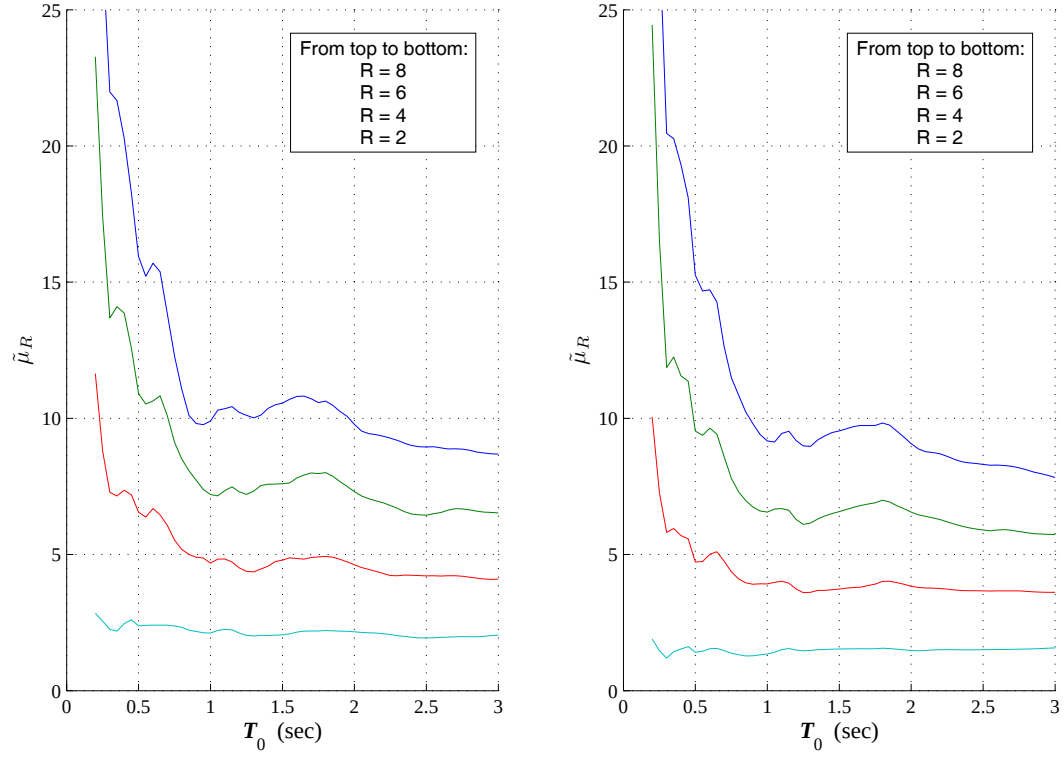

(a) SFDB-NF (b) SFDB

Figure 6.8 Smooth-median constant-*R* spectrum of ductility level, $\tilde{\mu}_R$

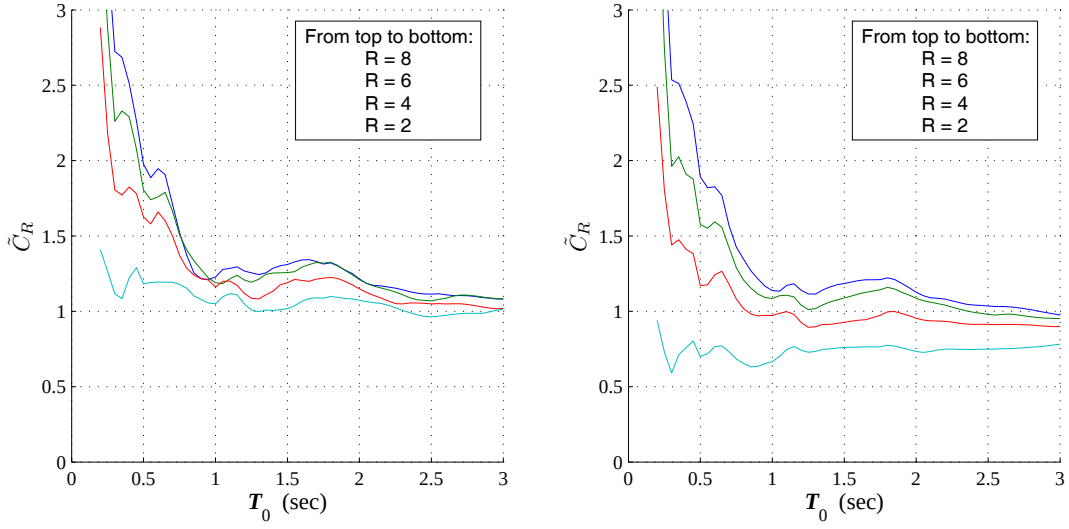

(a) SFDB-NF (b) SFDB

Figure 6.9 Smooth-median constant-*R* spectrum of nonlinear displacement coefficient, $\tilde{C}_R$

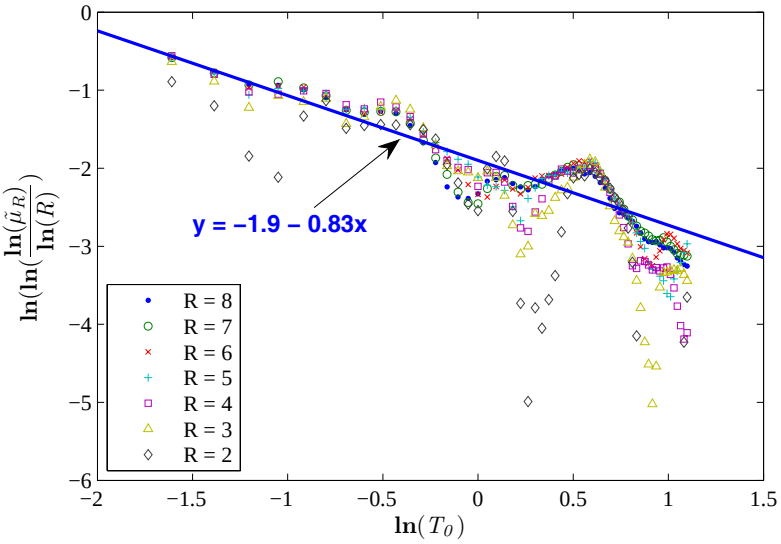

(a) SFDB-NF SDOF system

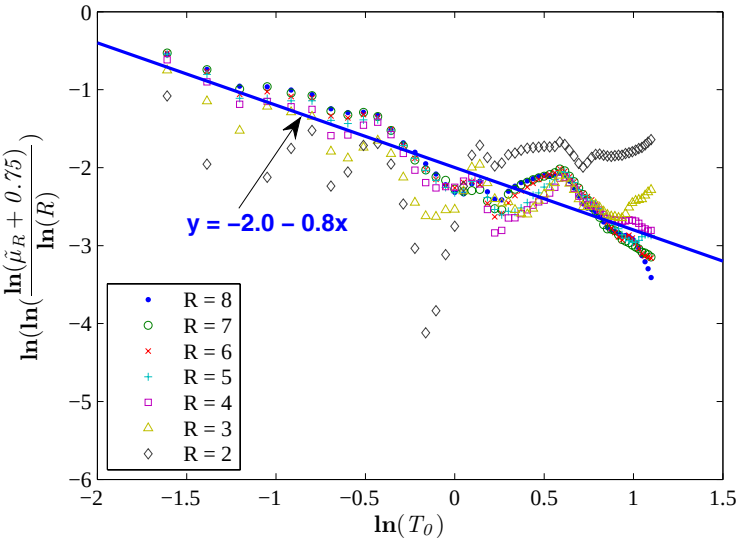

(b) SFDB SDOF system

Figure 6.10 Linear regression of μ_R-R-T_0 relationship

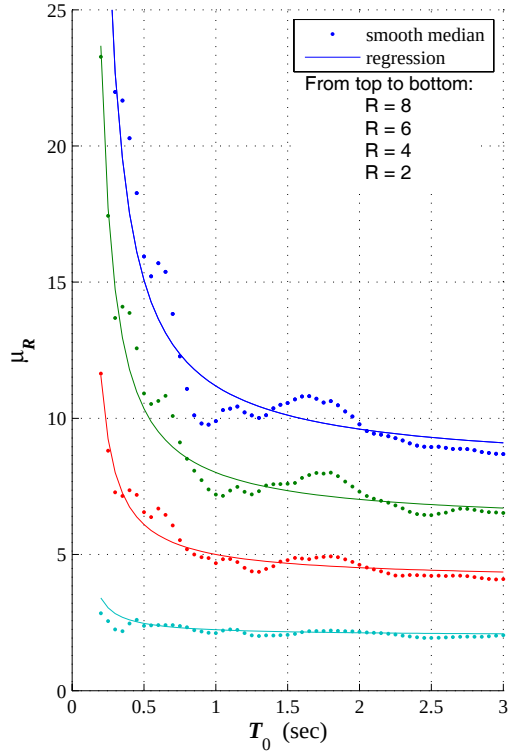

(a) SFDB-NF

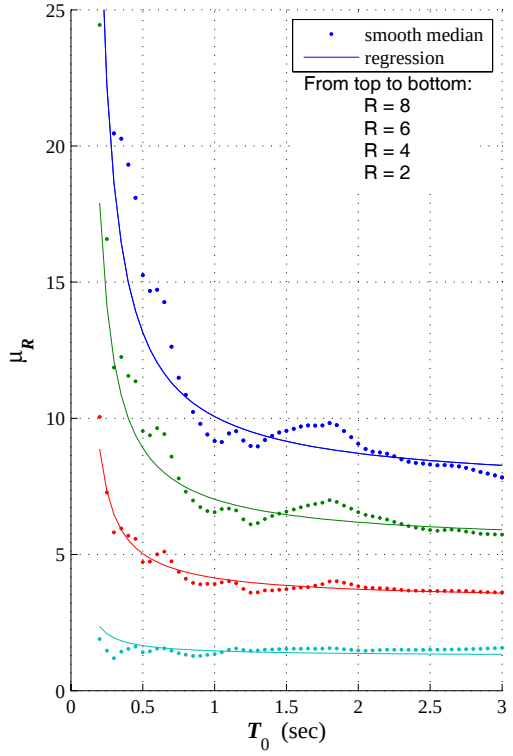

(b) SFDB

Figure 6.11 Comparison of smooth-median $\tilde{\mu}_R$ spectrum and regression function $\hat{\mu}_R$

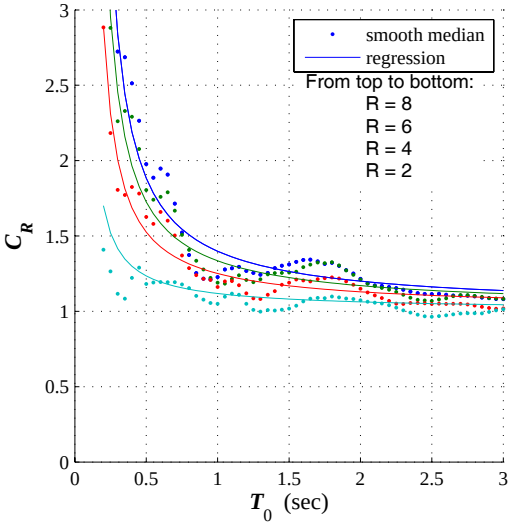

(a) SFDB-NF

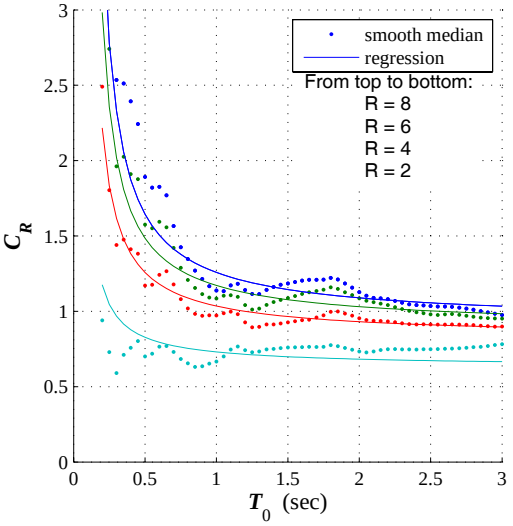

(b) SFDB

Figure 6.12 Comparison of smooth-median $\tilde{C}_R$ spectrum and regression function $\hat{C}_R$

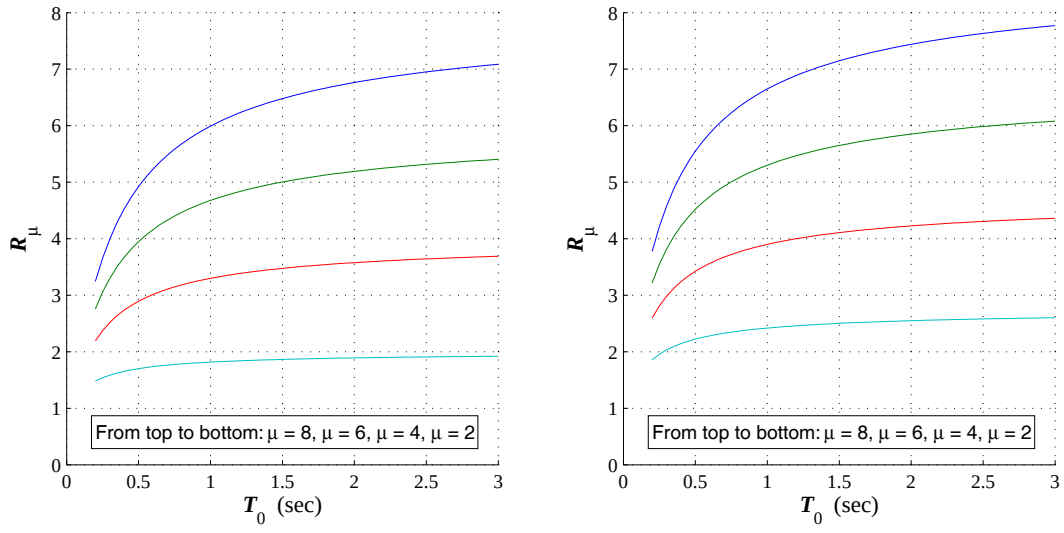

(a) SFDB-NF (b) SFDB

Figure 6.13 Mathematic function $\hat{R}_\mu$

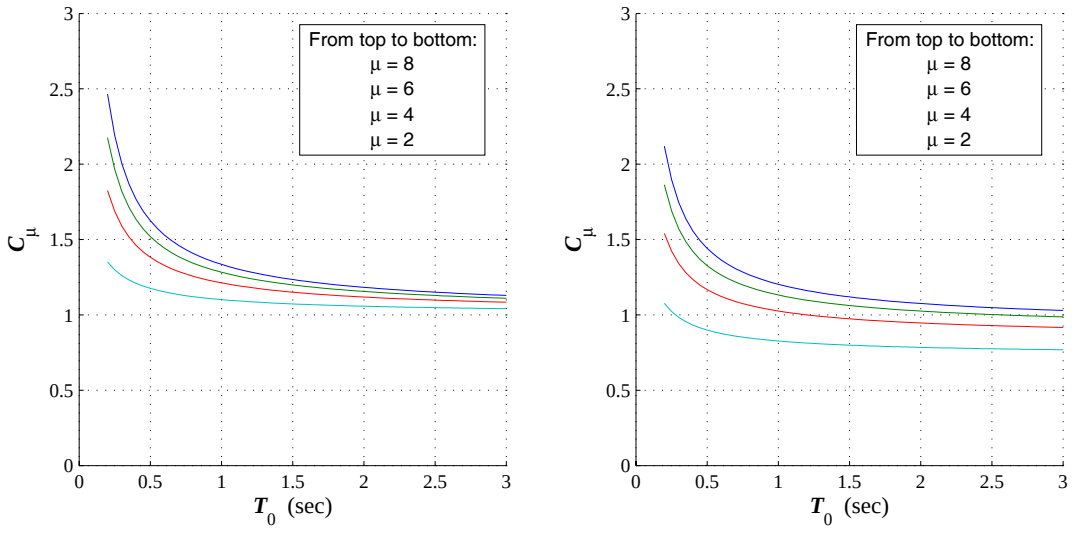

(a) SFDB-NF (b) SFDB

Figure 6.14 Mathematic function $\hat{C}_\mu$

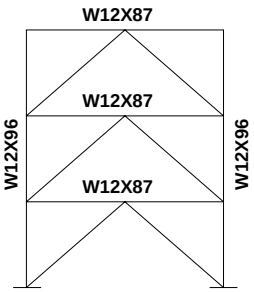

(a) 3-story SFDB frame

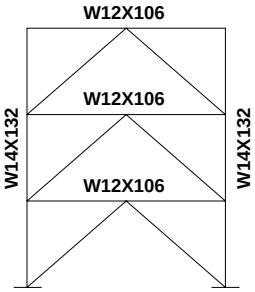

(b) 3-story SFDB-NF frame

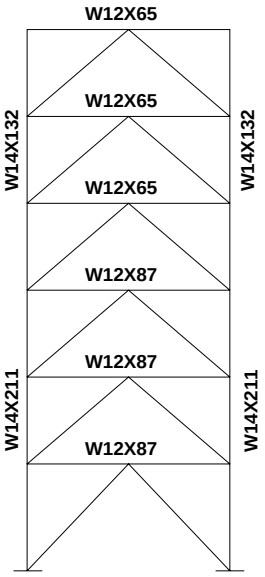

(c) 6-story SFDB frame

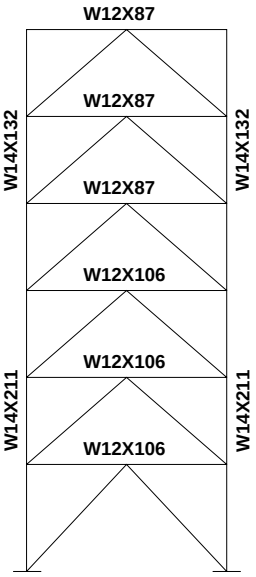

(d) 6-story SFDB-NF frame

Figure 6.15 Elevation of designed frames with member sections

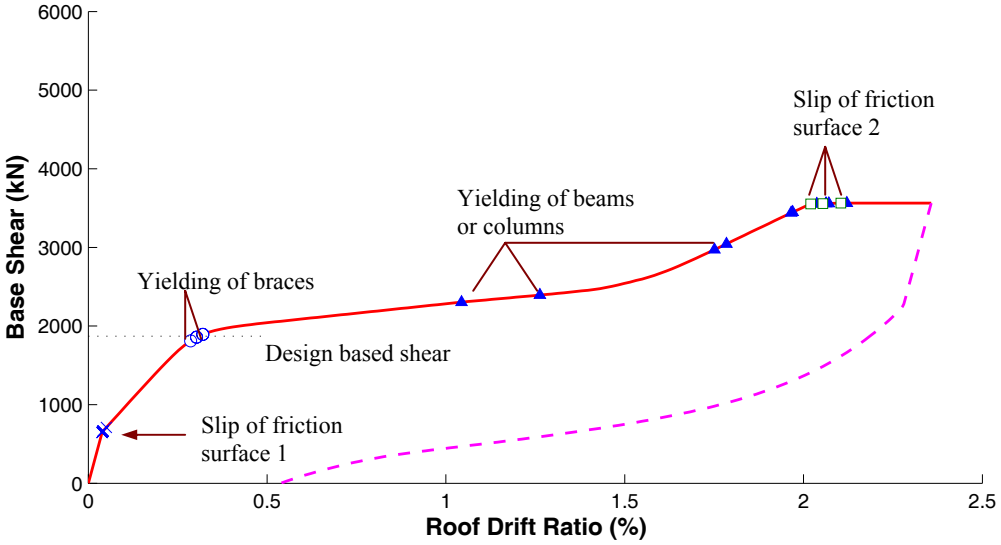

(a) 3-story SFDB frame

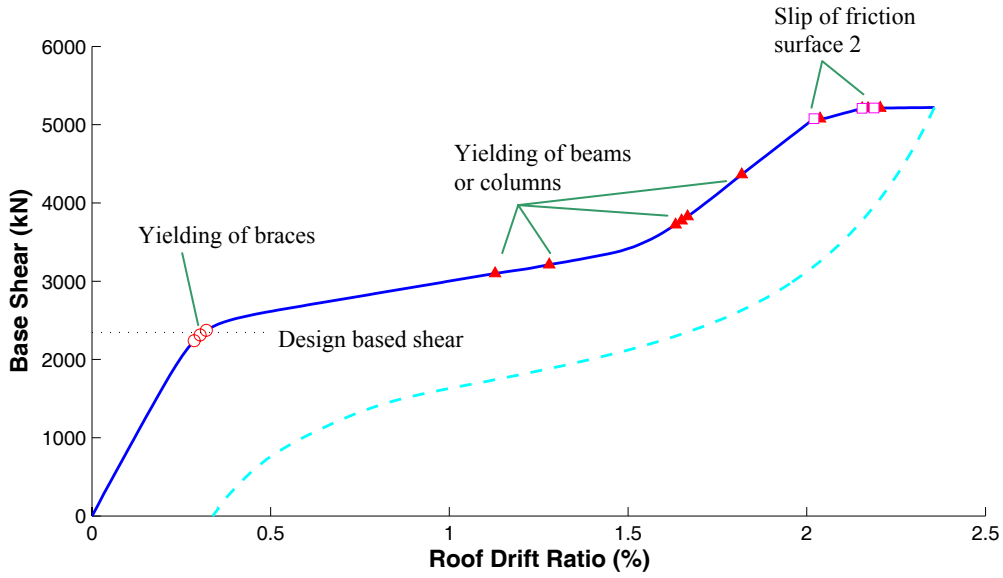

(b) 3-story SFDB-NF frame

Figure 6.16 Pushover analyses of 3-story braced frames

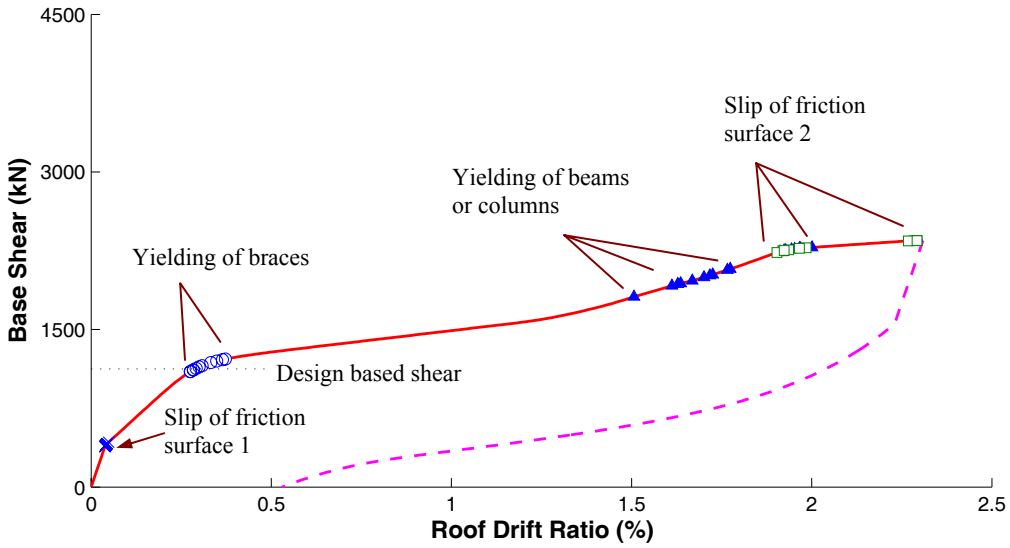

(a) 6-story SFDB frame

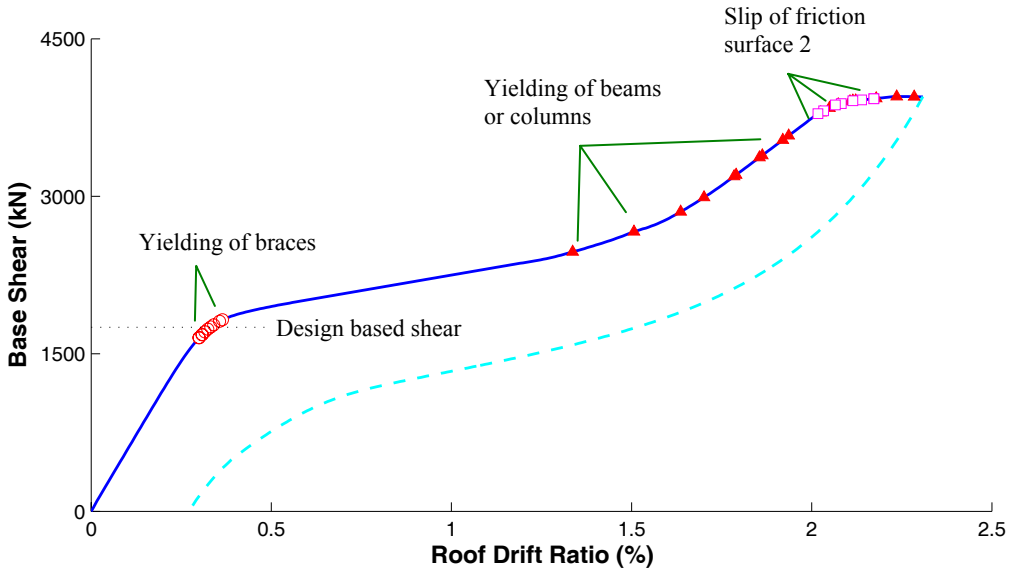

(b) 6-story SFDB-NF frame

Figure 6.17 Pushover analyses of 6-story braced frames

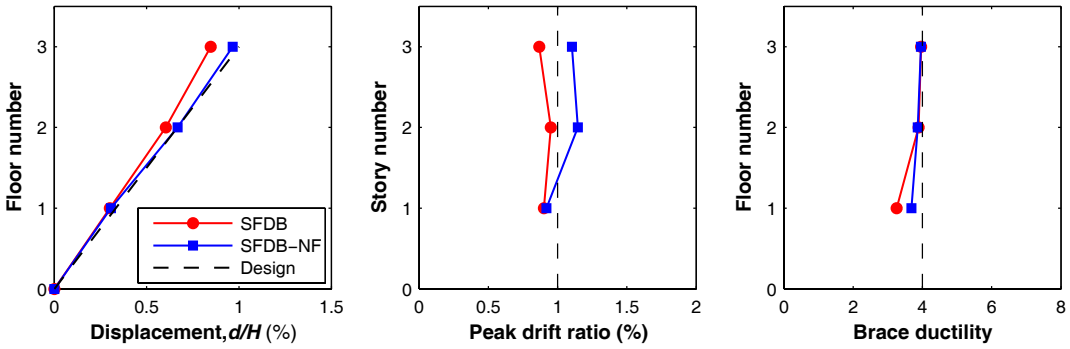

(a) Normalized displacement (b) Peak story drift ratio (c) Ductility level of braces

Figure 6.18 Smooth-median response of 3-story frames under DBE earthquakes

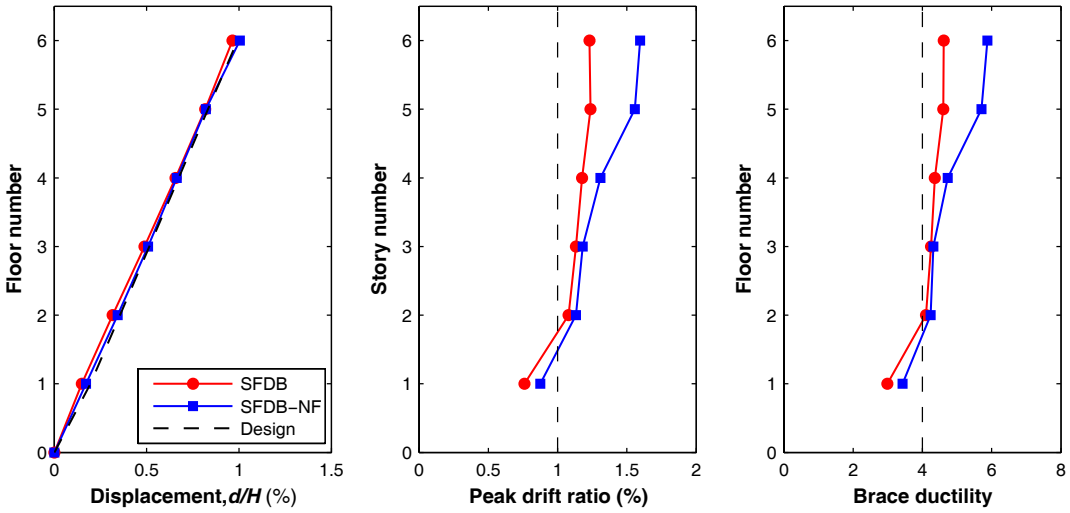

(a) Normalized displacement (b) Peak story drift ratio (c) Ductility level of braces

Figure 6.19 Smooth-median response of 6-story frames under DBE earthquakes

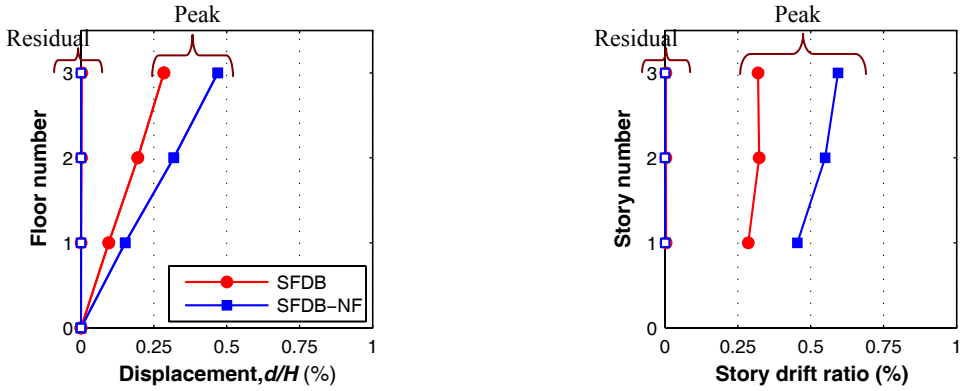

(a) Displacement (b) Inter-story drift ratio

Figure 6.20 Smooth-median response of 3-story building under FE earthquakes

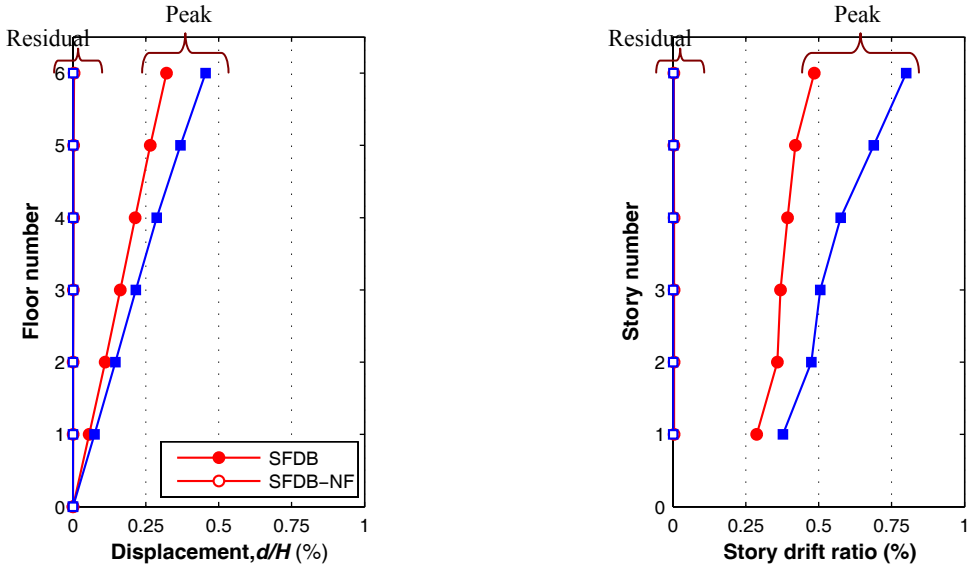

(a) Displacement (b) Inter-story drift ratio

Figure 6.21 Smooth-median response of 6-story building under FE earthquakes

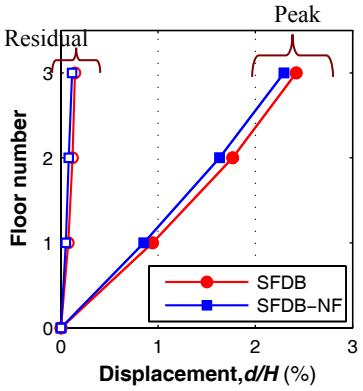

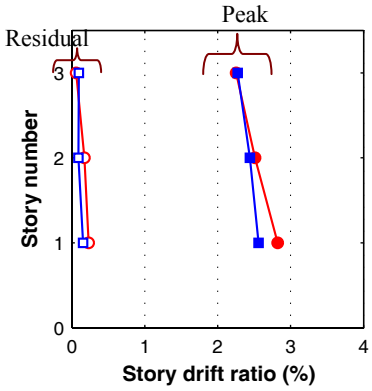

(a) Displacement (b) Inter-story drift ratio

Figure 6.22 Smooth-median response of 3-story building under MCE earthquakes

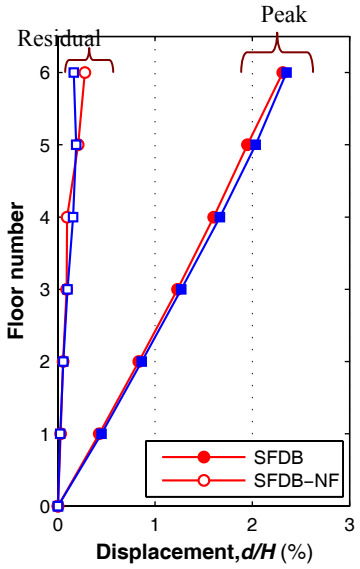

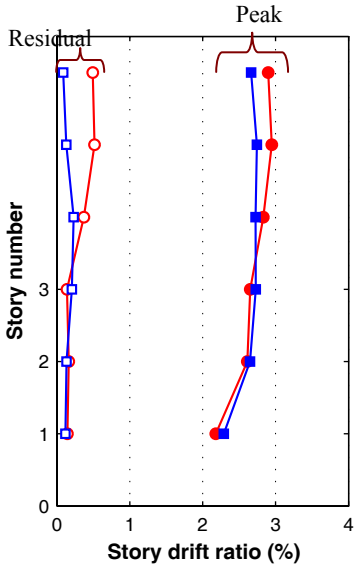

(a) Displacement (b) Inter-story drift ratio

Figure 6.23 Smooth-median response of 6-story building under MCE earthquakes

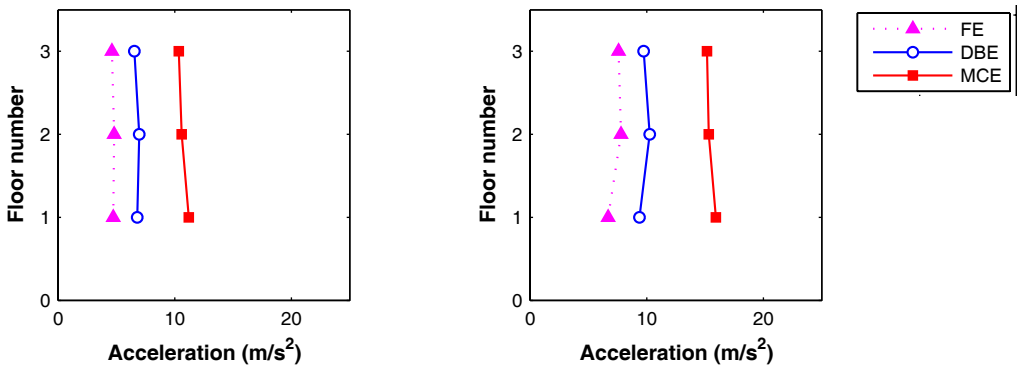

(a) SFDB (b) SFDB-NF

Figure 6.24 Smooth median acceleration of 3-story frames under different seismic intensity levels

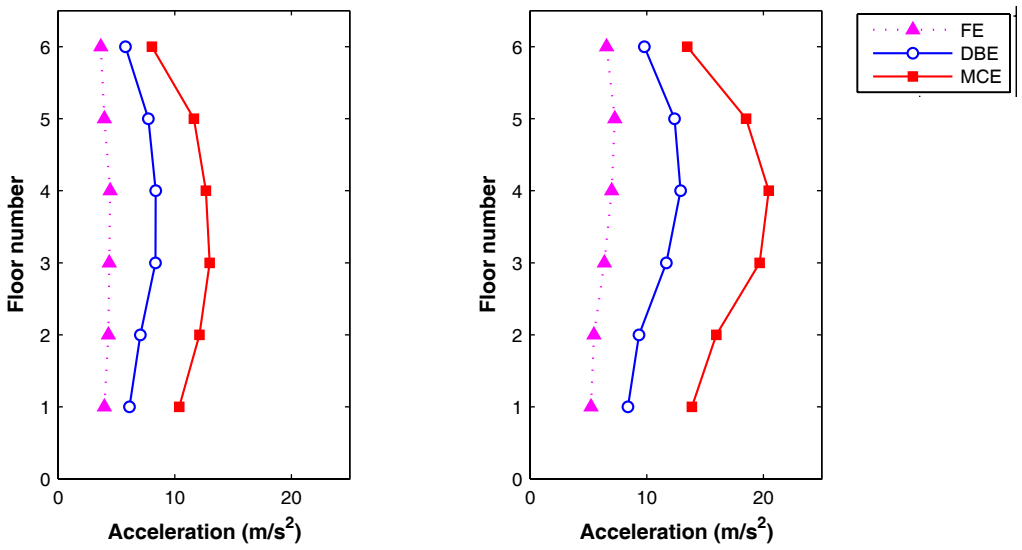

(a) SFDB (b) SFDB-NF

Figure 6.25 Smooth median acceleration of 6-story frames under different seismic intensity levels

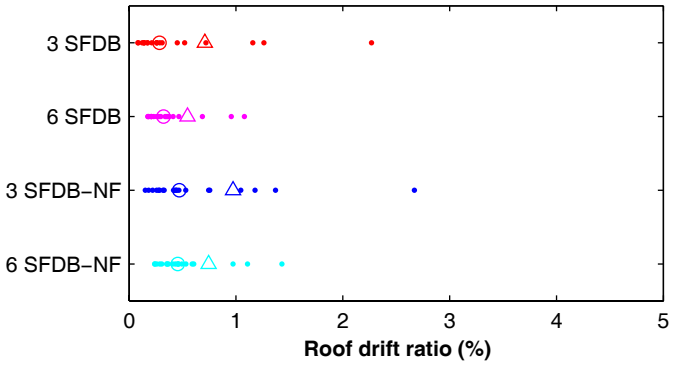

(a) FE earthquakes (50% in 50 years)

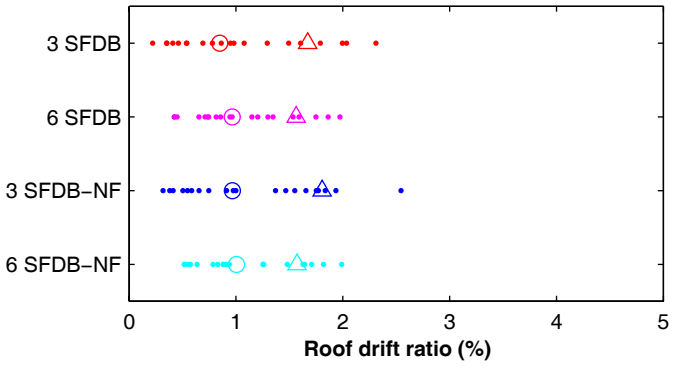

(b) DBE earthquakes (10% in 50 years)

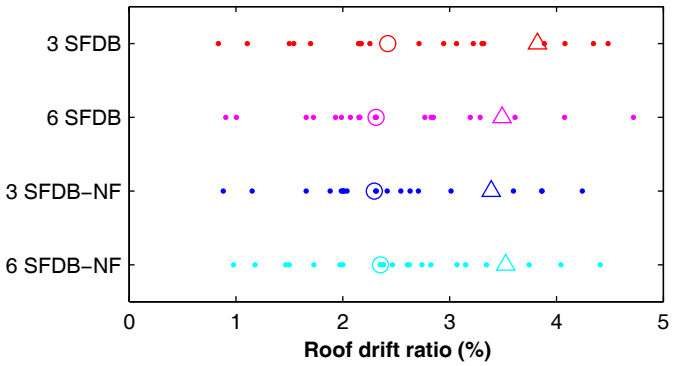

(c) MCE earthquakes (2% in 50 years)

Figure 6.26 Dispersion of all roof drift ratios under different seismic intensity levels (legend: circle = smooth median, triangle = smooth median + standard deviation)

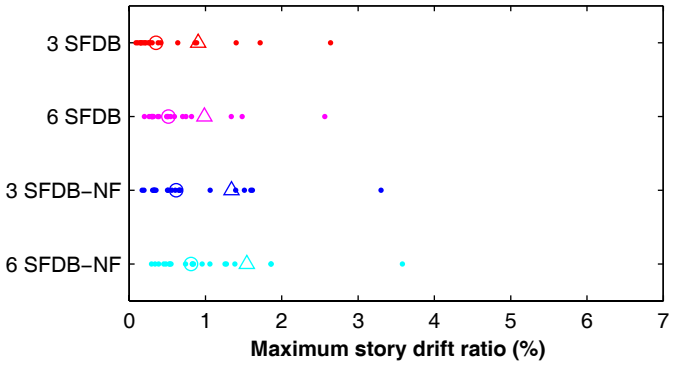

(a) FE earthquakes (50% in 50 years)

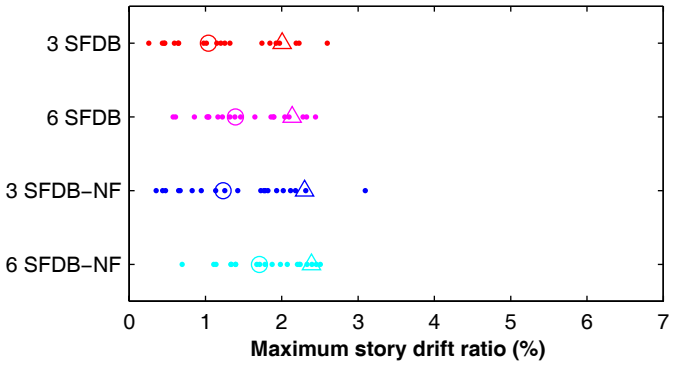

(b) DBE earthquakes (10% in 50 years)

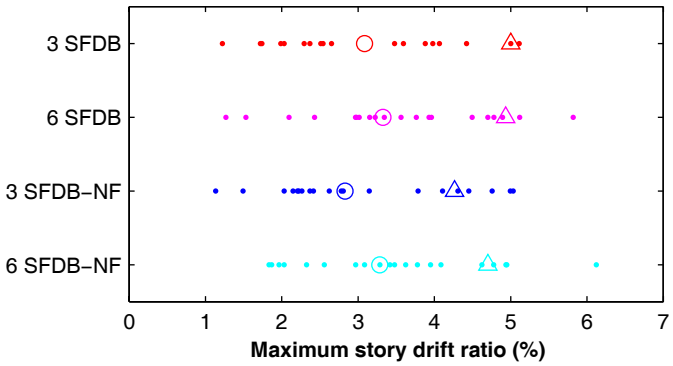

(c) MCE earthquakes (2% in 50 years)

Figure 6.27 Dispersion of all maximum inter-story drfit ratios under different seismic intensity levels (legend: circle = smooth median, triangle = smooth median + standard deviation)

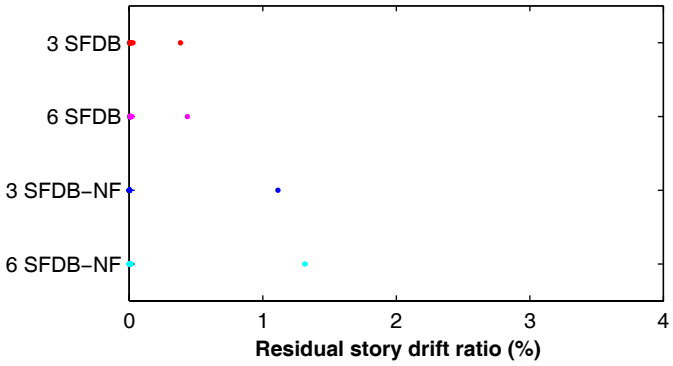

(a) FE earthquakes (50% in 50 years)

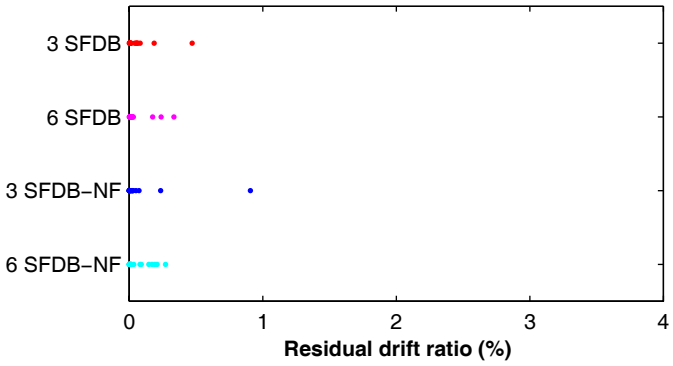

(b) DBE earthquakes (10% in 50 years)

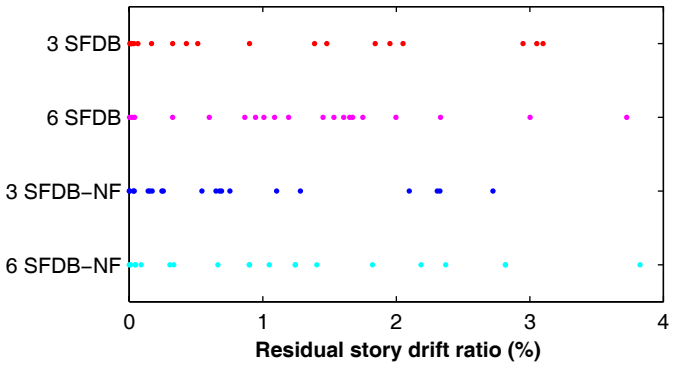

(c) MCE earthquakes (2% in 50 years)

Figure 6.28 Dispersion of residual inter-story drift ratios under different seismic intensity levels (legend: circle = smooth median, triangle = smooth median + standard deviation)

CHAPTER 7 CONCLUSIONS

7.1 SUMMARY

Recognizing the importance of reducing residual deformation in building structures after earthquake, the concept of self-centering seismic resisting system has recently attracted considerable interest. A flag-shaped hysteresis loop is typical of such self-centering systems. Special metals like shape memory alloys (SMA) also exhibit flag-shaped stress-strain curve. This research presents a special type of bracing element termed self-centering friction damping brace (SFDB) which utilizes superelastic SMA wire strands as its core re-centering component while enhanced energy dissipation is realized through friction effect. The current research focuses on the study of the system behavior of SFDB frames under earthquakes with varying earthquake intensity levels. Specifically, this research includes the accomplishment of the following major tasks:

- Establishing a novel mechanical configuration for SFDB device. In SFDB, its re-centering capability is realized using superelastic SMA wires while its enhanced energy dissipation capacity is achieved through friction mechanism.
- Proof-of-concept test of scaled SFDB specimens with various friction force levels.
- Experimental characterization of mechanical properties of superelastic Nitinol wires, including their fatigue life, hysteretic behavior, equivalent damping ratio, and effects of loading rate or temperature.

- Development of a rate-dependent thermo-mechanical constitutive model for superelastic SMA wires, which can be used to predict the loading rate effect on the hysteretic behavior of SMA wires.
- Development of the modified Wilde model for superelastic SMA wires. This is a rate-independent phenomenological model which has relatively simple mathematical expression.
- Feasibility study of using rate-independent constitutive models for superelastic SMA wires in seismic response analyses of structures with SMA-based energy dissipating device.
- Development of analytical models for SFDB device in DRAIN-2DX program. In these analytical models, different constitutive models for SMA wires are used respectively along with the consideration of friction forces at two sliding surfaces in SFDB device.
- Evaluation of seismic performance of SFDB frames through nonlinear pushover analyses and nonlinear time history analyses at specified seismic intensity levels.
- Development of a simplified displacement-based seismic design procedure for SFDB frames. The inter-story drift ratio and brace ductility are selected as the target performance in this design procedure.

This chapter summarizes the research findings and conclusions drawn from this research. Areas for further research in the future are also described.

7.2 CONCLUSIONS

- A training process that involves cyclic preloading for a specified number of load cycles, needs to be performed before the formal use of superelastic Nitinol wires in energy dissipation devices. The training process can effectively minimize accumulation of residual strain and stabilize the hysteretic behavior of superelastic Nitinol wires.
- The temperature variation in superelastic Nitinol wires under dynamic tests affects to some extent the hysteretic behaviors at different loading frequencies.
- In the proposed thermo-mechanical constitutive model for superelastic SMA wire, non-constant elastic modulus lead to more complex expression for the derivative mechanical law and the energy balance equation than constant elastic modulus. The integration scheme proposed in this study can facilitate the numerical simulation of the proposed thermo-mechanical model.
- The proposed thermo-mechanical constitutive model shows a good agreement with experimental stress-strain relationship of superelastic SMA wires at a variety of specified loading rates. The loading rate-induced thermo-mechanical effect, such as the reduction in hysteresis area, rise of the transformation plateau and the increased slope of the loading transformation plateau with increasing loading rates and temperature variation, can be predicted reasonably well by this thermo-mechanical constitutive model.
- The modified Wilde model is capable of simulating the experimental hysteretic behavior of superelastic SMA wires at a specified loading rate through regression.

- This study shows that using rate-independent constitutive models for superelastic SMA wires for seismic response analyses of structures gives fairly accurate results.
- Considering the mathematical complexity for numerical implementation, intensive computational demand and infeasibility for nonlinear static analyses associated with the rate-dependent constitutive models, the rate-independent constitutive models (e.g., the modified Wilde model) for superelastic SMA materials are very appealing to structural engineers for seismic simulation study of SMA-based energy dissipation devices.
- The use of sophisticated thermo-mechanical constitutive models for SMA is required in certain situations such as applications in which considerable changes in environmental temperature are anticipated.
- By properly adjusting the ratio between the 'yield' strength of superelastic Nitinol wire strands and friction force in SFDB, hysteresis loops with nearly self-centering behavior and enhanced energy dissipation can be obtained.
- The results of cyclic testing of scaled SFDB specimens under dynamic loading clearly verify the concept and mechanics of SFDB.
- To overcome the potential overloading problems due to the strain hardening behavior of Nitinol wires at large strain (i.e., >8.0%), a fuse-like device such as slotted bolted connection can be add at the end of SFDB.
- SFDB frames have almost negligible residual story drifts under the frequent earthquakes (FE) and design basis earthquakes (DBE) for Los Angeles, California, while noticeable residual drifts can be observed in SFDB frame after

maximum considered earthquakes (MCE). In general, SFDB frames have minimal residual story drifts in comparison with conventional braced frames (e.g., buckling-restrained braced (BRB) frame) owing to the self-centering behavior of SFDBs.

- In terms of peak story drifts and acceleration response, SFDB frames are capable of achieving a seismic response level comparable to that of BRB frames under the FE and DBE earthquake levels, while BRB frames appear to have better peak-response control performance under the MCE earthquakes.
- Due to the unique behavior of superelastic Nitinol wires such as full strain recovery and long fatigue life, SFDB has the potential to withstand several frequent or design basis earthquakes without the need for replacement.
- Incorporating friction damping in SFDB can significantly improve its seismic performance, while giving a more economical design of SFDB frame buildings than SFDB without friction force.
- SFDB frames designed using the proposed displacement-based design approach can achieve the target displacement profile. However, the current simplified design approach only considers the participation of the fundamental mode and assumes a constant displacement profile for the entire earthquake duration, and thus it tends to give underestimated values for the maximum story drift ratios and brace ductility demands for medium-rise braced frame buildings. Further work is needed to refine this design approach such as by considering the effect of inelastic deformation concentration on story drifts and brace ductility demand in some stories.

In summary, the SFDB frames, if properly designed, have minimal residual drifts under frequent and design basis earthquakes, and SFDBs are able to withstand several design level earthquakes without the need for repair or replacement. In light of these, SFDB appears to be a promising bracing element for seismic resistant structures and has the potential to establish a new type of concentrically braced frame systems with self-centering capability.

7.3 CONTRIBUTIONS

The main contributions of this research work are summarized as follows:

- Development of a concentrically braced frame system with a new type of bracing element termed self-centering friction damping brace (SFDB), which
  (a) exhibits nearly self-centering behavior until relatively large deformation;
  (b) utilizes friction effect for inexpensive and stable energy dissipation during earthquakes;
  (c) can withstand several frequent and design basis earthquakes without the need for replacement because of the high low-cycle fatigue life of nickel-titanium based shape memory alloy (SMA);
  (d) limits the maximum brace force acted on brace connections and adjoined members.
- Establishment of a new unidirectional thermo-mechanical constitutive model which can simulate the superelastic behavior of SMA material and fairly well capture the effect of loading rate and temperature on its mechanical behavior.

This rate-dependent thermo-mechanical constitutive model results in improvements in representing the superelastic behavior of SMA material in the frequency range of interest to seismic applications, and provides a rigorous basis to evaluate the applicability of rate-independent constitutive models in seismic response analyses. Additionally, modifications were made to a rate-independent phenomenological model which can be used to describe the stress-strain relation of superelastic SMA materials at specified values of loading rate and temperature. Extensive study was carried out to compare the performance of these two constitutive models for superelastic SMA materials in seismic analysis.

- Development of a displacement-based design methodology for incorporating and proportioning the proposed new bracing elements (i.e., SFDB) in buildings. It is a relatively simple procedure with a degree of difficulty similar to that of existing design methods but that it can more directly address important response parameters such as lateral displacement demands, peak inter-story drift demands and brace ductility demands.

7.4 FUTURE WORK

The following future work is suggested along the line of current research,

- Constitutive models for superelastic SMA wires that is capable of simulating the complex behavior at large strain including plastic deformation and residual strain, can be developed to facilitate a comprehensive study of SMA-based energy dissipating device.

- The SFDB in present study is intended for use in indoor environment without being subjected to wide range of temperature change. For applications in cold regions such as bridge restrainer, development of SMA materials suitable for cold temperature use is needed.
- Real-time large-scale test of SFDB frame is required to validate its seismic behavior and performance at different earthquake levels.
- In present research, only the ground motion sets for site class D in Los Angeles are used. Ground motion records from soft soil sites and near fault sites were not considered in this study. Nonlinear responses of SFDB frames under such ground motions may be different from those findings given in this study..
- Research work on the connections between SFDB and primary structure such as brace gusset plate and beam-column connections is desired to develop a set of structural details with favorable seismic performance.
- Only two different levels of friction forces are considered in present study. In order to make the design of SFDB frame more flexible, friction force level need to be considered as an additional design parameter in future design procedure.
- Further research is suggested to investigate the effect of inelastic deformation concentration on the inter-story drift ratios and brace ductility demands as well as higher mode participation.
- Probabilistic distributions of seismic responses of SFDB frames under specified earthquake intensity levels need to be studied, and the probability of exceedence in the lifetime of the structure needs to be further considered in the target performance levels to establish a true performance based design procedure. The

information of the probability of exceedence is usually more valuable than median response in structural design or evaluation of structural performance.

- Incremental dynamic analyses of SFDB frames which evaluate the seismic performance of SFDB frames at increasing earthquake intensity levels, is important in the performance-based earthquake engineering.
- To control the damage of acceleration-sensitive contents in buildings under MCE earthquakes, acceleration demand, which is one of the important design criteria, may also be included in the target performance in future design methodology.

REFERENCE

Aiken, I. D., Kelly, J. M., and Pall., A. S. (1988). "Seismic Response of a Nine-story Steel Frame with Friction Damped Cross-bracing." *Proc. Ninth World Conference on Earthquake Engineering*, Tokyo and Kyoto, Japan, August, 1988.

Aiken, I. D., Nims, D. K. and Kelly, J. M. (1992) "Comparative study of four passive energy dissipation systems," *Bulletin of the New Zealand National Society for Earthquake Engineering*. Vol. 25, no. 3, pp. 175-192.

Aiken, I. D., Nims, D. K., Whittaker A.S. and Kelly, J. M. (1993) "Testing of passive energy dissipation systems," *Earthquake Spectra*. Vol. 9, no. 3, pp. 335-370.

Aiken, I. D., Nims, D. K., Whittaker, A.S. and Kelly, J. M. (1993) "Testing of passive energy dissipation systems," *Earthquake Spectra*, 9(3): 335-370.

AISC (2005), "2005 Seismic Provisions for Structural Steel Buildings," American Institute of Steel Construction, Chicago, IL.

Andrawes, B. and DesRoches, R. (2005) "Unseating prevention for multiple frame bridges using superelastic devices," *Smart Mater. Struct.*, 14: S60-S67.

Ang, A. H-S. and Tang, W. H. (1975) "Probability concepts in engineering planning and design: Volume I—basic principles," John Wiley & Sons, NY.

ATC (2002) "Preliminary evaluation of methods for defining performance," *Rep. ATC-58-2*, Applied Technology Council, Redwood City, 2002.

Anderson, E. and Mahin, S. A. (1997) "A displacement-based design approach for seismically isolated bridges," In: Fajfar P, Krawinkler H. Editors. *Seismic design methodologies for the next generation of codes*. Rotterdam: AA Balkema, 1997: 383-394.

Auricchio, F. and Sacco, E. (1999) "Modelling of the rate-dependent superelastic behavior of Shape-Memory Alloys," *ECCM '99, European Conference on Computational Machanics*, August 31-September 3, Munchen, Germany.

Auricchio, F. and Sacco, E. (2001) "Thermo-mechanical modeling of a superelastic shape-memory wire under cyclic stretching-bending loadings," *International Journal of Solids and Structures*, 38: 6123-6145.

Auricchio, F., Fugazza, D. and DesRoches, R. (2006) “Numerical and experimental evaluation of the damping properties of shape-memory alloys,” *Journal of Engineering Materials and Technology*, 128: 312-319.

Baz, A., Poh, S., Ro, J. and Gilheany, J. (1995) “Control of the natural frequencies of Nitinol-reinforced composite beams,” *Journal of Sound and Vibration*, 185(1): 171-185.

Borzi, B., Calvi, G. M., Elnashai, A. S., Faccioli, E. and Bommer, J. J. (2001) “Inelastic spectra for displacement-based seismic design,” *Soil Dynamics and Earthquake Engineering*, 21: 47-61.

Boyd, J. G. and Lagoudas, D. C. (1998) “A thermodynamic constitutive model for the shape memory materials part I: the monolithic shape memory alloys.” *International Journal of Plasticity*, 6: 805-842.

Brinson, L. C. (1993) “One-dimensional constitutive behavior of shape memory alloys: Thermomechanical derivation with non-constant material functions and redefined martensite internal variable,” *J. Intell. Mater. Syst. Struct.* 4: 229-242.

Brinson, L. C. and Huang, M. S. (1996) “Simplifications and comparisons of shape memory alloy constitutive models,” *J. Intell. Mater. Syst. Struct.*, **7**(1): 108-114.

Brocca, M., Brinson, L. C., and Bazant, Z. P. (2002) “Three-dimensional constitutive model for shape memory alloys based on microplane model,” *Journal of the Mechanics and Physics of Solids*, 50: 1051-1077.

Calvi, G. M. and Kingsley, G. R. (1995) “Displacement-based design of multi-degree of freedom bridge structures,” *Earthquake Engineering and Structural Dynamics*, 24: 1247-1266.

Cardone, D., Coelho, E., Dolce, M. and Ponzo, F. (2004) “Experimental behaviour of RC frames retrofitted with dissipating and re-centring braces.” *Journal of Earthquake Engineering*, 8(3): 361–396.

Chopra, A. K. (2001) “Dynamics of Structures,” Prentice-Hall, NJ

Chopra, A. K. and Chintanapakdee, C. (2001) “Comparing response of SDF systems to near-fault and far-fault earthquake motions in the context of spectral regions,” *Earthquake Engineering and Structural Dynamics*, 30: 1769-1789.

Chopra, A. K. and Goel, R. K. (2001) “Direct displacement-based design: use of inelastic vs. elastic design spectra,” *Earthquake Spectra*, 17(1): 47-64.

Chopra, A. K. and Chintanapakdee, C. (2004) “Inelastic deformation ratios for design and evaluation of structures: single-degree-of-freedom bilinear systems,” ASCE *Journal of Structural Engineering*, 130(9): 1309-1319.

Christopoulos, C., Filiatrault, A., and Folz, B. (2002) “Seismic response of self-centering hysteretic SDOF systems,” *Earthquake Engineering and Structural Dynamic*s, 31, 1131–1150.

Christopoulos, C., Filiatrault, A., and Folz, B. (2002a). “Seismic response of self-centering hysteretic SDOF systems,” *Earthquake Engineering and Structural Dynamics*, 31: 1131–1150.

Christopoulos, C., Filiatrault, A., Folz, B., and Uang, C-M. (2002b), “Post-Tensioned Energy Dissipating Connections for Moment-Resisting Steel Frames,” ASCE *Journal of Structural Engineering*, 128(9): 1111-1120.

Christopoulos, C. and Pampanin, S. (2004) “Towards performance-based seismic design of MDOF structures with explicit consideration of residual deformations,” ISET *Journal of Earthquake Technology*, 41(1): 53-73.

Clark PW, Aiken ID, Kelly JM, Higashimo M, Krumme RC. (1995) “Experimental and analytical studies of shape memory alloy dampers for structural control,” *Proc., the 1995 Conference on Smart Structures and Materials, SPIE, vol. 2445*, pg. 241-251.

Clark, P. W., Aiken, I. D., Kasai, K., Ko, E., and Kimura, I., (1999) “Design procedures for buildings incorporating hysteretic damping devices,” *Proc., the 69th SEAOC Annual Convention*, Sacramento, CA.

DesRoches, R., McCormick, J., and Delemont, M. (2004) “Cyclic properties of superelastic shape memory alloy wires and bars,” ASCE *Journal of Structural Engineering*, 130(1): 38-46.

Dolce, M., Cardone, D., and Marnetto, R. (2000) “Implementation and testing of passive control devices based on shape memory alloys,” *Earthquake Engrg. Struct. Dyn,*, 29(7): 945-968.

Dolce M. and Cardone D. (2001) “Mechanical behavior of shape memory alloys for seismic applications 2. Austenite NiTi wires subjected to tension,” *International Journal of Mechanical Sciences*, 43: 2657-2677.

Dolce M., Cardone D, Ponzo FC, Valente C. (2005) “Shaking table tests on reinforced concrete frames without and with passive control systems,” *Earthquake Engineering and Structural Dynamics*, 34(14): 1687-1717.

Fajar, P. and Krawinkler, H. (Eds) (1997) “Seismic design methodologies for the next generation of codes,” Proceedings of International Conference at Bled, Slovenia, A.A. Balkema, Rotterdam/Brookfield, 1997, 411 pp.

Fajar, P. and Krawinkler, H. (Eds) (2004) “Performance-based seismic design concepts and implementation,” Proceedings of International Workshop at Bled, Slovenia, June 28-July 1, 2004, PEER Report 2004/05, Pacific Earthquake Engineering Research Center, University of California, Berkeley.

Fajfar, P., Gaspersic, P. and Drobnic, D. (1997) “A simplified nonlinear method for seismic damage analysis of structures,” In: Fajfar P, Krawinkler H. Editors. *Seismic design methodologies for the next generation of codes*. Rotterdam: AA Balkema, 1997: 183-194.

Fajar, P. (2000) “A nonlinear analysis method for performance based seismic design,” *Earthquake Spectra*, 16: 573-592

Farrow, K. T. and Kurama, Y. C. (2003) “SDOF demand index relationships for performance-based seismic design,” *Earthquake Spectra*, 19(4): 799-838.

FEMA (2000) “Prestandard and commentary for the seismic rehabilitation of buildings”, FEMA-356, Federal Emergency Management Agency, Washing D.C.

FEMA (2003) “NEHRP recommended provisions for seismic regulations for new buildings and other structures”, FEMA-450, Federal Emergency Management Agency, Washington D.C.

FitzGerald, T. F., Anagnos, T., Goodson, M. and Zsutty, T. (1989) “Slotted bolted connections in aseismic design for concentrically braced connections,” *Earthquake Spectra*, 5(2): 383-391.

Funakubo, H. (1987) “Shape memory alloys,” Gordon and Breach Science Publishers, New York, NY.

Graesser, E.J., and Cozzarelli, F.A. (1991). “Shape-memory alloys as new materials for aseismic isolation.” ASCE *J. Eng. Mech*., 117(11): 2590-2608.

Gupta, A. and Krawinkler, H. (2000) “Estimate of seismic drift demands for frame structures,” *Earthquake Engineering and Structural Dyanmics*, Vol. 29,: 1287-1305

Hodgson, D. E., Krumme, R. C. (1994) “Damping in structural applications,” *Proc., the 1st International Conference on Shape Memory and Superelastic Technologies*, Pacific Grove, CA, USA.

Housner, G. W., Bergman, L. A., Caughey, T. K., Chassiakos, A. G., Claus, R. O., Masri, S. F., Skelton, R. E., Soong, T. T., Spencer, B. F., Yao, J. T. P. (1997). "Structural control: Past, present and future," ASCE *J. Engrg. Mech.*, 123(9): 897–971.

Ivshin, Y. and Pence, T. J. (1994) "A constitutive model for hysteretic phase transition behavior," *Int. J. Eng. Sci.* 32: 681–704.

Janke, L., Czaderski, C., Motavalli, M. and Ruth, J. (2005) "Applications of shape memory alloys in civil engineering structures - Overview, limits and new ideas," *Materials and Structures*, 38: 578-592.

Kiggins, S. and Uang, C. M. (2004). "Reducing residual drifts in BRBF systems," *Proc., 73rd SEAOC Annual Convention, Sacramento*, CA, pp. 481-492.

Kowalsky, M. J., Priestley, M. J. N. and MacRae, G. A. (1995). "Displacement-based design of RC bridge columns in seismic regions," *Earthquake Engineering and Structural Dynamics*, 24: 1623-1643.

Kowalski, M. and Priestley, M. J. N. (1996) "A direct displacement-based design approach for reinforced concrete bridges," *Proc., 4th Caltrans Seismic Research Workshop*, Sacramento, June 1996.

Kowalsky, M. J. (2002) "A displacement-based approach for the seismic design of continuous concrete bridges," *Earthquake Engineering and Structural Dynamics*, 31: 719-747.

Kurama, Y., Sause, R., Pessiki, S. and Lu, L.-W. (1999). "Lateral load behavior and seismic design of unbonded post-tensioned precast concrete walls," *ACI Structural Journal*, 96(4): 622–632.

Liang, C. and Rogers, C. A. (1990) "One-dimensional thermomechanical constitutive relations for shape memory materials," *J. Intell. Mater. Syst. Struct.*, 1(2): 207-234

Liang, C. (1990) "The constitutive modeling of shape memory alloys," *Ph.D. thesis, Virginia Tech*

Mao, C. and Li, H. (2005) "SMA-based smart damper/displacement transducer," *Smart Structures and Materials 2005: Sensors and Smart structures Technologies for Civil, Mechanical and Aerospace Systems*, Proc. of SPIE Vol. 5765, Bellingham, WA. pp: 442-452

Maugin, G. A. (1999) "The thermomechanics of nonlinear irreversible behaviors: an introduction," World Scientific Publishing, Singapore.

McCormick, J., DesRoches, R., Fugazza, D. and Auricchio, F. (2006) “Seismic vibration control using superelastic shape memory alloys,” *ASME J. Engineering Materials and Technology*, 128: 294-301.

Miranda, E. (2000) “Inelastic displacement ratios for structure on firm site,” ASCE *Journal of Structural Engineering*, 126(10): 1150-1159.

Miranda, E. (2001) “Estimation of inelastic deformation demands of SDOF systems,” ASCE *Journal of Structural Engineering*, 127(9): 1005-1012.

Miranda, E. and Bertero, V. V. (1994) “Evaluation of strength reduction factors for earthquake resistant design,” *Earthquake Spectra*, 10(2): 357-379.

Miranda, E. and Reyes, C. J. (2002) “Approximate lateral drift demands in multistory buildings with nonuniform stiffness,” Journal of Structural Engineering, 128(7): 840-849.

Moehle, J. P. (1984) “Strong motion drift estimates for R/C structures,” ASCE *Journal of Structural Engineering*, 110(9): 1988-2001.

Moehel, J. P. (1992) “Displacement-based design of RC structures subjected to earthquakes,” *Earthquake Spectra*, 8(3): 403-428.

Nassar, A. A. and Krawinkler, H. (1991) “Seismic demands for SDOF and MDOF systems,” Report. No 95, John Blume Earthquake Engineering Center, Department of Civil Engineering, Stanford Univeristy, Stanford, CA.

Newmark, N. M. and Hall, W. J. (1982) “Earthquake spectra and design,” *EERI Monograph*, Earthquake Engineering Research Institute, Oakland, CA.

Nims, D.K., Ritcher, P.J., and Bachman, R.E. (1993) “The use of the energy dissipating restraint for seismic hazard mitigation,” *Earthquake Spectra*, 9(3): 467-489.

Otsuka, K. and Kakeshita, T. (2002) “Science and technology of shape-memory alloys: new developments,” *MRS Bulletin*, February, 2002, pp. 91-100.

Ozdemir, H. (1976). “Nonlinear transient dynamic analysis of yielding structures,” *PhD Thesis*, University of California, Berkeley, CA.

Pampanin S., Christopoulos and C, Priestley, M. J. N. (2003) “Performance-based seismic response of frame structures including residual deformations. Part II: multi-degree of freedom systems,” *Journal of Earthquake Engineering*, 7(1): 119-147.

Prahlad, H. and Chopra, I. (2003) “Development of a strain-rate dependent model for uniaxial loading of SMA wires.” *J. Intell. Mater. Syst. Struct.,* 14: 429-442.

Prakash, V., Powell, G.H., and Campbell, S. (1993). “DRAIN-2DX: Base Program and User Guide,” *Report No. UCB/SES-93/17*, University of California, Berkeley, CA.

Priestley, M. J. N. (1998). “Displacement-based approaches to rational limit states design of new structures,” Keynote Address in the *11th European Conference on Earthquake Engineering*, Paris, France.

Priestley, M. J. N. (2000) “Performance based seismic design,” *Proc., 12th World Conference on Earthquake Engineering*, Paper No. 2831, Auckland, New Zealand, January-February 2000.

Priestley, M. J. N. and Kowalsky, M. J. (2000) “Direct displacement-based seismic design of concrete buildings,” *Bulletin of the New Zealand Society for Earthquake Engineering*, 33(4): 421-444.

Priestley, M. J. N. and Calvi, G. M. (1997) “Concepts and procedures for direct displacement-based design and assessment,” In: Fajfar P, Krawinkler H. Editors. *Seismic design methodologies for the next generation of codes*. Rotterdam: AA Balkema, 1997: 171-81.

Qi, X. and Moehle, J. P. (1991) “Displacement design approach for reinforced concrete structures subjected to earthquakes,” *Report No. UCB/EERC-91/02*, Earthquake Engineering Research Center, University of California at Berkeley, Berkeley, California, January 1991, 186 pp.

Ricles, J. M., Sause, R., Garlock, M. M., and Zhao, C. (2001), “Posttensioned seismic-resistant connections for steel frames,” *Journal of Structural Engineering*, 127(2): 113-121.

Ruiz-Garcia, J. and Miranda, E. (2003) “Inelastic displacement ratios for evaluation of existing structures,” *Earthquake Engineering and Structural Dynamics*, 32: 1237-1258.

Ruiz-Garcia, J. and Miranda, E. (2006a) “Evaluation of residual drift demands in regular multi-storey frames for performance-based seismic assessment,” *Earthquake Engineering and Structural Dynamics*, 35: 1609-1629.

Ruiz-Garcia, J. and Miranda, E. (2006b) “Residual displacement ratios for assessment of existing structures,” *Earthquake Engineering and Structural Dynamics*, 35: 315-336.

Sabelli, R. (2001) “Research on improving the design and analysis of earthquake resistant steel braced frames,” *The 2000 NEHRP Professional Fellowship Report, Earthquake Engineering Research Institut*, Oakland, SA.

Sabelli, R., Mahin, S.A., and Chang, C. (2003). “Seismic demands on steel-braced buildings with buckling-restrained braces,” *Engineering Structures*, 25: 655-666.

Sadjadpour, A. and Bhattacharya, K. (2006) “A micromechanics inspired constitutive model for shapememory alloys: the one-dimensional case,” *Smart Mat. Struct*., 16: S51-S62

Sato, Y. and Tanaka, K. (1988) “Estimation of energy dissipation in alloys due to stress-induced martensitic transformation,” *Res Mechanica*, 23: 381-393.

Schmidt, I. (2006) “A phenomenological model for superelastic NiTi wires based on plasticity with focus on strain-rate dependency caused by temperature,” *J. Engineering Materials and Technology*, 128: 279-284.

SEAOC (1995) “Performance based seismic engineering of buildings,” *Vision 2000 report*, Structural Engineers Association of California, Volumes I and II, Sacramento, California.

Seo, C. Y. and Sause, R. (2005) “Ductility demands on self-centering systems under earthquake loading.” *ACI Structural Journal*, 102(2): 275-285

Seo, C. Y. (2005) “Influence of ground motion characteristics and structural parameters on seismic responses of SDOF systems,” *Ph.D. dissertation*, Department of Civil and Environmental Engineering, Lehigh University, Bethlehem, PA.

Shimazaki, K. and Sozen, M. A. (1985) “Seismic drift of reinforced concrete structures,” Special research paper, Hazama-Gumi, Ltd., Tokyo, Japan, 1985.

Smith, R. C., Seelecke, S., Dapino, M. and Ounaies, Z. (2006) “A unified framework for modeling hysteresis in ferroic materials,” *Journal of the mechanics and physics of solids*, **54**(1): 46-85.

Sommerville, P., et al. (1997) “Development of ground motion time histories for Phase 2 of the FEAM/SAC steel project,” *SAC Background document SAC/BD-91/04*, SAC joint venture, Sacramento, California.

Soong, T. T. and Dargush, G. G. (1997) “Passive energy dissipation systems in structural engineering,” John Wiley & Sons Ltd, West Sussex, England.

Sullivan, T., Calvi, G.M., Priestley, M.J.N. and Kowalsky, M. (2003) "The limitations and performances of different displacement-based design methods," *Journal of Earthquake Engineering*, 7(No. Special Issue 1): 201-241.

Tanaka, K. (1986) "A thermomechanical sketch of shape memory effect: one-dimensional tensile behavior," *Res. Mechanica,* 18: 251-263.

Tsai, K. C., Weng, Y. T., Lin, M. L., Chen, C. H., Lai, J. W. and Hsiao, P. C. (2004) "Pseudo dynamic tests of a full-scale CFT/BRB composite frame: displacement based seismic design and response evaluations," *Proc. The 2004 Structures Congress - Building On The Past: Securing The Future*, Nashville, Tennessee, May 22-26, 2004.

Uang, C. M., Nakashima, M., and Tsai, K. C. (2004). "Research and application of buckling-restrained braced frames," *International Journal of Steel Structures*, 4: 301-313.

Vidic, T., Fajar, P. and Fischinger, M. (1994) "Consistent inelastic design spectra: strength and displacement," *Earthquake Engineering and Structural Dynamics*, 23:507-521.

Vitiello, A., Giorleo, G. and Morace, R. E. (2005) "Analysis of thermomechanical behaviour of Nitinol wires with high strain rates," *Smart Mat. Struct*., 14: 215-221.

Wang, R., Cho, C., Kim, C. and Pan, Q. (2006) "A proposed phenomenological model for shape memory alloys," *Smart Mat. Struct*., 15: 393-400

Whittaker, A. S., Krumme, R., Sweeney, S. C. and Hayes, J. R. (1995) "Structural control of building response using shape-memory alloys. Phase 1," *USACERL Technical Report 95/22*, Construction Engineer Research Laboratories, US Army Corps of Engineers, Champaign, IL.

Wilde, K., Gardoni, P., and Fujino, Y. (2000) "Base isolation system with shape memory alloy device for elevated highway bridges," *Eng. Struct*., 22(3): 222-229.

Wilson, J. C. and Wesolowsky, M. J. (2005). "Shape memory alloys for seismic response modification: a state-of-the-art review," *Earthquake Spectra*, 21(2): 569-601.

APPENDIX A GROUND MOTION SETS

The time history analyses in this study employ the suites of earthquake ground motions developed previously by Somerville et al. (1997) for use in the FEMA/SAC Steel Project on steel moment-resisting frames. Suites of acceleration time histories were developed for three different sites—Los Angeles, Boston and Seattle, and for different seismic hazard levels which are corresponding to 50%, 10% and 2% probability of excedence in a 50 years respectively. Each suite which contains twenty ground motion records is corresponding to one specific site and seismic hazard level. These twenty records were derived from fault-parallel and fault-normal orientations of ten earthquake records with adjustment in amplitude and frequency domain in order to match the target response spectra defined in the 1994 *NEHRP* provisions.

Three earthquake suites, totally 60 ground motions, corresponding to site class D (firm soil) at downtown Los Angeles, California, are selected in this study. These three suites, designated as LA01 – LA20, LA21 – LA40 and LA41 – LA60 respectively, represent seismic hazard levels with a 10%, 2% and 50% probability of exceedance in a 50 year period, respectively. Table A.1 to Table A.3 show the details of 60 ground motions including earthquake names, magnitudes, site distance and scale factors. More detailed procedure for generating these ground motion time histories can be found in Somerville et al. (1997).

Table A.1 Los Angeles ground motions (10% in 50 years)

SAC Name	Record	Earthquake Magnitude	Distance (km)	Scale Factor	Number of Points	DT (sec)	Duration (sec)	PGA (cm/sec^2)
LA01	Imperial Valley, 1940, El Centro	6.9	10	2.01	2674	0.02	39.38	452.03
LA02	Imperial Valley, 1940, El Centro	6.9	10	2.01	2674	0.02	39.38	662.88
LA03	Imperial Valley, 1979, Array #05	6.5	4.1	1.01	3939	0.01	39.38	386.04
LA04	Imperial Valley, 1979, Array #05	6.5	4.1	1.01	3939	0.01	39.38	478.65
LA05	Imperial Valley, 1979, Array #06	6.5	1.2	0.84	3909	0.01	39.08	295.69
LA06	Imperial Valley, 1979, Array #06	6.5	1.2	0.84	3909	0.01	39.08	230.08
LA07	Landers, 1992, Barstow	7.3	36	3.2	4000	0.02	79.98	412.98
LA08	Landers, 1992, Barstow	7.3	36	3.2	4000	0.02	79.98	417.49
LA09	Landers, 1992, Yermo	7.3	25	2.17	4000	0.02	79.98	509.70
LA10	Landers, 1992, Yermo	7.3	25	2.17	4000	0.02	79.98	353.35
LA11	Loma Prieta, 1989, Gilroy	7	12	1.79	2000	0.02	39.98	652.49
LA12	Loma Prieta, 1989, Gilroy	7	12	1.79	2000	0.02	39.98	950.93
LA13	Northridge, 1994, Newhall	6.7	6.7	1.03	3000	0.02	59.98	664.93
LA14	Northridge, 1994, Newhall	6.7	6.7	1.03	3000	0.02	59.98	644.49
LA15	Northridge, 1994, Rinaldi RS	6.7	7.5	0.79	2990	0.005	14.945	523.30
LA16	Northridge, 1994, Rinaldi RS	6.7	7.5	0.79	2990	0.005	14.945	568.58
LA17	Northridge, 1994, Sylmar	6.7	6.4	0.99	3000	0.02	59.98	558.43
LA18	Northridge, 1994, Sylmar	6.7	6.4	0.99	3000	0.02	59.98	801.44
LA19	North Palm Springs, 1986	6	6.7	2.97	3000	0.02	59.98	999.43
LA20	North Palm Springs, 1986	6	6.7	2.97	3000	0.02	59.98	967.61

Table A.2 Los Angeles ground motions (2% in 50 years)

SAC Name	Record	Earthquake Magnitude	Distance (km)	Scale Factor	Number of Points	DT (sec)	Duration (sec)	PGA (cm/sec^2)
LA21	1995 Kobe	6.9	3.4	1.15	3000	0.02	59.98	1258.00
LA22	1995 Kobe	6.9	3.4	1.15	3000	0.02	59.98	902.75
LA23	1989 Loma Prieta	7	3.5	0.82	2500	0.01	24.99	409.95
LA24	1989 Loma Prieta	7	3.5	0.82	2500	0.01	24.99	463.76
LA25	1994 Northridge	6.7	7.5	1.29	2990	0.005	14.945	851.62
LA26	1994 Northridge	6.7	7.5	1.29	2990	0.005	14.945	925.29
LA27	1994 Northridge	6.7	6.4	1.61	3000	0.02	59.98	908.70
LA28	1994 Northridge	6.7	6.4	1.61	3000	0.02	59.98	1304.10
LA29	1974 Tabas	7.4	1.2	1.08	2500	0.02	49.98	793.45
LA30	1974 Tabas	7.4	1.2	1.08	2500	0.02	49.98	972.58
LA31	Elysian Park (simulated)	7.1	17.5	1.43	3000	0.01	29.99	1271.20
LA32	Elysian Park (simulated)	7.1	17.5	1.43	3000	0.01	29.99	1163.50
LA33	Elysian Park (simulated)	7.1	10.7	0.97	3000	0.01	29.99	767.26
LA34	Elysian Park (simulated)	7.1	10.7	0.97	3000	0.01	29.99	667.59
LA35	Elysian Park (simulated)	7.1	11.2	1.1	3000	0.01	29.99	973.16
LA36	Elysian Park (simulated)	7.1	11.2	1.1	3000	0.01	29.99	1079.30
LA37	Palos Verdes (simulated)	7.1	1.5	0.9	3000	0.02	59.98	697.84
LA38	Palos Verdes (simulated)	7.1	1.5	0.9	3000	0.02	59.98	761.31
LA39	Palos Verdes (simulated)	7.1	1.5	0.88	3000	0.02	59.98	490.58
LA40	Palos Verdes (simulated)	7.1	1.5	0.88	3000	0.02	59.98	613.28

Table A.3 Los Angeles ground motions (50% in 50 years)

SAC Name	Record	Earthquake Magnitude	Distance (km)	Scale Factor	Number of Points	DT (sec)	Duration (sec)	PGA (cm/sec^2)
LA41	Coyote Lake, 1979	5.7	8.8	2.28	2686	0.01	39.38	578.34
LA42	Coyote Lake, 1979	5.7	8.8	2.28	2686	0.01	39.38	326.81
LA43	Imperial Valley, 1979	6.5	1.2	0.4	3909	0.01	39.08	140.67
LA44	Imperial Valley, 1979	6.5	1.2	0.4	3909	0.01	39.08	109.45
LA45	Kern, 1952	7.7	107	2.92	3931	0.02	78.6	141.49
LA46	Kern, 1952	7.7	107	2.92	3931	0.02	78.6	156.02
LA47	Landers, 1992	7.3	64	2.63	4000	0.02	79.98	331.22
LA48	Landers, 1992	7.3	64	2.63	4000	0.02	79.98	301.74
LA49	Morgan Hill, 1984	6.2	15	2.35	3000	0.02	59.98	312.41
LA50	Morgan Hill, 1984	6.2	15	2.35	3000	0.02	59.98	535.88
LA51	Parkfield, 1966, Cholame 5W	6.1	3.7	1.81	2197	0.02	43.92	765.65
LA52	Parkfield, 1966, Cholame 5W	6.1	3.7	1.81	2197	0.02	43.92	619.36
LA53	Parkfield, 1966, Cholame 8W	6.1	8	2.92	1308	0.02	26.14	680.01
LA54	Parkfield, 1966, Cholame 8W	6.1	8	2.92	1308	0.02	26.14	775.05
LA55	North Palm Springs, 1986	6	9.6	2.75	3000	0.02	59.98	507.58
LA56	North Palm Springs, 1986	6	9.6	2.75	3000	0.02	59.98	371.66
LA57	San Fernando, 1971	6.5	1	1.3	3974	0.02	79.46	248.14
LA58	San Fernando, 1971	6.5	1	1.3	3974	0.02	79.46	226.54
LA59	Whittier, 1987	6	17	3.62	2000	0.02	39.98	753.70
LA60	Whittier, 1987	6	17	3.62	2000	0.02	39.98	469.07

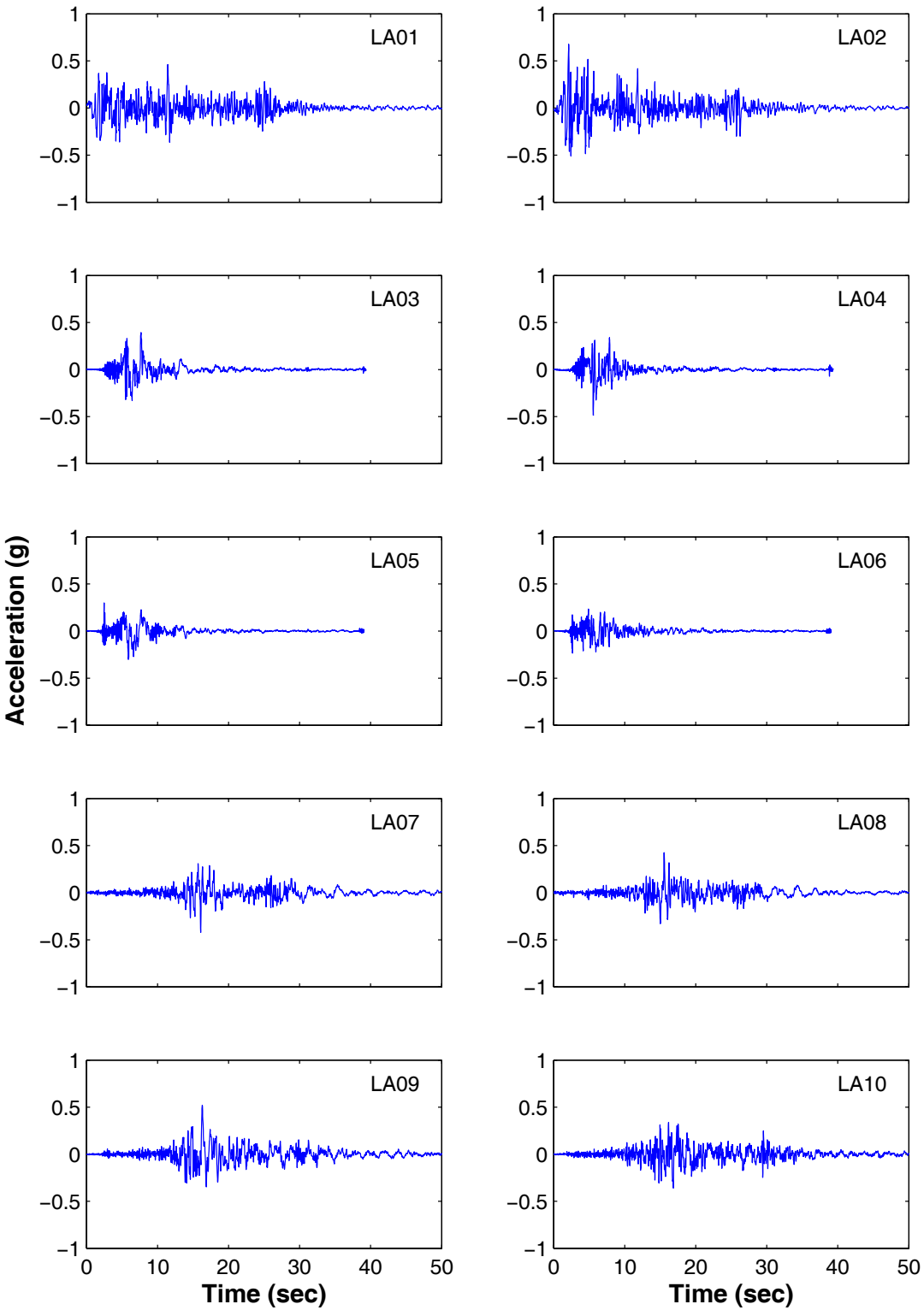

Figure A.1 Ground motion time histories (LA01 – LA10)

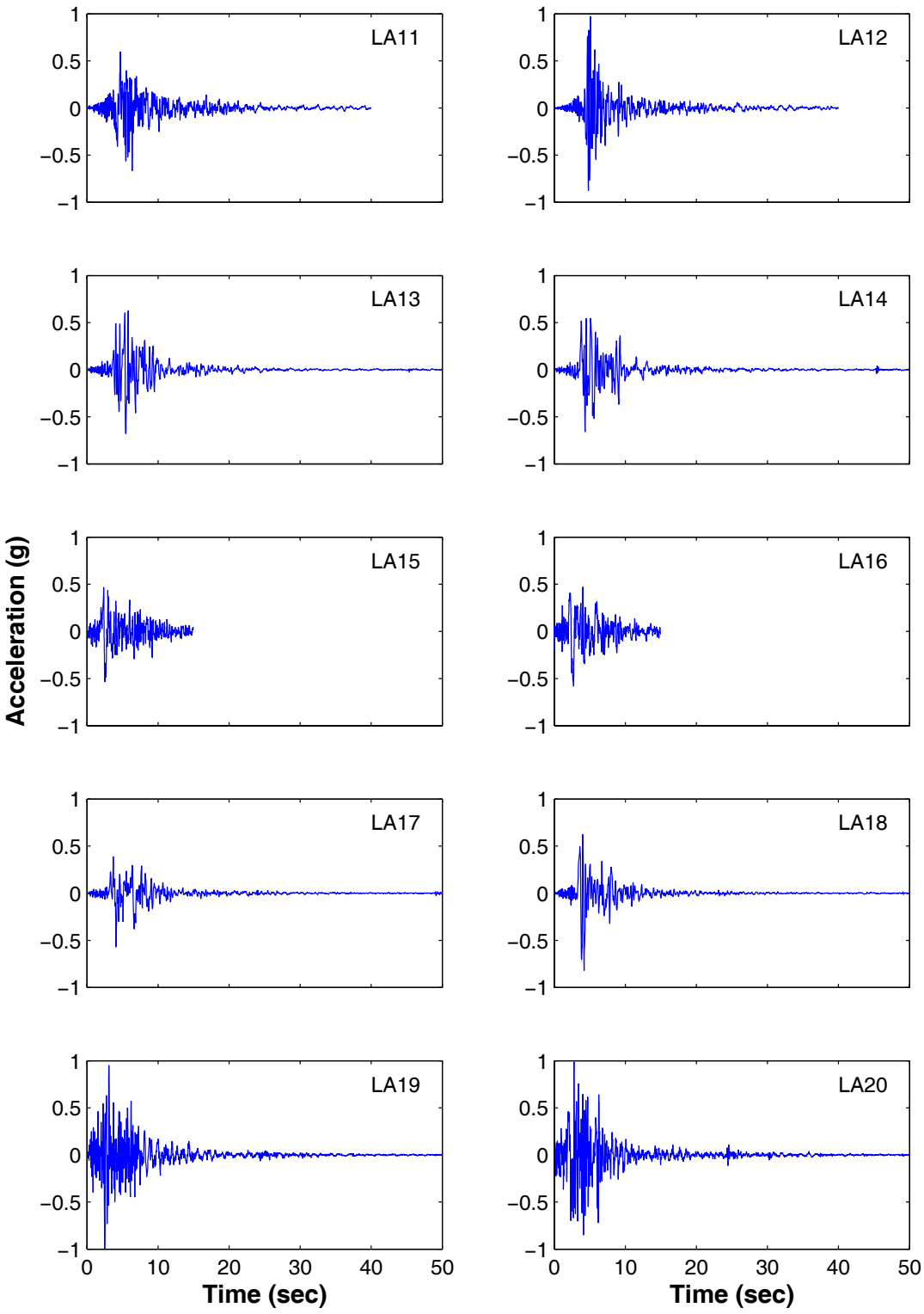

Figure A.2 Ground motion time histories (LA11 – LA20)

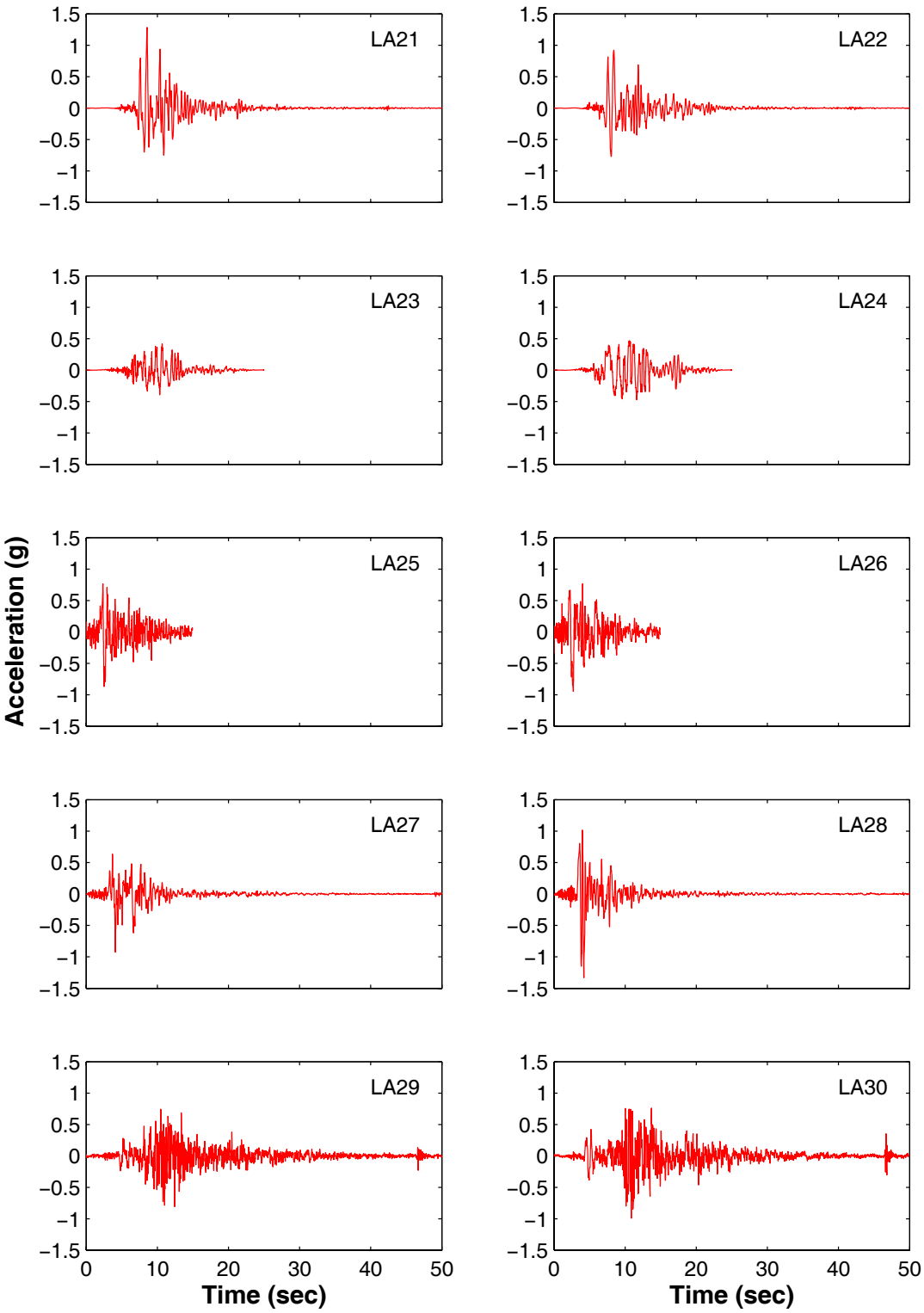

Figure A.3 Ground motion time histories (LA21 – LA40)

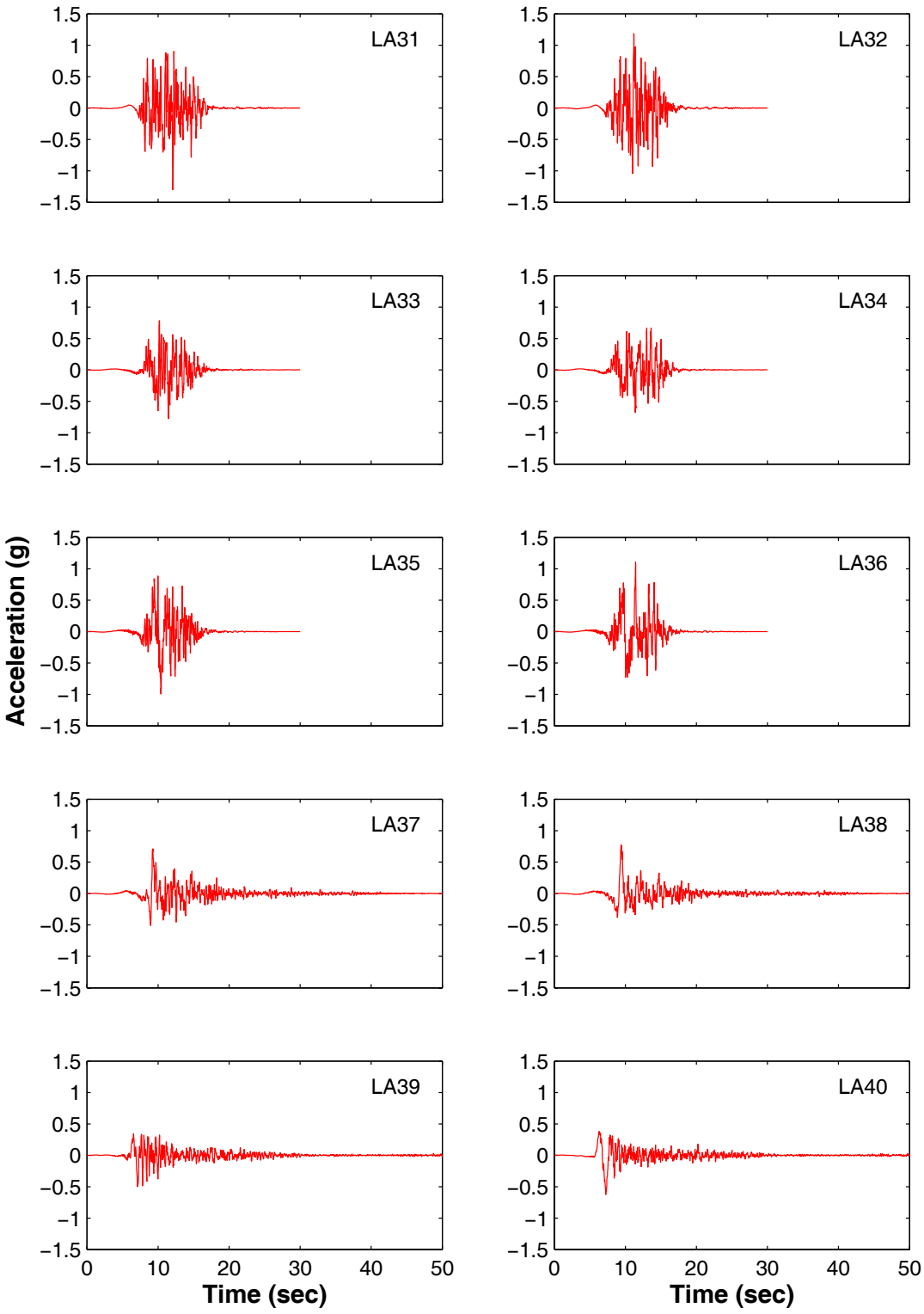

Figure A.4 Ground motion time histories (LA31 – LA40)

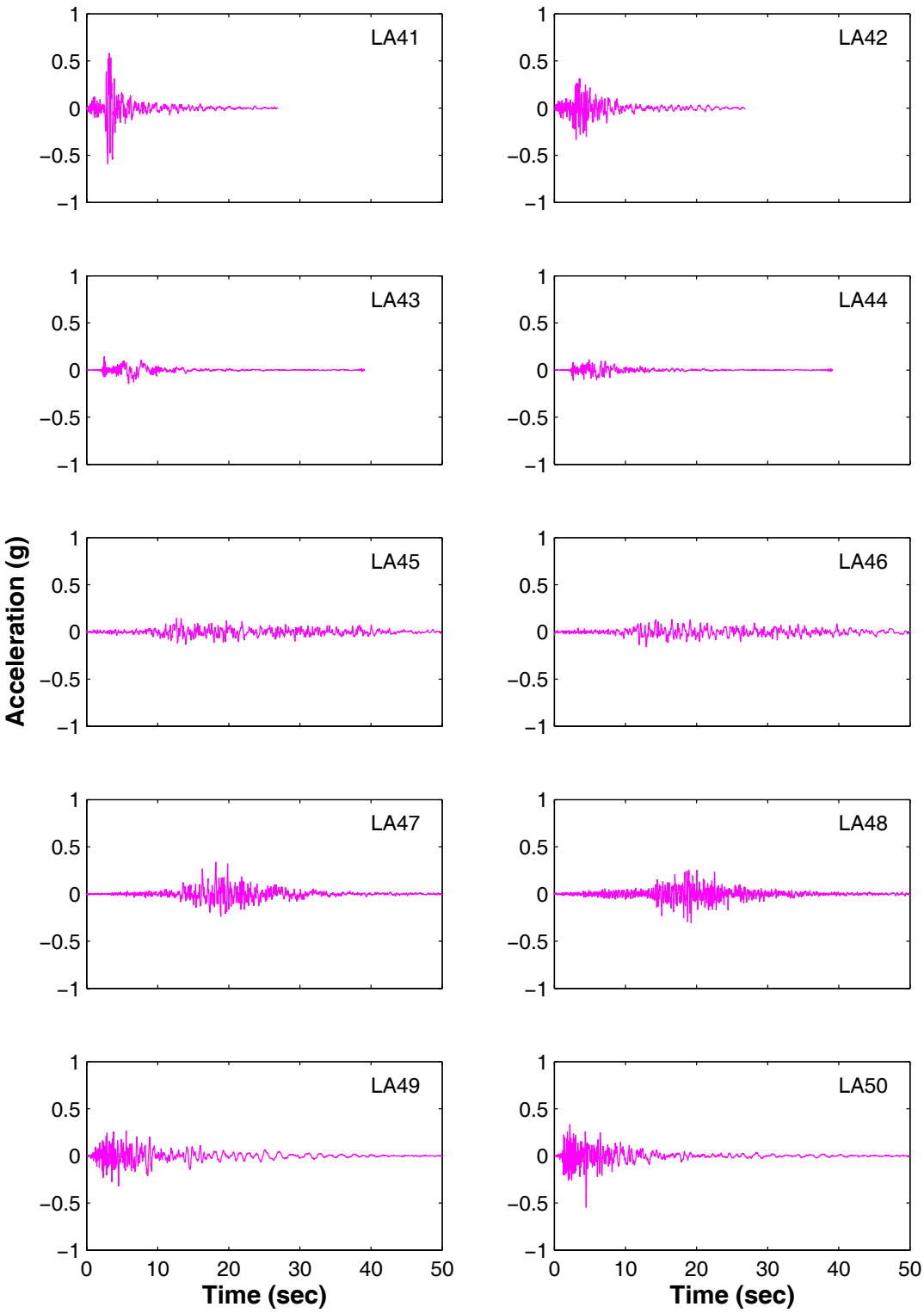

Figure A.5 Ground motion time histories (LA41 – LA50)

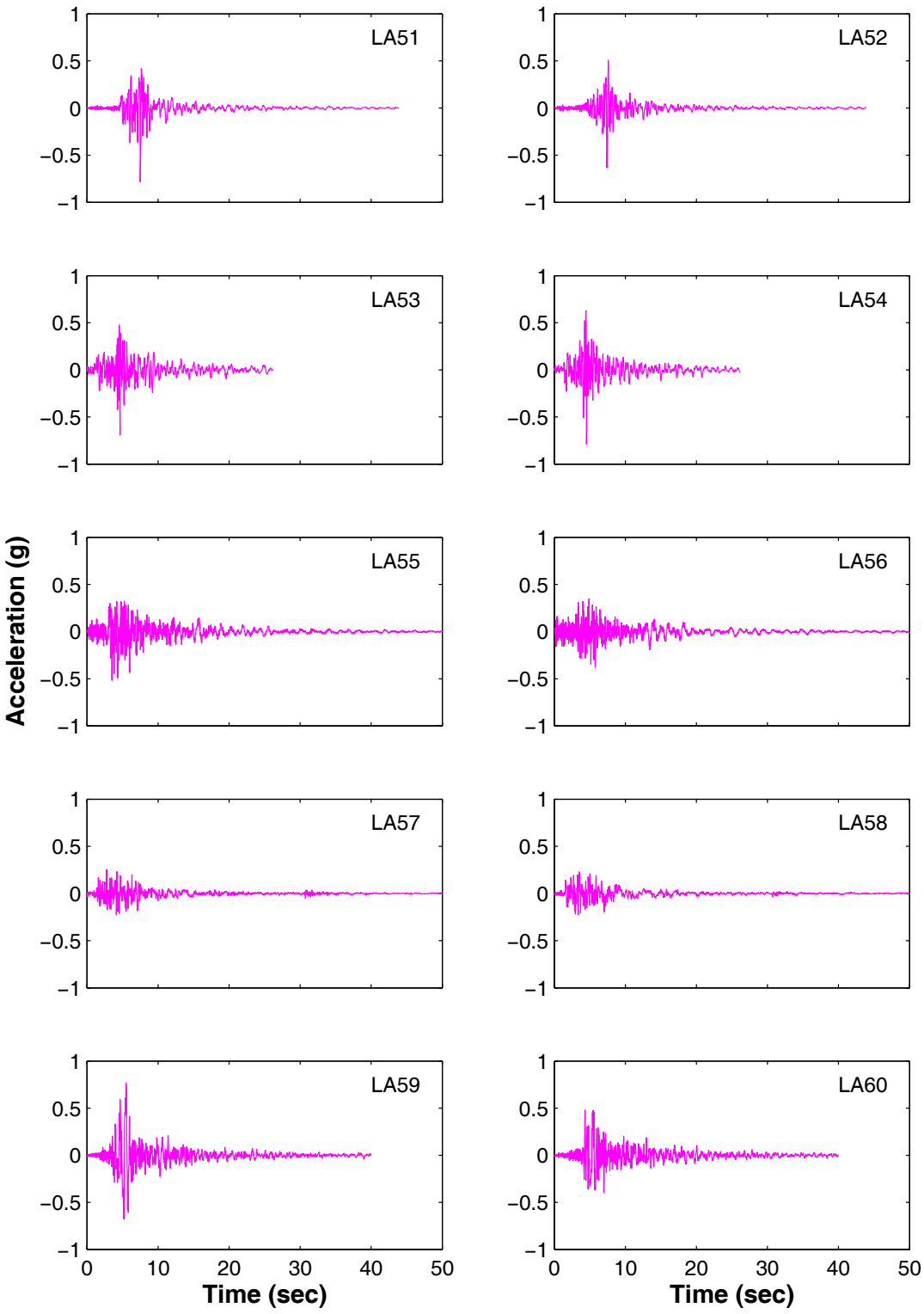

Figure A.6 Ground motion time histories (LA51 – LA60)

APPENDIX B PROTOTYPE BUILDING

The 3-story and 6-story concentrically braced frames (model 3vb2 and 6vb2) used by Sabelli (2001) and Kiggins and Uang (2006) in their study of buckling-restrained-braced (BRB) frames are selected as the prototype structures in this study. These two BRB frame buildings are designed to be located in downtown Los Angeles with site class D (firm soil). Figure B.1 and Figure B.2 show the building plans and elevations of the 3- and 6-story frame buildings respectively. The locations of braces, as well as the section sizes of columns and beams, are also shown in Figure B.1 and Figure B.2. The typical story height is 3.96 m (13 ft), except for the first story of the 6-story building which has a story height of 4.88 m (16 ft). The typical bay width is equal to 9.15 m (30 ft).

The design of these buildings followed the FEMA building design criteria, in which a response of modification factor (R) of 8 was employed. Table B.1 shows the tensile yield strength and axial stiffness of BRBs for each story. The compression capacities of all the BRBs were assumed to be 1.1 times their tension capacities based on previous research observation. The yield capacities of the BRBs were selected to just satisfy the minimum strength requirements such that the capacity of each structure was not over-designed. A992 Gr.50 steel was used for all beams and columns.

In numerical analyses, only one bay of the braced frame was modeled and analyzed. Thus the seismic mass of each floor was calculated by dividing the total seismic floor masses with the number of braced bays in each principal direction (i.e.,

1/4 of the total dead load for the 3-story building and 1/6 of the total dead load for the 6-story building). All beam-to-column connections except for those at the roof were modeled as rigid connection by considering the effect of attached gusset plates while the ends of all braces were assumed as frictionless pins. The column bases are assumed fixed to the ground. In order to approximately account for the stiffness contribution from all other columns in the un-braced frame, a column running the full height was added to the model. Global P-Δ effect was also considered in the nonlinear time history analyses. More details about the prototype buildings can be found in Sabelli (2001).

Table B.1 Properties of the BRBs in the prototype buildings

Building Model	Story #	BRB	
		Tensile Strength (kN)	Axial Stiffness (kN/m)
3-story	3	520	1.030×10^5
	2	872	1.651×10^5
	1	1081	1.905×10^5
6-story	6	391	0.798×10^5
	5	712	1.418×10^5
	4	961	1.881×10^5
	3	1160	2.238×10^5
	2	1299	2.481×10^5
	1	1699	2.500×10^5

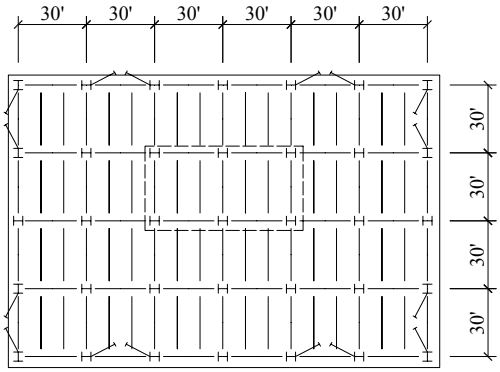

(a) Building plan

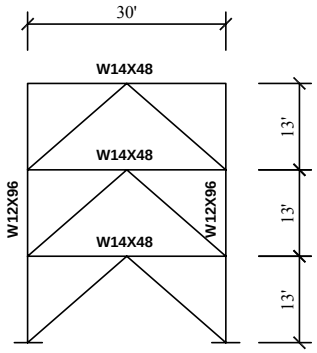

(b) Frame elevation

Figure B.1 The prototype steel frame structures: 3-story building

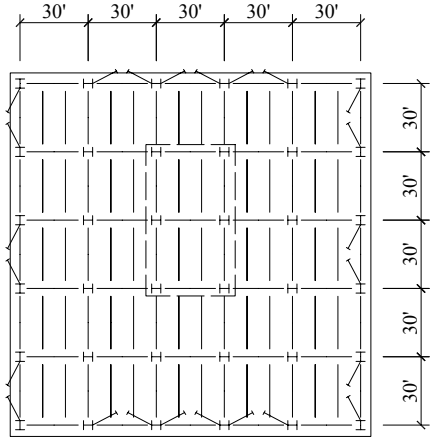

(a) Building plan

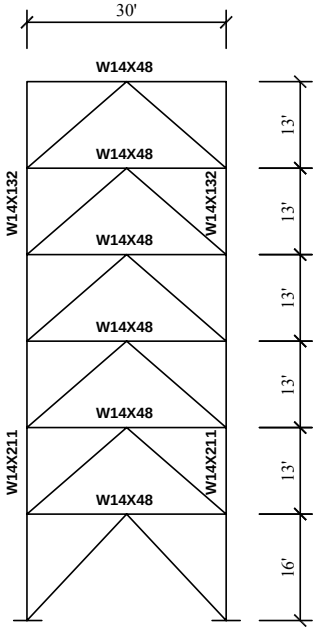

(b) Frame elevation

Figure B.2 The prototype steel frame structures: 6-story building